METROLOGY AND FABRICATION OF VOLUME-STRUCTURED OPTICAL AND MECHANICAL FEATURES IN PHOTOPOLYMERS

by

DAVID JOHN GLUGLA

B.S., University of Colorado Boulder, 2012

M.S., University of Colorado Boulder, 2015

A thesis submitted to the

Faculty of the Graduate School of the

University of Colorado in partial fulfillment

of the requirement for the degree of

Doctor of Philosophy

Department of Electrical, Computer, and Energy Engineering

2018

This thesis entitled:
Metrology and fabrication of volume-structured optical and mechanical features in photopolymers
written by David J. Glugla
has been approved for the Department of Electrical, Computer, and Energy Engineering

_____
Professor Devatha P. Nair

_____
Professor Robert R. McLeod

Date_____

The final copy of this thesis has been examined by the signatories, and we find that both the content and the form meet acceptable presentation standards of scholarly work in the above mentioned discipline.

Abstract

Glugla, David J. (Ph.D., Electrical, Computer, and Energy Engineering)

Metrology and fabrication of volume-structured optical and mechanical features in photopolymers

Thesis directed by Professor Robert R. McLeod

The ability to exert three-dimensional control over the intrinsic mechanical and optical properties of a solid are desirable in the fields of diffractive optical elements, shape programmable materials, and regenerative medicine. Although volume photostructuring in two-stage polymers has demonstrated the ability to produce such features, quantitative metrology of the photostructured elements remains a significant obstacle towards the widespread adoption of this patterning technique. Current methods to characterize photostructured features provide only qualitative information or fail to capture the entire material response. This inadequate characterization impedes the broader adoption of photostructuring to fabricate complex mechanical and optical devices.

In this thesis, I overcome the problem of quantitative metrology in photostructuring by developing techniques to measure the resulting mechanical and optical features. To do this, I first categorize the photostructuring process into two distinct groups: 1) local reactions that are confined to the exposed region, and 2) reactions that induce mass transport through e.g. diffusion. For local reactions, I demonstrate the suitability of bulk metrology on uniform samples to characterize and infer the properties of in-situ photostructured elements. For reactions that induce mass transport, bulk metrology is no longer adequate, and in-situ metrology is required. To measure photostructuring in these materials, I develop a new technique using quantitative phase imaging and confocal reflection microscopy that provides complete characterization of the

material response. The knowledge gained from these metrology techniques is then applied to fabricate novel mechanical and optical devices such as self-folding origami structures and high diffraction efficiency, large-aperture Fresnel lenses. Finally, by exploring a novel multiple-exposure method, I demonstrate how the presented metrology enables the development and understanding of new photostructuring techniques. This new patterning technique enhances the dynamic range of the photostructuring process beyond the single-exposure limit and extends the range of current photostructuring materials.

Dedication

For my family. You patiently supported me and always encouraged me to do my best.

Acknowledgements

Throughout my graduate studies, there have been a number of people to whom I owe a great deal of gratitude. First, I would like to thank my advisor, Professor Robert McLeod for his guidance and support. He helped me to not only love research (and Fourier transforms), but through his tutelage, I became a more effective writer and presenter. I am also grateful for the many connections and research opportunities that he has provided me.

Next, I would like to thank Professor Christopher Bowman and the entire Bowman/Stansbury group for allowing me to use their facilities and sharing their expertise. Their equipment, tutelage, and collaboration greatly enhanced my understanding of photopolymer chemistry and was critical in the success of my projects. I am particularly thankful for the guidance and friendship provided by Dr. Alan Aguirre-Soto, Dr. Abeer Alzahrani, Kim Childress, Dr. Matthew McBride, Dr. Parag Shah, Dr. Brady Worrell, and Xinpeng Zhang.

I am also extremely grateful to Prof. Devatha Nair for all of her help and assistance during my first years as a graduate student. Despite already managing a multitude of undergraduate students in addition to her own research, she found the time to take me under her wing and teach me most of what I know about materials characterization and polymer chemistry. She continued to be a valuable friend and mentor throughout my studies even after starting her own lab at the Anschutz campus.

I also want to thank Professor Carol Cogswell and her group for allowing me to use their brightfield microscope to perform quantitative phase imaging. I am especially thankful for the assistance provided by Dr. Jiun-Yann and Simeng Chen whenever I needed to use the piezo stage on the microscope.

Next, I would like to thank my undergraduate assistants: Keaton Byars and Madeline Chosy. I could not have asked for more motivated and talented students.

I would like to thank all of the past and current members of the McLeod group for their friendship, support, and assistance over the years. I especially want to thank Dr. Amy Sullivan and Dr. Darren Foreman for their friendship and guidance over the years. Thanks as well to Marvin Alim, Dr. Martha Bodine, Dr. Callie Fiedler, Dr. Jake Friedlein, Johnny Hergert, Keith Kamysiak, Dr. Ben Kowalski, Dr. Zefram Marks, David Miller, Archish Muralidharan, Josh Noble, Charlie Rackson, Megan Renny, Dr. Adam Urness, Camilla Uzcategui, and Dr. Chunfang Ye.

Lastly, I want to thank my funding sources:

- NSF EFRI (1240374)
- NSF STTR Phase I (1721055)
- NSF GOALI (1307918)
- Department of Education GAANN fellowship (P200A120063)
- NIH

Table of Contents

Tables

Figures

CHAPTER I
INTRODUCTION

A. Motivation

Three-dimensional photostructuring of solid polymers offers a means to integrate diverse mechanical, optical, and chemical functionality into a single material. This capability is desirable in a number of fields where gradient properties are necessary, including shape programmable materials (SPMs) [1–3], photonics [4–10], biology [11], and regenerative medicine [12,13]. For example, control over the 3D refractive index within a polymer volume has been used to implement holographic data storage [5,14], optical interconnects/couplers for on-chip waveguides [6,15], custom 2D phase elements [16], and diffractive optical elements (DOEs) for augmented reality and solar concentration [4,8,17]. 3D structuring of volume mechanical properties has also enabled self-actuated origami [1], cell scaffolds that mimic in-vivo environmental conditions [12], and non-planar, twisted microfluidic devices [3]. However, widespread adoption of volume photostructuring in solid polymers remains limited due to the lack of in-situ, quantitative metrology, which in turn limits the types of features that can be produced. In this work, I extend the understanding of volume photostructuring in solid polymers by first overcoming the metrology problem. To do this, I develop metrology techniques that both probe the material with the appropriate resolution, and enable characterization of in-situ features. This knowledge allows me to 1) extend and enhance current photostructuring techniques in photopolymers, and 2) apply these new structuring techniques to fabricate novel 3D analog mechanical and photonic devices such as self-actuated origami structures and flat, gradient-index Fresnel lenses (Figure I-1).

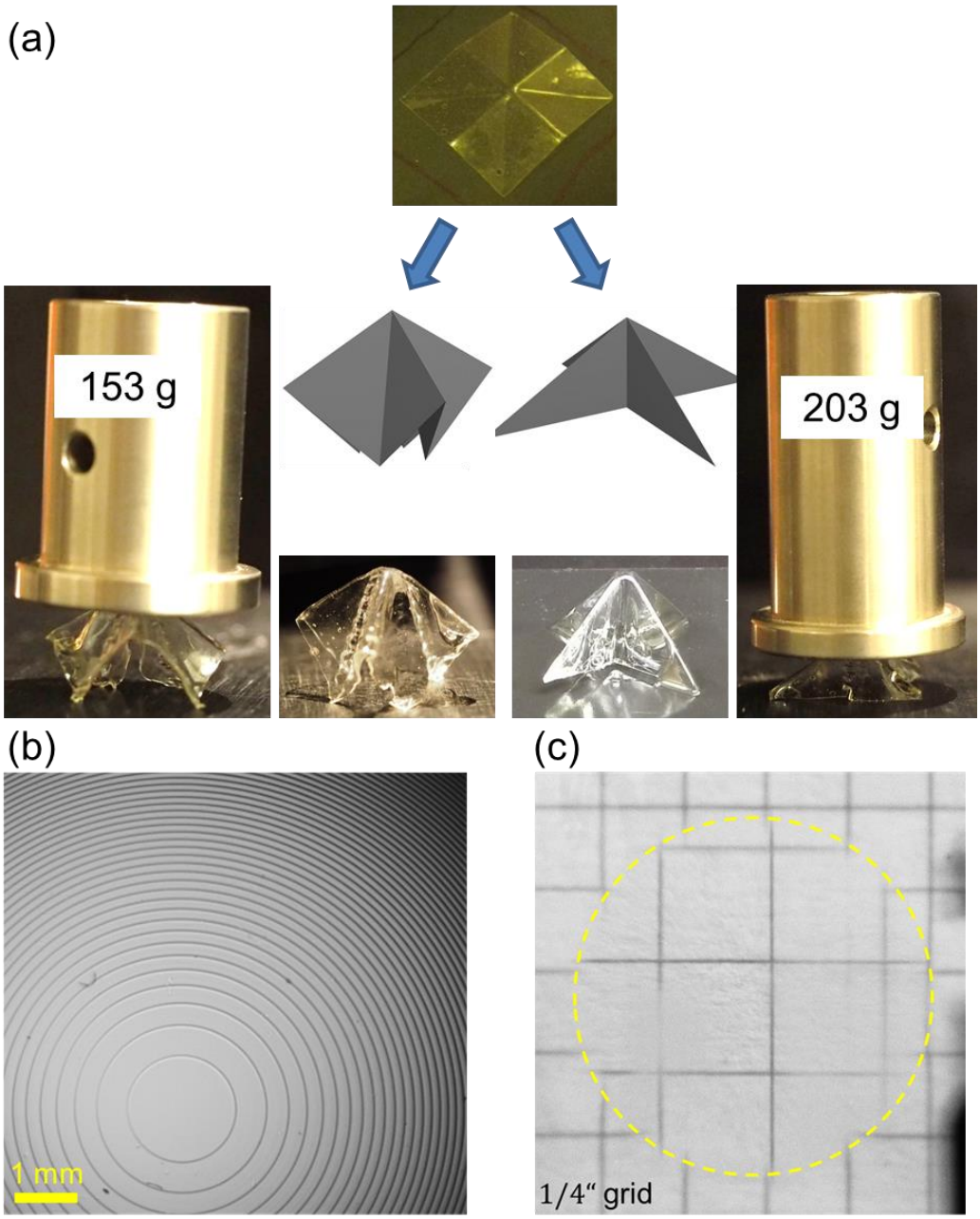

Figure I-1**.** (a) Self-actuated origami structure fabricated through mechanical photostructuring. Mechanical patterning programs the sheet to fold into a waterbomb base upon immersion in a solvent. A final exposure polymerizes the solvent and creates a permanent, rigid structure that can support up to 1500 times its own weight. (b) Fresnel lens fabricated through photostructuring the refractive index of a polymer. (c) The fabricated Fresnel lens used to magnify an object.

In order to understand the requirements for metrology of volume-structured polymers, the remainder of this chapter first introduces the physical mechanisms involved in volume

photostructuring. This information then defines the requirements necessary to perform quantitative metrology in these structured materials. In light of these requirements, I discuss strategies for performing quantitative metrology in photostructured polymers. Finally, I outline how this metrology will assist in extending current photostructuring methods, and in fabricating novel mechanical and photonic structures.

B. Volume photostructuring

Volume photostructuring occurs through the following sequence of events [18]: 1) incident photons are absorbed by the material, 2) the absorbed energy induces a photo-triggered event in the material, and 3) the photoinduced event changes the material's properties. Although light absorption can trigger a variety of phenomena, ranging from photochemical reactions to melting, the end-result is a change in the material properties. Therefore, I categorize the photostructuring process into two distinct groups. The first consists of purely local reactions that are confined to the exposed region. The second category includes events that induce mass transport, e.g. diffusion, and are thus nonlocal. Figure I-2(a-d) details the first category of local structuring. In this example, a photoreactive chemical species (red) is incorporated into the solid polymer network during formulation. Upon irradiation, the species reacts with other nearby reactive groups on the network and the effects of the reaction remain confined to the exposed area. In the case of the second category, the mobile, photoreactive species is able to diffuse through the solid network [Figure I-2(f-i) - red circles]. Concentration gradients initiated by photostructuring will drive transport of reactive and unreactive species. In this case, any region of the material including those not illuminated can be influenced by the diffusion of these species.

The distinction between immobile and mobile events in the above discussion highlights the need to determine a material's underlying photostructuring mechanism before choosing the appropriate metrology technique. For example, the response of materials with purely local reactions does not depend on the size or shape of the material or illumination. Therefore, the photoresponse of these materials can be characterized through metrology of bulk materials. Here, 'bulk' refers to homogeneous materials whose dimensions are at least an order of magnitude larger than the in-situ structure, yet still possess the same properties. The measured properties from this bulk material can then be used to directly infer the properties of the in-situ structure. However, in the presence of diffusion or other transport mechanisms, the profile and scale of illumination can dramatically modify the photo-response. In this case, properties must instead be measured in-situ.

In this thesis, I will use a class of photo-responsive materials referred to as two-stage photopolymers. As fully described next, these encompass a class of materials including a solid matrix, which may or may not be chemically functionalized or swollen with a reactive or unreactive liquid. These degrees of freedom in the chemical formulation enable a number of useful approaches to three-dimensional gradient photostructuring of mechanical and optical properties.

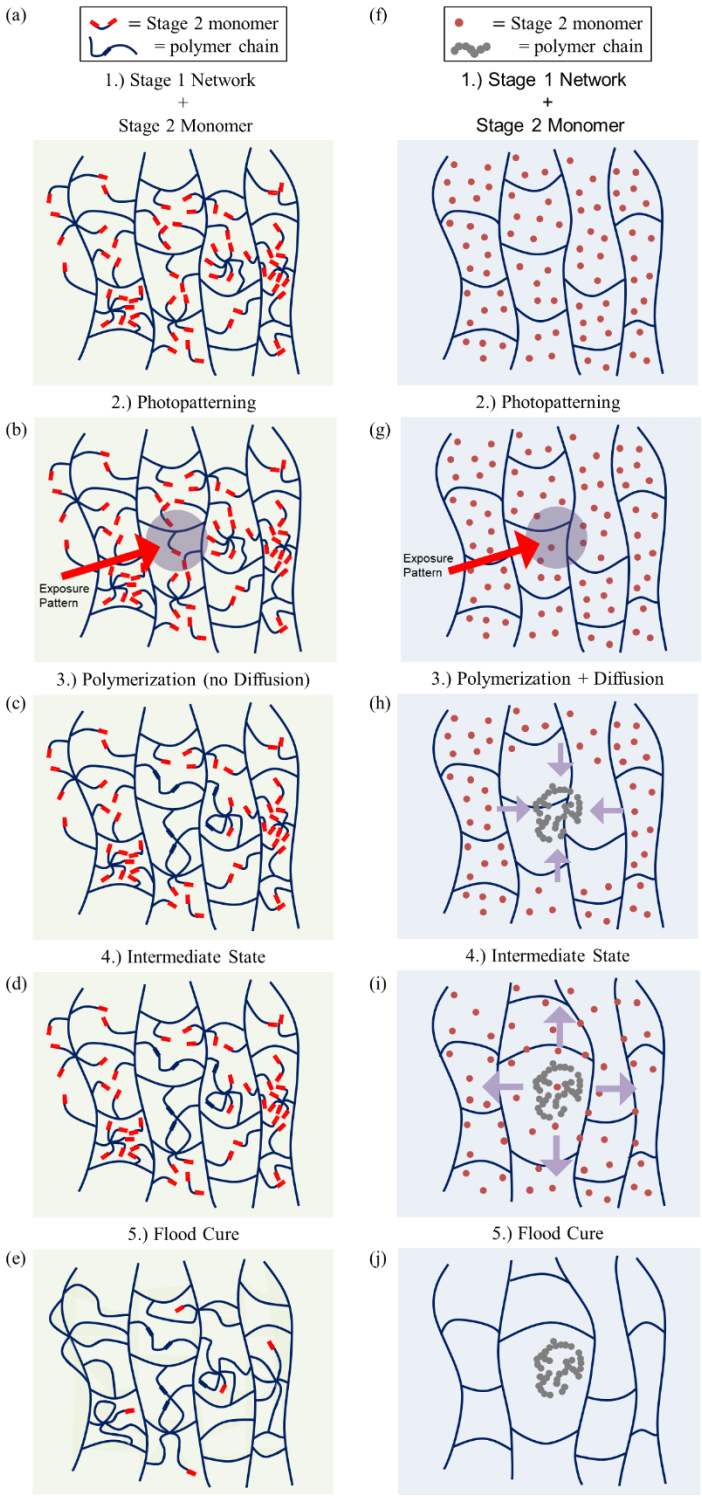

Figure I-2. The general process for photostructuring in a material where the photochemical reaction is confined (a-e) and in a material where photostructuring induces mass transport (f-j). (a-e) Two-stage material utilizing a tethered stage-2 monomer. (b-c) A patterned photoexposure

locally polymerizes the stage-2 chemistry and results in a spatially non-uniform material. (c-d) Because tethering of the stage-2 chemistry inhibits diffusion, their concentration distribution remains unchanged. (e) Because the concentration distribution of stage-2 monomer remains unaltered in this material, a final uniform flood cure will polymerize the remaining stage-2 monomers, resulting in a bulk, uniform material. (f) A two-stage material utilizing an untethered stage-2 monomer. (g) A patterned photoexposure polymerizes the local stage-2 monomer. (h) Diffusion re-equilibrates the unreacted monomers and the stage-1 matrix swells out of the region of exposure, resulting in (i) a spatially non-uniform concentration of the stage-2 material. (j) A final flood cure polymerizes the remaining unreacted monomer and freezes the non-uniform stage-2 concentration, resulting in a material with spatially-varying properties.

C. Two-stage photopolymers

The model photopolymer in this work is a two-stage system that incorporates two orthogonal reactive chemistries. The stage-1 chemistry polymerizes to form a loosely-crosslinked polymer network that hosts the remaining second-stage reactive species. This stage-2 chemistry is later initiated during photostructuring either to form its own interpenetrating network, or to attach to the stage-1 matrix. In order to explore both local and nonlocal photostructuring, I use different versions of the two-stage photopolymer. The first system utilizes a tethered photostructuring mechanism that alters the mechanical properties of the polymer network, while the second system is swollen with a mobile, reactive monomer whose diffusion alters the optical properties of the material.

The first of the two-stage photopolymer systems uses a stage-1 reaction where the second-stage species is directly tethered into the initial network [similar to Figure I-2(a)]. This restricts any long range mobility, yet enables the stage-2 reaction to directly modify the stage-1 network [Figure I-2(b-d)]. In this case, illumination causes the stage-2 species to homopolymerize and generate additional crosslinks within the exposed region. Because all of the stage-2 species are immobile, uniformly exposing the entire material will polymerize all remaining stage-2 species and wash out any features created by prior exposures [Figure I-2(e)]. I will show below that this is not the case for materials that allow transport between exposures.

Examples of the properties that can be structured in this type of photopolymer system are demonstrated in the work by Nair et al. [19,20]. In their work, they used a tethered multifunctional acrylate in the second-stage chemistry to increase the crosslink density, modulus and glass transition temperature (T_g) of the network. Because this second-stage was photoinitiated, they were able to control both the location and extent of the reaction, which allowed them to pattern analog mechanical properties into the material. In this work, I will advance the capability of this material by developing photo-controlled folding of mechanically robust origami.

The second two-stage photopolymer system uses an untethered stage-2 monomer that is able to diffuse within the network [Figure I-2(f)]. During photostructuring, these stage-2 monomers form entangled chains or interpenetrating networks within the host [Figure I-2(g)]. Following the initial reaction, the unreacted stage-2 monomer re-equilibrates through diffusion [Figure I-2(h-i)]. This re-equilibration results in an overall increased concentration of the stage-2 species in the exposed region and a decrease in concentration elsewhere. Thus, photostructuring in this material not only creates concentration gradients of the stage-2 species, but it also influences future exposures. In contrast to the previous tethered system, a uniform flood exposure applied after photostructuring and re-equilibration [Figure I-2(i)] will result in a permanent concentration gradient rather than a uniform material [Figure I-2(j)]. The ability of this photopolymer system to create permanent concentration gradients has motivated use in holography and diffractive optics. Because the stage-1 and stage-2 components possess different refractive indices, increasing the local concentration of one relative to the other will produce a subsequent Δn according to the Lorentz-Lorenz mixing rule [21]. Thus, control over concentration gradients provides the ability to make complex phase structures and DOEs. A

number of commercial photopolymers such as Covestro's Bayfol HX, and Akonia's DRED material utilize this system for such applications [14,17,22].

D. Requirements for the metrology of photostructured features

In light of the photostructuring mechanisms and materials discussed above, quantitative metrology of photostructured features requires: 1) noninvasive, direct measurement of the property of interest, and 2) the ability to resolve the entire feature. Here non-invasive means quantifying the desired property without affecting the state of the system. By "direct", I mean that the ideal technique would measure the desired property within the 3D host without the addition of a label, e.g. a fluorophore. Such labels may influence the chemistry of the system or, more commonly, introduce additional uncertainty related to the fidelity and calibration of the labeling process itself.

The second condition is a common flaw in many 3D characterization methods, as I will show in later chapters. Specifically, the metrology system must be capable of resolving 3D spatial plus temporal variations of the material with sufficient sampling density and resolution. If a portion of the material response falls outside the instrument's measurement capability, the measurements are not quantitative and thus cannot be predictive for materials development or design of applications.

It is important to note that the above requirements are not solely dependent on the final photostructured feature, but that they are also influenced by the photostructuring mechanism. As previously discussed, photopolymers that use a tethered stage-2 species are amenable to bulk characterization techniques because the material obeys both spatial and temporal invariance to photostructuring, i.e. diffusion does not re-equilibrate reacted species and the material remains

static after the photostructuring process. Furthermore, because modern photopatterning techniques can precisely control the light exposure profile down to the micrometer and nanometer scales, the 3D volume of exposure can be accurately known. Therefore, characterization curves measuring bulk properties of uniformly reacted materials vs. exposure time and optical intensity can be used to directly infer the in-situ properties of the photostructed features. This strategy is amenable for the measurement of mechanical properties because established metrology techniques to measure Young's modulus, T_g, and crosslink density lack micrometer-scale resolution and are instead designed to measure bulk properties [23,24]. Despite efforts to improve the resolution of these techniques through, e.g. nanoindentation and atomic force microscopy, these techniques are still limited to surface features and are susceptible to errors resulting from defects in the probe [25]. In the following chapter, I will demonstrate the power of combining bulk metrology with the optical exposure profile to predict the in-situ properties of photostructured features. Using this predictive capability then allows me to extend the field of smart materials by fabricating novel, single layer shape programmable structures that use gradient, photostructured mechanical features to fold into complex shapes.

In contrast, materials whose response depends on mass transport must be characterized under illumination conditions representative of the intended use. Because diffusion of unreacted species occurs between each exposure, measurement of the material properties must be performed in-situ. In the case of photostructured optical elements, 2D imaging techniques such as digital holographic microscopy or quantitative phase imaging through the Transport of Intensity technique offer the ability to acquire rapid, micron-scale resolution images of phase features. However, as I will later demonstrate, no imaging techniques that use standard transmission imaging systems can completely measure arbitrary 3D structures due to the finite

coherent transfer function of the instrument. Optical tomography attempts to circumvent this issue by rotating the sample in order to improve the overlap of the object spatial frequency content with the coherent transfer function of the imaging system. However, implementation of such systems is non-trivial and requires specific sample geometry in order to both fit inside of the system and to avoid issues with total internal reflections off sample interfaces. I will overcome this problem of insufficient sampling and enable the quantitative characterization of arbitrary photostructures by using phase imaging techniques in a manner that guarantees overlap between the imaging system coherent transfer function and the entirety of the object spatial frequency content. Leveraging the high resolution and 2D imaging provided by phase imaging, I then investigate the in-situ development of photostructured features within a diffusive environment. This information then enables me to predict optical properties of photostructured features resulting from arbitrary 3D exposures. This quantitative characterization will also allow me to extend the current library of photostructuring techniques by demonstrating a multiple exposure process that improves the dynamic range of the photostructuring process.

E. Outline of the thesis

Chapter II demonstrates the use of bulk metrology, combined with chemical and mechanical modeling to predict the resulting 3D gradient in crosslink density, modulus, and swelling ratio within a mechanical two-stage photopolymer. This information is applied to design and fabricate a new self-actuated origami structure that uses its mechanically distinct polymerization states, and the ability to blend their associated properties, to mimic the supple folds and rigid panels found in traditional origami crease patterns. Additionally, the 3D swelling ratio of the folds is manipulated to enable directed, self-folding through differential absorption of an external solvent. Chapter III demonstrates the use of a quantitative phase imaging technique

to perform a comprehensive measurement of 2D in-situ, micron-scale refractive index profiles written into a two-stage holographic photopolymer. Because this metrology captures the entire material response, characterization of 2D structures is shown to enable the prediction of embedded 3D features without the need to perform tomographic measurements. Assisted by this characterization technique, chapter IV reveals a new multiple-exposure method to create phase structures that exceed the classical dynamic range in holographic photopolymers, and demonstrates a new method to perform in-situ diffusivity measurements. Then, in chapter V the characterization from chapters III and IV is used to fabricate a high-efficiency, large aperture Fresnel lens diffractive optical element within the two-stage photopolymer. Finally, chapter VI discusses future opportunities for applying the aforementioned metrology techniques to study the fundamental limitations of photostructuring in two-stage photopolymers.

CHAPTER II
SELF-FOLDING ORIGAMI THROUGH MECHANICAL PHOTOSTRUCTURING OF A TWO-STAGE PHOTOPOLYMER[1]

A. Chapter Overview

This chapter develops a characterization and photopatterning scheme to understand and control the 3D mechanical properties of a two-stage photopolymer [1]. In this material, the stage-2 chemistry is tethered into the backbone of the stage-1 network. Photostructuring induces crosslinking among the stage-2 species and increases the crosslink density of the network. Critically, this tethering scheme inhibits diffusion of unreacted stage-2 chemistry, which enables bulk metrology, i.e. characterization performed on homogeneous samples, to characterize the in-situ mechanical changes resulting from the stage-2 reaction. Informed by this characterization, I apply mechanical models to predict the material response to arbitrary, patterned optical exposures. With the ability to predict and control the 3D mechanical properties such as crosslink density, the local glass transition temperature, and swelling ratio, I then fabricate novel shape programmable structures for self-actuated origami.

B. Introduction

1. Shape-programmable materials and self-actuated origami

Shape-programmed materials (SPMs) have recently gained popularity as a means for assembling complex 3D structures from 2D sheets [26–29]. The ability to autonomously morph from a 2D sheet into a 3D structure has been used in a myriad of fields including photovoltaics and energy storage [30,31], microfluidic devices [3], cell encapsulants and scaffolds [32–37], surgery [38], sensing [39], porous structures and membranes [40,41], mechanical

[1] Adapted with permission from ACS Appl. Mater. Interfaces 8, 29658-29667 (2016). Copyright (2016) American Chemical Society. (Bibliography reference: [1])

metamaterials [42], robotics [43], and nanooptics [44,45]. At its core, shape-programming involves an initial processing step in which select regions of a sheet are modified to controllably deform upon exposure to an external stimulus at a later time [26]. Polymers are a promising materials system for shape programming due to their wide range of chemical and mechanical properties, large actuation strains in comparison to other active materials [46], and sensitivity to a variety of external stimuli [26,47]. A common approach towards the patterning of polymer SPMs is to create a sheet out of multiple discrete polymer segments, allowing for regions with dramatically different properties and responses to stimuli. Examples include bilayer [37,48], trilayer [49–51], and hinged structures [52,53] whose constituent elements exhibit different mechanical responses to heat, solvent, and pH stimuli. Recent work has also demonstrated the ability to spatially modify and program the mechanical and chemical properties of a single-layer, homogeneous polymer film. For example, light absorption within a layer of uncrosslinked SU-8 was exploited to induce a differential crosslink density throughout the thickness of the film. Upon removal of the remaining unreacted material, the differential crosslink density caused the film to undergo stress-induced bending [54]. Other optically patterned properties in single-layer films include differential porosity [2], alignment of liquid crystal networks [55,56], shape memory internal stresses [57], and network relaxation [50,58]. Because these SPMs are fabricated as homogeneous films whose properties are modified by a subsequent optical exposure, they can avoid the complex fabrication steps associated with multilayer material deposition, thereby presenting an attractive means for fabricating complex self-folding 3D structures via simple processing steps.

A popular method for coordinating the stimulus-induced deformations in SPMs utilizes basic origami principles such as creasing and folding, and has been successfully applied to

construct 3D devices such as self-folding robots [59]. Creasing occurs during the programming stage of SPMs, and results in a pattern of folding hinges and rigid panels. The hinges are characterized by a localized change in the material's mechanical and/or chemical properties such that, upon application of an external stimulus, they selectively undergo directed folding to form the desired 3D structure. Crease panels are those regions that do not respond to the applied stimulus and instead serve to constrain and channel the motion provided by the folding hinges. Recent examples of programmed crease patterns in single-layer SPMs include patterned relaxation of a polymer network via addition-fragmentation chain-transfer (AFT) [58], differential crosslinking to control swelling [3], mechanical fixing of shape memory polymers [60,61], and patterned deposition of an infrared-absorptive dye onto a shape memory polymer [62]. Although the above methods all successfully demonstrate the ability to make folded structures from initially homogenous sheets, many of these techniques require precise control over the applied stimulus in order to produce controlled bending. For example, thermal triggering of shape memory polymer crease patterns requires that the glass transition temperature be exceeded only within the creased hinges, otherwise the entire structure deforms. Techniques using AFT processes have not yet demonstrated the ability to incorporate rigid panels alongside flexible hinges, thereby limiting the types of achievable origami structures. For example, the Miura-ori pattern and tessellated waterbomb base, which exhibit negative Poisson's ratio and reduced degrees of freedom, are two of the most common origami structures used in engineering applications [63]. However, without the constraints imposed on the folds by rigid panels, the structures lose these unique mechanical properties. Finally, the inability of some of the aforementioned programming techniques to harden the flexible hinges after folding limits the

ultimate rigidity and stability of the final product, thereby restricting its use as a load-bearing structure.

2. Objective

Using a two-stage photopolymer system, I combine bulk characterization and mechanical modeling to understand and tune the 3D mechanical properties in order to create a single-layer, 2D SPM capable of folding into permanent, 3D, load-bearing, origami structures. This characterization provides the necessary information to accurately program latent crease pattern hinges and panels into the initial loosely crosslinked and rubbery stage-1 material via a series of optical exposures controlled by photomasks. The first exposure step creates the rigid, stage-2 panels by applying a large optical exposure dose to both sides of the material, while the unexposed hinges remain flexible and rubbery. A second photomask exposure applied to the bottom and top side of the photoabsorptive sheet programs mountain and valley folds respectively by creating a depth-wise gradient in the crosslink density of the hinges. Upon immersion of the sheet into a polymerizable solvent, these patterned hinges undergo nonuniform swelling, causing the mountain and valley folds to actuate, and the sheet to transform into the programmed 3D structure. After swelling, a final, uniform exposure polymerizes both the monomeric solvent and unreacted stage-1 material, and permanently fixes the shape. This last exposure increases the final modulus and glass transition temperature of the hinges by more than an order of magnitude compared to the stage-1 material, thereby forming a rigid, permanent structure capable of supporting external loads 1500 times its own weight.

C. Experimental Conditions and Techniques

The following section discusses the chemical formulation of the two-stage photopolymer and describes the experimental procedures to characterize its bulk mechanical and chemical properties. Also included are descriptions of the bulk folding tests for later use in fabricating self-folding directional hinges.

1. Two-stage polymer chemical formulation

The two-stage polymer was adopted from the procedure developed by Nair et al [19,20]. The thiol monomer, trimethylolpropane tri(3-mercaptopropionate) (Thiocure® TMPMP) was donated by Bruno Bock. The acrylate monomers were hexafunctional aliphatic urethane acrylate oligomers (Ebecryl® 1290) and difunctional tricyclodecane dimethanol diacrylate (TCDDA), donated by Allnex and Sartomer respectively. The UV photoinitiator DMPA (2,2-dimethoxy-2-phenylacetophenone) was donated by Ciba Specialty Chemicals, and the UV absorber, Tinuvin 328 was purchased from CIBA. The base used to catalyze the thiol-Michael reaction, triethyl amine (TEA), was purchased from Sigma-Aldrich. In order to provide a large difference in mechanical properties between stages 1 and 2, samples were fabricated with a 2:1 ratio of acrylate to thiol functional groups, and a 1:1 ratio of hexacrylate to diacrylate functional groups. In all samples, 2.5 wt% of TEA and 1 wt% of DMPA were added to initiate the stage-1 and stage-2 reactions, respectively. To create the stage-1 network, the photoinitiator and thiol were mixed first, and then added to the acrylates. Mixing during each step was performed in a heated $(65°C)$ water bath. After mixing finished, TEA was then added as the catalyst for the stage-1 thiol-Michael polymerization. Sheet thickness was controlled by casting the material between two silanated (RainX) glass plates with 127 or 254 μm spacers. Additionally, a small amount of the material was cast between salt plates and monitored via Fourier-Transform Infrared

Spectroscopy (FTIR) to ensure full thiol group conversion. Upon completion of the thiol-Michael reaction, the polymer sheet was delaminated from the plates and cut into various geometries for testing. For the creation of the self-actuating folds and bends, 0.5 wt% of Tinuvin 328 was added to attenuate light intensity through the $127\ \mu m$-thick sample. N-vinyl-2-pyrrolidone (NVP) (Acros Organics) mixed with 2 wt% of the photoinitiator 2, 4, 6-trimethylbenzoyldiphenylphosphine oxide (TPO) was used as the photopolymerizable solvent to swell and fold the creased materials.

2. Optical exposure conditions

After completion of the thiol-Michael stage-1 reaction, samples were delaminated from the glass plates and exposed directly to 365 nm light at 5 mW/cm^2 using an EXFOS Acticure 4000, 100 W high pressure mercury lamp equipped with a 365 nm bandpass filter. The relative stage-2 conversion was controlled by adjusting the exposure time, with longer exposure times resulting in higher stage-2 acrylate conversions. All irradiated samples were stored in the dark for at least 3 hours to allow any ongoing dark polymerization to terminate.

For the later demonstrations of fixing the shape of the folded structures via polymerization of the in-swollen NVP + TPO solution, $11\ mW/cm^2$ of 365 nm light was used to uniformly expose the material from each side. Exposure times of 90s for each side were used in all cases.

3. Fourier transform infrared spectroscopy

FTIR spectroscopy was used to monitor the homopolymerization of the remaining unreacted acrylates during stage-2 curing. A Thermo Scientific Nicolet 6700 FTIR spectrometer was fitted with a specialty mount for simultaneous UV irradiation, which allowed for monitoring

of the acrylate peak at 814 cm^{-1}, and concurrent irradiation of the sample with 365 nm light at 5 mW/cm^2. Optically transparent samples were prepared between two salt (NaCl) plates and allowed to cure at ambient temperature via the thiol-Michael reaction for 24 hours. Completion of the thiol-Michael stage-1 reaction was determined by ensuring that no remaining thiol peak around 2550 cm^{-1} was present. Final conversion of the remaining unreacted acrylates $(c_{acrylate})$ was monitored by integrating the peak over the range 790-830 cm^{-1} for various exposure times and intensities. The area of the acrylate peak after completion of the stage-1 reaction was given by $A_{initial}$. A_{final} was the area under the acrylate peak after completion of the stage-2 photoinitiated acrylate homopolymerization [see equation (2.1)].

$$c_{acrylate} = 1 - \frac{A_{final}}{A_{initial}} \tag{2.1}$$

4. Swelling strain vs. dose

Bulk swelling measurements were performed by immersing 127 μm-thick, 6.35 mm-radius discs of the optically thin two-stage polymer into NVP. Uniform crosslink density was achieved by preparing the polymer discs without photoabsorber. Once the samples reached equilibrium swelling strain after 24 hours, they were removed from the solvent and patted dry to remove any excess surface liquid. Pictures of the new, swollen discs were taken, and their corresponding radii were computed using ImageJ software and the ThreePointCircularROI plugin developed by Gabriel Landini [64].

5. Tensile testing

The tensile modulus of the polymer strips vs. optical exposure dose was measured using a TA Instruments Q800 DMA. Strips without photoabsorber were cut into rectangles measuring

$6.35 \times 12.7 \times 0.127\ mm$, exposed with $5\ mW/cm^2$, 365 nm light, and then strained at a rate of 800 μm/min at room temperature (23 ℃) in order to obtain the elastic stress-strain curve. When measuring the swollen modulus, strips prepared without photoabsorber were first irradiated with $5\ mW/cm^2$, 365 nm light, and then set aside for at least 3 hours to allow dark polymerization to terminate. The samples were then immersed in the NVP solvent for 24 hours. Immediately prior to measuring the stress-strain curve, samples were removed from the solvent and patted dry.

6. Crosslink density and glass transition temperature

To measure the crosslink density and glass transition temperature (T_g) of the material as a function of optical exposure dose, unswollen, stage-1 samples prepared without photoabsorber, with dimensions of $10 \times 6 \times 0.25$ mm were first exposed with 365 nm light at $5\ mW/cm^2$, and then stored in the dark for at least 3 hours. Measurements were obtained using a TA Instruments Q800 DMA. The sample temperature was ramped at 3℃/min from -20℃ to 180℃ with a frequency of 1 Hz and strain of 0.0125% in tension. The T_g was assigned as the maximum of the tan δ curve after a single temperature scan, and the crosslink density ($\rho_{crosslink}$) for each sample was calculated using equation (2.2) [65]:

$$\rho_{crosslink} = \frac{E'}{3RT} \tag{2.2}$$

where R is the gas constant and E' is the storage modulus at temperatures $T = T_g + 50$℃.

A similar method was used to determine the final T_g of strips that were swollen with the NVP/TPO solution and then uniformly exposed with 365 nm light. In this case, the stage-1 material was swollen in the NVP/TPO solution for 24 hours and then exposed on both sides with

11 mW/cm^2 light at a dose of 990 mJ/cm^2. The T_g was measured using the same Q800 DMA and testing parameters as before.

7. Bend radius of curvature

Two-stage polymer containing 0.5 wt% Tinuvin 328 was cut into strips measuring 6.35 × 1.6 × 0.127 mm. Each strip was exposed for different amounts of time using 365 nm light at 5 mW/cm^2. After exposure, strips were stored in the dark for 3 hours to allow for completion of dark polymerization prior to immersion in the NVP solvent. Measurements of the bend radius of curvature were taken after 24 hours of swelling. Images of the strips were captured and the bend radius was analyzed using ImageJ software and the ThreePointCircularROI plugin [64].

D. Characterizing and Tuning the Mechanical Properties

1. Design of the two-stage photopolymer

The two-stage polymer uses orthogonal polymerization reactions to produce a material with two sets of distinct mechanical properties (Figure II-1).

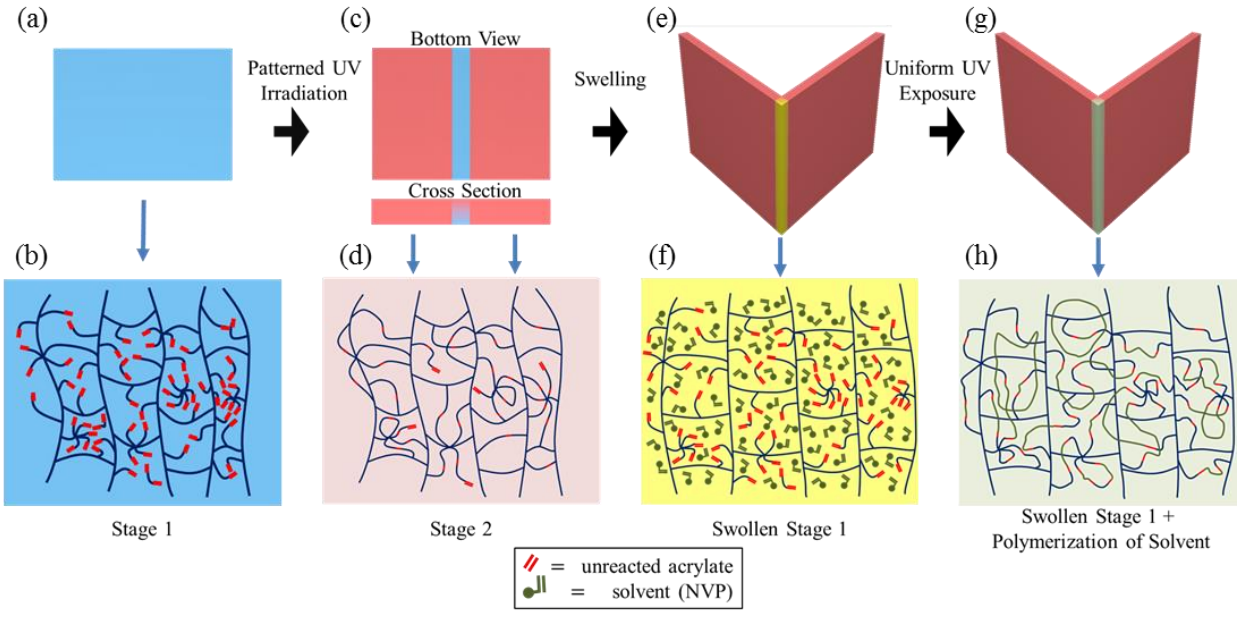

Figure II-1. The overall scheme depicting the different material states accessible to the two-stage photopolymer, and their application for creating self-folding SPMs. (a,b) The initial stage-1 material (blue) is composed of a rubbery and loosely crosslinked thiol-acrylate matrix with excess unreacted acrylate groups. (c,d) After exposure to UV light, the excess unreacted acrylates in the stage-1 material react to form a rigid, high-crosslink stage-2 matrix (red). Addition of a photoabsorber in the material allows for a gradient between stage 1 and 2 to be formed within the thickness of the material. (e,f) Upon immersion in N-vinyl-2-pyrrolidone (NVP), the stage-1 material swells (yellow). This swelling can be combined with the gradient-patterned material to create a self-folding hinge. (g,h) After folding, the swollen material is exposed to UV light, causing the NVP and unreacted acrylates to polymerize, resulting in a rigid, permanently swollen matrix (green).

The stage-1 network is designed to have a low modulus and crosslink density, while the photoinitiated stage-2 reaction is designed to produce a network with a modulus and crosslink density at least an order of magnitude higher than the stage-1 network. Polymerization of the stage-1 network uses a thiol-Michael base-catalyzed polymerization reaction, while stage 2 is induced via a photoinitiated chain-growth acrylate homopolymerization. The use of photoinitiator to trigger the stage-2 reaction allows for control over both the location and extent of stage-2 properties within the material. In order to produce a wide dynamic range for the mechanical properties between stage 1 and 2, the initial stage-1 network is fabricated using a 2:1 ratio of acrylate to thiol functional groups, which provides the large excess concentration of acrylates needed in the stage-2 reaction (Figure II-1b). The acrylate mixture is a 1:1 ratio by functional group of low viscosity diacrylates and high viscosity hexacrylates to both facilitate mixing of the initial thiol-acrylate solution and enable higher acrylate conversions during the stage-2 reaction.

2. Characterizing the mechanical properties

Because the tethered nature of the stage-2 chemistry prevents diffusive mass-transport after a patterned exposure, the material response is invariant to the size or location of the exposed region. Thus, bulk mechanical metrology is sufficient to characterize the material

response. The following describes the results of bulk mechanical testing on the two-stage polymer using the techniques outlined in the previous section. Because a continuum between stage-1 and -2 properties can be achieved by varying the total optical exposure, the mechanical properties are also measured for a range of intermediate stage-1 and -2 states (Figure II-2). Understanding this continuum and its dependence on the applied exposure allows for the design and control of gradient properties within the material.

Due to the relatively low concentration of thiol functional groups, the stage-1 material forms a flexible, loosely crosslinked network ($4 \times 10^{-3} mol/cm^3$) with a T_g well below room temperature (-8 ℃), and a modulus of around 4 MPa (Figure II-2a,c,d). Because of the low crosslink density, the stage-1 sheet can readily absorb NVP, and exhibits swelling strains of up to 26% (Figure II-2a-b), which are necessary to induce sharp folds.

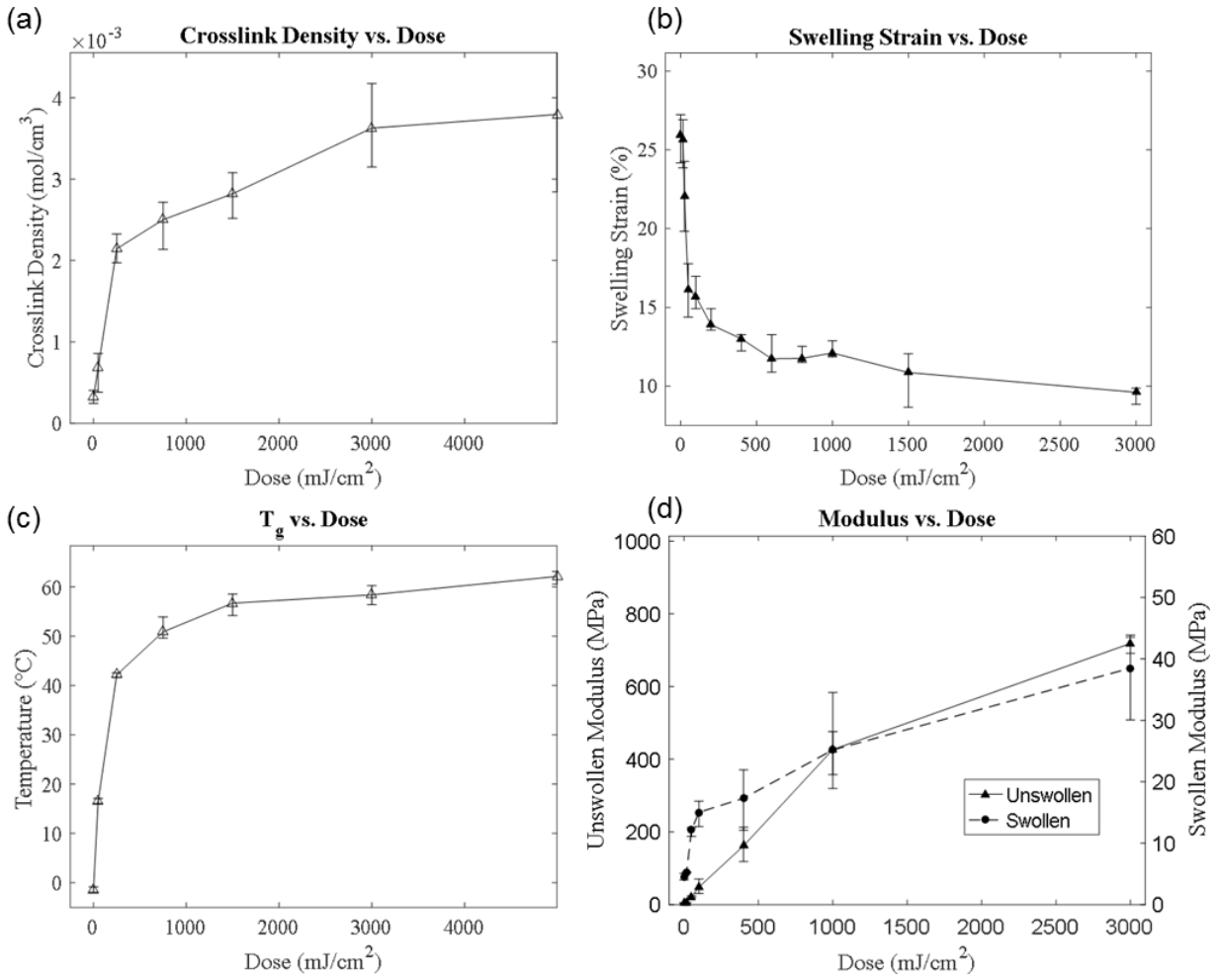

Figure II-2. All exposures were performed using an intensity of $5\,mw/cm^2$ at 365 nm. By controlling the applied irradiation dose at a single intensity, mechanical properties of the polymer may be set anywhere between those of the stage-1 (low dose) and -2 (high dose) networks. (a) The crosslink density of the stage-2 network is roughly an order of magnitude larger than at stage 1. (b) Upon immersion in a solvent, the maximum difference in swelling strain between the stage-1 and -2 networks is about 16%. (c) The glass transition temperature of the stage-1 network is well below room temperature, whereas the stage-2 network possesses a glass transition well above room temperature. (d) The tensile modulus of both the unswollen and swollen network (in NVP) is at least an order of magnitude larger in stage 2 as compared to stage 1.

The second-stage reaction of the material is accessed via irradiation with UV light, which triggers a chain-growth homopolymerization of the remaining unreacted acrylate groups from the stage-1 reaction. Maximum conversion of the residual acrylate bonds, as measured via FTIR, peaks at ~70% and is attributed to the decreased acrylate mobility resulting from the onset of

vitrification and increased network crosslink density [20,66]. At the point of maximum conversion, the crosslink density increases by an order of magnitude compared to the stage-1 network (Figure II-2a), resulting in a T_g much greater than room temperature, and a tensile modulus that is roughly two orders of magnitude higher (Figure II-2c-d). The increased crosslink density also reduces the amount of solvent uptake, restricting the sheet to undergo only 10% swelling strain when immersed in the NVP solvent (Figure II-2b).

Because the two-stage photopolymer utilizes a chain-growth polymerization mechanism, the extent of conversion, and thus increase in tensile modulus, crosslink density, and glass transition temperature, monotonically increases with the number of generated radicals. However, the number of these generated radicals is often nonlinearly dependent on the exposure intensity. Thus, instead of interpolating the intermediate mechanical properties between stages 1 and 2, varying exposure times are used to directly access the intermediate states, which are shown in Figure II-2. In all cases, after exposure the samples are stored in the dark at ambient conditions until dark polymerization terminates.

The above characterization provides the ability to structure the two-stage polymer with arbitrary mechanical properties ranging between the stage-1 and -2 extrema. The only requirement is adequate control over the amplitude and profile of the optical exposure. This characterization will be combined with the intuition from mechanical models to create the folds necessary for complex 3D folded structures via self-actuated origami.

Lastly, solvent evaporation imposes a significant limitation on self-folding structures that utilize swelling-induced actuation. Due to evaporation, the folded, swollen structures are vulnerable to a wide range of environmental conditions such as heat and vacuum. In order to

combat this weakness, the solvent used in the proposed material system is chosen to be a polymerizable monomer/photoinitiator solution consisting of NVP and TPO, such that a uniform light exposure applied immediately after folding polymerizes the monomer. This polymerization step permanently secures the now polymerized solvent within the structure while concurrently mechanically reinforcing the swollen hinges. To quantify this stiffening effect in the hinge regions, initially unexposed polymer strips were swollen in the NVP/TPO solution and then exposed with 11 mW/cm^2, 365 nm light using doses of 990 mJ/cm^2 on each side. Photopolymerization of the solvent increases the tensile modulus of the swollen strip to ~790 MPa, and the T_g of the material to 130 ℃, which is well above the maximum T_g of either the stage-1 or stage-2 networks (Figure II-2c). Through this stiffening process, rigid, permanent, folded 3D structures may be formed.

3. Bending the two-stage polymer

Bending of a two-stage polymer strip is achieved by inducing a depth-wise gradient in the mechanical properties via a single-sided optical exposure (Figure II-3a-c). Immersion of the sheet in a favorable solvent then causes the material to undergo differential swelling and bending (Figure II-3d-f). However, achieving the sharpest fold requires control over the polymer's internal mechanical properties, and a model to understand the optimal patterning of stage-1 and -2 properties. This section first discusses a mechanical model that provides insight into the optimal distribution of stage-1 and stage-2 properties. Then a method is developed, based on the prior mechanical characterization data, and informed by kinetic theory, to predict the development of mechanical properties in response to an arbitrary optical exposure. Using these two tools, the optimal exposure conditions are generated to produce the sharpest folds.

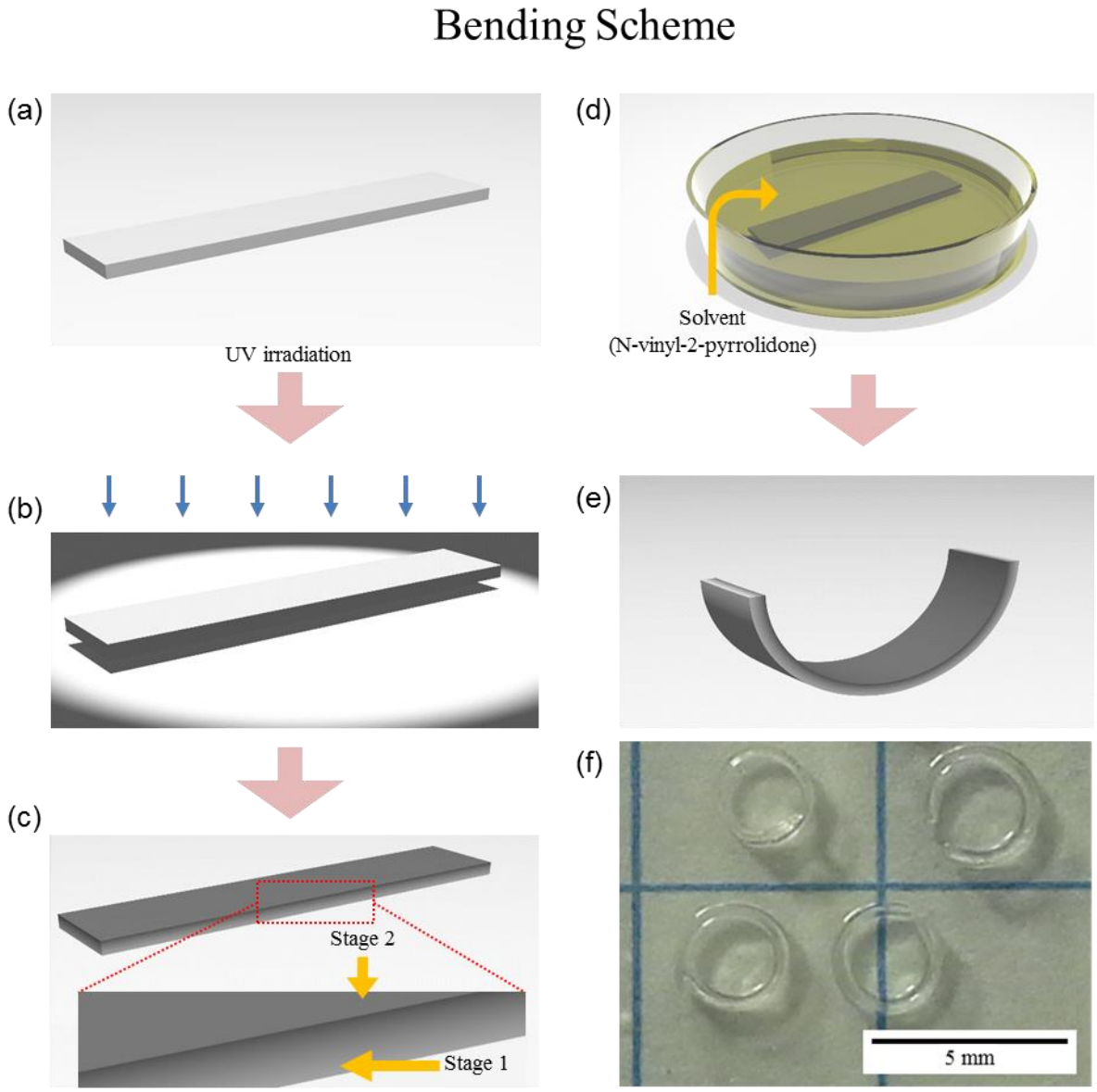

Figure II-3. The scheme used to induce bending in the two-stage polymer. (a-b) A strip fabricated with absorber is irradiated by 365 nm light, creating a gradient (c) in the crosslink density and modulus through the thickness of the material. (d-e) Upon immersion in a solvent (N-vinyl-2-pyrrolidone), the gradient in crosslink density causes the strip to differentially swell, inducing bending. (f) Side-view of the bent strips after removal from the solvent.

A qualitative understanding of the factors that control the bending seen in Figure II-3 is given by the composite beam theory [67]. Because the length to thickness ratio of the samples is 50, the strips are considered slender, and a simple Euler-Bernoulli model is applicable. Under

these assumptions, the bend radius at the center of a thin composite beam subject to differential axial expansion across its thickness is given by:

$$\frac{1}{\rho} = \frac{\int_0^h E\epsilon\left(z - z_N\right)\partial z}{\int_0^h E\left(z - z_N\right)^2 \partial z} \tag{2.3}$$

and

$$z_N = \int_0^h Ez\partial z \Big/ \int_0^h E\partial z \tag{2.4}$$

where ρ is the radius of curvature (ROC), z is the coordinate along the thickness direction, h is the total thickness of the strip, E is swollen tensile modulus, ϵ is the swelling strain, and z_N is the location of the neutral axis. The numerator in the equation above represents the bending moment created by the differential swelling, while the denominator characterizes the bending stiffness.

As shown previously, the tensile modulus and the swelling strain depend on the exposure dose (Figure II-2). Due to the Beer-Lambert law, the incident light intensity undergoes a smooth, exponential decay as it passes through the material, resulting in a depth-dependent dose. Additionally, processes such as saturation of the material response, and a polymerization rate that is sublinear with intensity further alter the resulting distribution of mechanical properties throughout the strip. Thus, a direct mapping between the mechanical properties and the applied dose without accounting for the light intensity cannot be used. To obtain a more accurate estimate of the distribution of material properties across the thickness of the strip, and to improve the bend ROC prediction, the data shown in Figure II-2 is mapped to an "effective dose" $\left(D_{eff\_cal}\right)$ that accounts for the sublinear dependence of the polymerization rate on intensity. This sublinear

dependence with intensity arises from the dominance of bimolecular termination during the polymerization reaction, whereby the polymerization rate scales with the square root of the light intensity (see appendix VIII A). Thus, $D_{eff\_cal} = t\sqrt{I}$ is the product of the exposure time (t) and square root of the light intensity (I). The effective dose as a function of depth within the strip, $D_{eff\_strip}(z)$, is then calculated by first using the Beer-Lambert law to determine the depth-wise intensity profile $\left(I(z)\right)$ and then multiplying by the exposure time. Interpolation of the mapped data from Figure II-2 using $D_{eff\_strip}(z)$ then yields the resulting material properties as a function of depth within the strip:

$$\mathrm{E}(\mathrm{z}) = \mathrm{E}\left(\mathrm{D}_{\mathrm{eff\ \_strip}}(\mathrm{z})\right) \text{ and } \epsilon(z) = \epsilon\left(D_{eff\ \_strip}(z)\right) \tag{2.5}$$

with

$$D_{eff\ \_stript}(z) = t\sqrt{I(z)};\ \ I(z) = I_0 e^{-\log(10)A(z)};\ \ A(z) = \epsilon c z\ , \tag{2.6}$$

where I_0 is the incident light intensity at the illuminated surface of the strip, $A(z)$ is the depth-dependent material absorbance, ϵ is the molar absorptivity of the material, and c is the concentration of absorber. For the $z = 127\ \mu m$-thick strip, $A(z = 127\mu m) = 2.3$ at 365 nm. Note that the z-coordinate is zero at the illuminated surface.

Experimental results for the bend ROC vs. applied dose at the front surface of an isolated $6.35 \times 12.7 \times 0.127$ mm strip are shown in Figure II-4a. The incident light intensity was $5\ mW/cm^2$ for all samples. ROC results predicted by the simple beam theory outlined above are also shown in the inset of Figure II-4a. The beam theory qualitatively matches the experimental measurements, and, aside from differences in ROC values, provides insight into the interplay

between bending stiffness and bending moment, and their effect on the resulting ROC. The computed bending stiffness, bending moment, and location of the neutral axis as a function of applied exposure dose are shown in Figure II-4b-d, while the associated depth profiles of the tensile modulus and swelling strain at select doses are shown in appendix VIII A. Whereas the tensile modulus, and therefore bending stiffness, increase monotonically with the exposure dose, the bending moment and the location of the neutral axis exhibit a more complex relationship with the exposure dose. However, regardless of the applied dose, the location of the neutral axis experiences only small shifts and remains below $z < h/2 = 63.5\,\mu m$. Small doses below $100\,mJ/cm^2$ are insufficient to significantly convert the top surface to stage 2. For these conditions, the difference in swelling strain and tensile modulus about the neutral axis of the strip is small. Thus, the ensuing bending moment is too weak relative to the bending stiffness to deform the beam, resulting in a large ROC. As the exposure dose increases to 100 mJ/cm^2, the front surface is converted to stage 2, however, the back remains at stage 1 due to attenuation of the incident light by the absorber. Initially, this difference in both the swelling strain and tensile modulus about the neutral axis causes the bending moment to grow faster than the bending stiffness, thereby decreasing the ROC. Beyond doses of $100\,mJ/cm^2$, the neutral axis is slightly shifted towards the illuminated surface, indicating an increased difference in tensile modulus between the front and back sides, and even greater conversion of the front surface towards stage 2. This difference in the mechanical properties of the strip about the neutral axis leads to a peak in the bending moment around a dose of $200\,mJ/cm^2$. However, due to continued conversion, the difference in the product of the tensile modulus and swelling strain about the neutral axis decreases, causing the bending moment to experience a small drop, which, combined with the increase in bending stiffness results in an increase of the ROC. Due to the significant attenuation of light intensity at the back surface of the

strip, conversion of the back surface towards stage 2 is slow and the difference in swelling strain and tensile modulus about the neutral axis remains relatively unchanged over the dose range of interest, causing the bending moment to plateau. For an infinite dose, the material would eventually convert to stage 2 and the uniformity in material properties throughout the depth would cause both the neutral axis to shift to the middle of the strip, and the bending moment to fall back to 0.

Overall, the smallest ROC predicted using the simplified beam model and the given experimental parameters is 1.4 mm, or ~11 times the strip thickness, which equates to a factor of 1.4 smaller than the minimum measured ROC (2.0 mm) for the chosen material and strip dimensions. Using a more sophisticated nonlinear finite element model with a Neo-Hookean constitutive material model yields a slightly better prediction of ROC vs. applied dose than the simple Euler-Bernoulli model, however, the same qualitative trend in the ROC is observed (see appendix VIII B). Thus, by using the bulk mechanical characterization data in conjunction with the mechanical modelling, the appropriate exposure conditions to achieve either significant or minimal bending in a hinge can be prescribed.

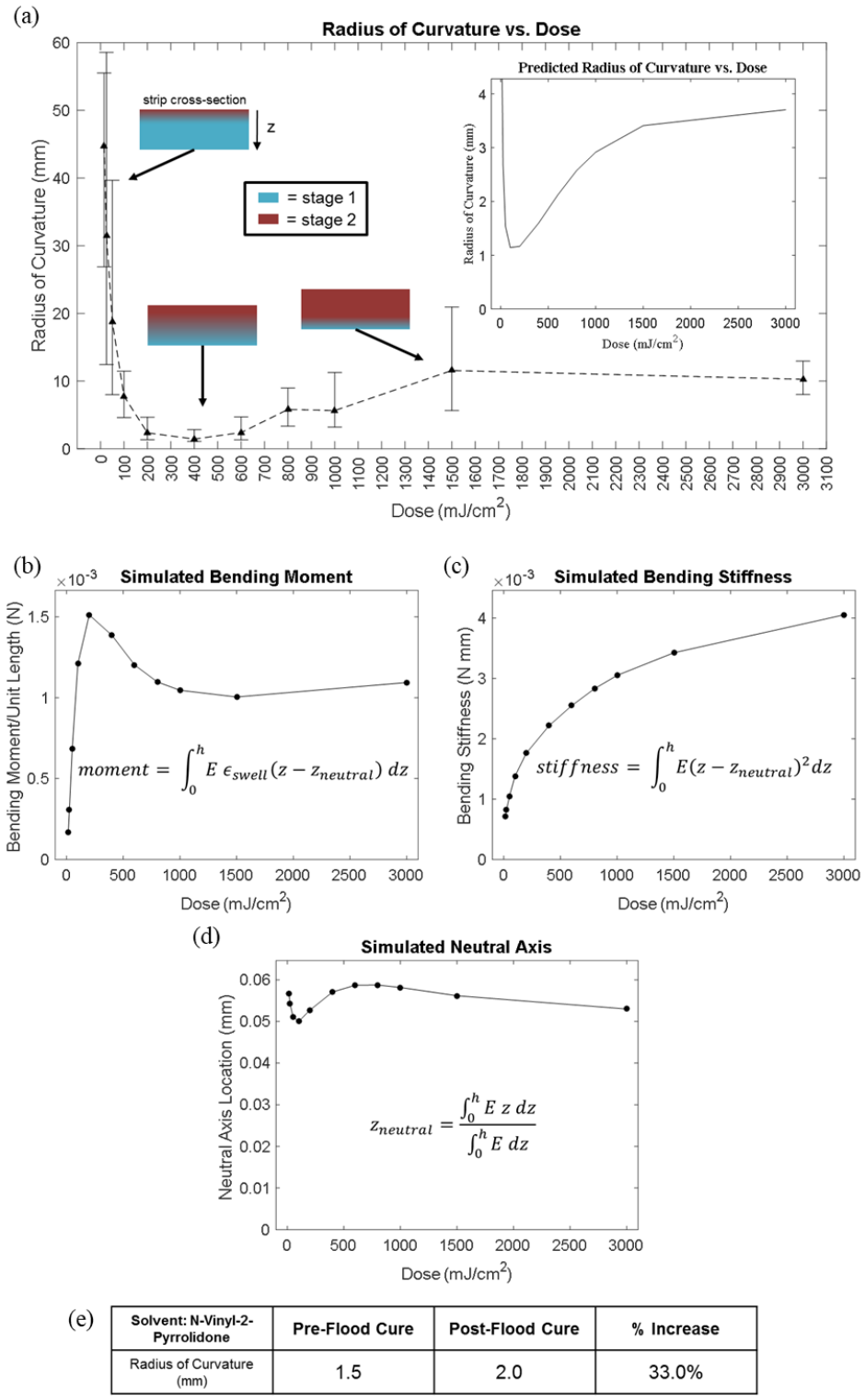

(e)

Solvent: N-Vinyl-2-Pyrrolidone	Pre-Flood Cure	Post-Flood Cure	% Increase
Radius of Curvature (mm)	1.5	2.0	33.0%

Figure II-4. (a) The radius of curvature (ROC) for 6.4 x 1.6 x 0.13 mm strips as a function of exposure dose at 5 mW/cm^2, 365 nm light. The error in ROC measurements becomes large as

ROC ≫ strip length. (Inset) Estimated ROC using the Euler-Bernoulli composite beam model. (b-d) The simulated bending moment, bending stiffness, and neutral axis vs. front exposure dose using the Euler-Bernoulli composite beam model. (e) The radius of curvature increases by up to 33% after the final uniform exposure to polymerize the NVP.

After bending the strip, a final, uniform exposure polymerizes the monomeric solvent and fixes the shape of the bent structure. As shown in Figure II-4e, shrinkage resulting from polymerization of the NVP solvent and remaining unreacted stage-1 acrylates causes the resulting bend radius to increase by up to 33%. However, this shrinkage can be compensated in the initial design of the hinges.

E. Folding 3D Structures

1. Waterbomb base folding process

Unlike bending, where the entire sheet is subject to the swelling response, folding occurs via localized bending of flexible hinges surrounded by stiff panels. In origami, a crease pattern is imposed into an otherwise rigid sheet, creating the flexibility required for the folding hinges while maintaining stiff panels for mechanical strength of the final folded object. In order to demonstrate the capability to accurately pattern folds into the two-stage polymer, a waterbomb base crease pattern utilizing both mountain and valley origami folds is programmed into a $25.4 \times 25.4 \times 0.127$ mm sheet of the material using the process outlined in Figure II-5.

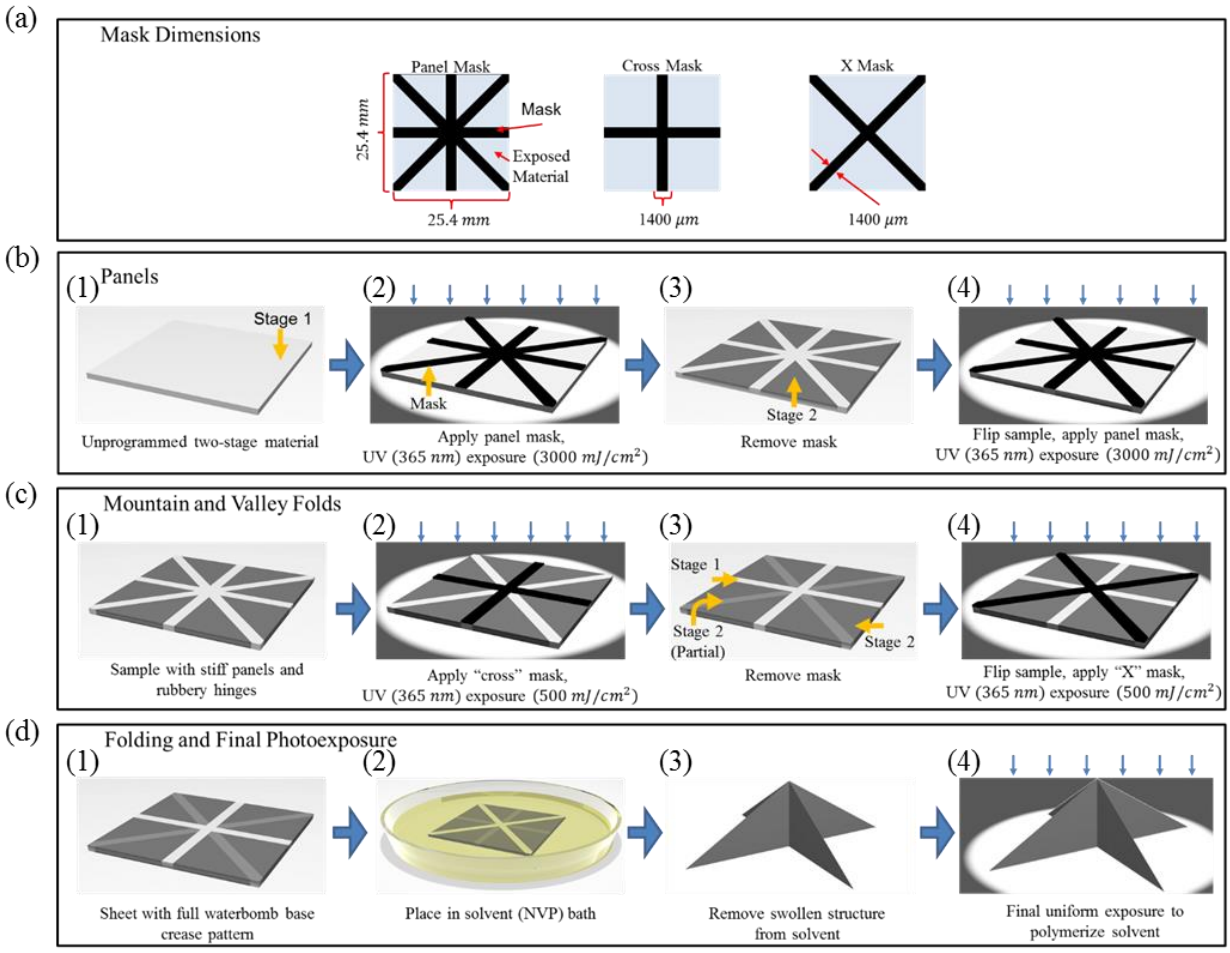

Figure II-5. (a) The masks used to create the waterbomb base structure. Creasing and folding the waterbomb base involves 3 main processing steps: creating the stiff panels, programming the mountain and valley folds, and folding the final structure. (b) Hardening of the panels is performed using large exposure doses applied to each side of the sheet through the panel mask. (c) Mountain and valley folds are created by applying either the "cross" or "X" mask to a single side and using a small exposure dose. Both types of folds may be programmed into the same sheet by applying the two masks to different sides. (d 1-2) Folding of the creased structure occurs upon immersion into a solvent. (d 3-4) A final uniform cure applied to each side of the structure is used to polymerize the solvent and make the final structure permanent.

The folded structure is created using 3 sequential exposure steps that 1) define the stiff panels, 2) define the mountain and valley folds, and (after swelling and folding) 3) lock-in the permanent shape of the folded structure. Each exposure dose is informed by the characterization

and modelling developed in the previous section. Stiff panels with a high modulus and crosslink density throughout their thickness are programmed via high-dose, photomask exposures applied from both sides of the material (Figure II-5b 1-4). The resulting sheet possesses two mechanically distinct regions featuring the stiffened, rigid panels (stage-2 material) and flexible hinges (stage-1 material) (Figure II-5c 1). Mountain or valley folds are then created via small-dose, single-sided mask-exposures applied to select hinges (Figure II-5c 2-4). The small exposure dose establishes a gradient in the mechanical properties that causes nonuniform swelling of the hinge, leading to directed bending/folding. Because these folds remain latent until triggered by solvent, programming of both the mountain and valley folds may be performed on the same 2D surface through masked exposures applied to either side of the sheet. Control over both the width of the hinge and the mechanical gradient is possible by adjusting the mask and exposure dose respectively. After patterning the creases, immersion into a monomeric solvent (NVP) initiates the latent crease program and causes the structure to autonomously fold (Figure II-5d 1-3). A final uniform optical exposure applied to the front and back of the structure polymerizes both the remaining unreacted stage-1 acrylates as well as the NVP solvent, thereby stiffening the hinges and raising the modulus of the entire structure (Figure II-5d 4). Due to polymerization of the solvent within the material, evaporation does not occur, and the structure's shape becomes permanent.

An example of the pre-programmed, unfolded waterbomb base is shown in Figure II-6a. The panels were exposed using 365 nm light from each side with a dose of 3000 mJ/cm^2 at an intensity of 5 mw/cm^2, while the mountain and valley folds were each exposed to 500 mJ/cm^2 on a single side. Optimal hinge width to achieve the sharpest folds was 1.4 mm. Although the pre-programmed sheet exhibits weak bending in the hinges due to polymerization-induced shrinkage

from stage 1 to stage 2, the material remains sufficiently flexible to be pressed against the exposure mask during all programming steps. The folded structure, prior to the final uniform exposure step, is shown in (Figure II-6c-d). In contrast to the isolated bend structures measured in the previous section, the bend radii exhibited by the hinges in the waterbomb base are as small as 0.5 mm. This difference in bending is found to be primarily caused by assistance from swelling-induced buckling in the unexposed vertex at the center of the sheet (see appendix VIII C). As the vertex swells, it is constrained by the rigid panels and is forced to buckle along the hinges. Such buckling assists the folding process in each hinge and promotes a tighter bend radius than that which is normally achieved in an isolated hinge. This assisted folding is made possible by the interaction between the stiff panels and the flexible material at the vertex. For entirely flexible materials with no stiff regions, such buckling does not occur, and the structure will not fold as tightly.

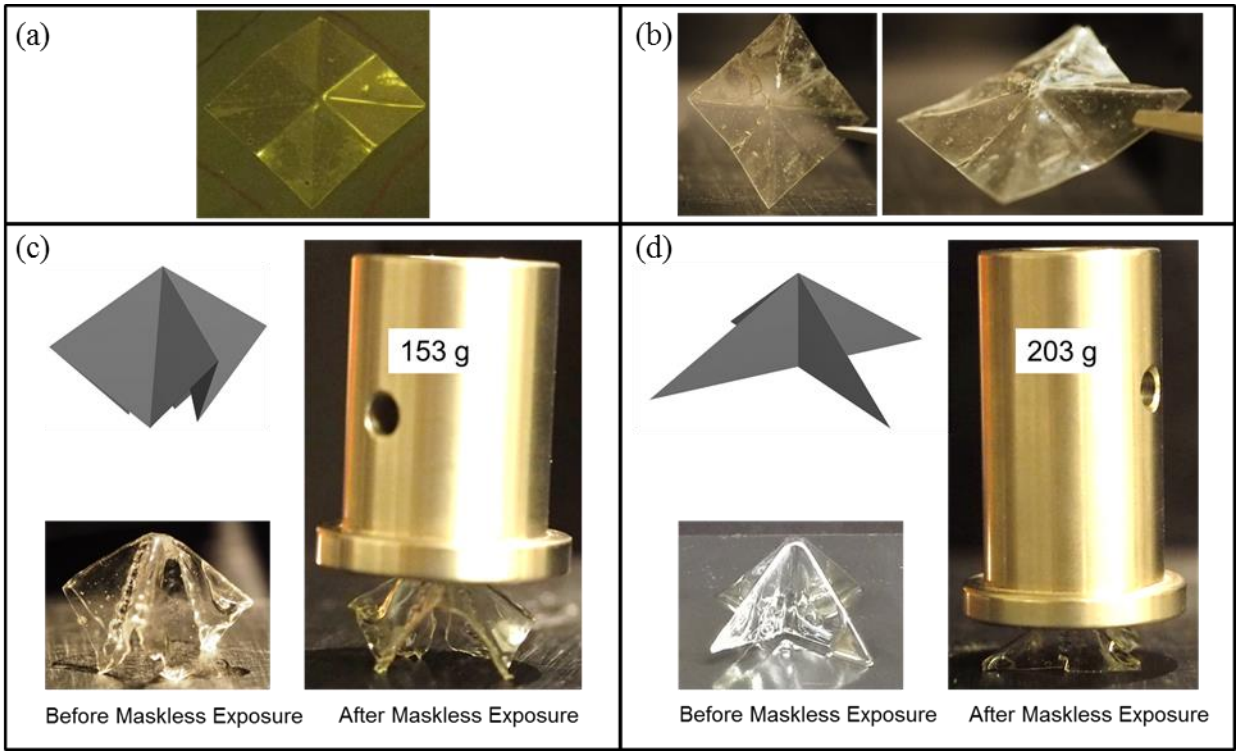

Figure II-6**.** (a) The unswollen two-stage polymer sheet that has been programmed with the waterbomb base crease pattern. (b) If solvent is allowed to evaporate from the folded structure, it will return to a flat sheet. Due to the bistability of the waterbomb base, folding the creased pattern produces 2 different structures. (c,d) The two different bistable states of the waterbomb base are shown along with the experimentally achieved folded structure. If a uniform light exposure is applied to the folded structure immediately after swelling, the structure's rigidity increases and is capable of supporting an external load whose maximum weight depends on the selected bistable structure. The structure in (c) is capable of supporting a maximum load up to 1140 times its own weight while the structure in (d) is capable of supporting up to 1500 times its own weight.

2. Final exposure to lock the shape of the waterbomb base

Evaporation of the NVP solvent causes the folded waterbomb base to eventually return to a flat sheet (Figure II-6b). However, a uniform flood exposure applied immediately after the structure is removed from the NVP bath, before evaporation can occur, causes polymerization of the swollen NVP and locks in the shape of the structure while concurrently reinforcing the hinges. Although some polymerization shrinkage causes the hinges to open and the panel edges to curl, the final shape remains comparable to the initial folded structure. This post-swelling

photopolymerization step thus acts as a trigger to allow solvent to either evaporate and enable reversible folding, or to polymerize and create a permanent structure.

Evaporation of the NVP solvent causes the folded waterbomb base to eventually return to a flat sheet (Figure II-6b). However, a uniform flood exposure applied immediately after the structure is removed from the NVP bath, before evaporation can occur, causes polymerization of the swollen NVP and locks in the shape of the structure while concurrently reinforcing the hinges. Although some polymerization shrinkage causes the hinges to open and the panel edges to curl, the final shape remains comparable to the initial folded structure. This post-swelling photopolymerization step thus acts as a trigger to allow solvent to either evaporate and enable reversible folding, or to polymerize and create a permanent structure.

Due to the extra post-swelling polymerization step, the tensile modulus and T_g of the polymer structure's hinges greatly increase, reaching values as high as 790 MPa and 130 ℃ respectively, thereby allowing the structure to support an external load. This was demonstrated by applying a series of increasing weights to the structure, with the maximum loading weights shown in Figure II-6c-d. The maximum recoverable loading of the flood-cured, 0.134 g waterbomb base is 203 g, which is ~1500 times its own weight. It is important to note that the geometry of the waterbomb base crease pattern allows for two different stable structures [68] (Figure II-6c-d) which arise from the single degree of freedom allowed by the flexible, unpatterned material at the vertex of the mountain and valley folds in the center of the square sheet. Due to their final geometries, the maximum supportable load of these two bistable structures is different. The structure in Figure II-6c, which is only supported by 4 narrow points, can bear up to 1140 times

its weight, while the alternate structure in Figure II-6d, which is instead supported by the edges of the polymer sheet, can support up to 1500 times its own weight.

F. Conclusion

By designing a two-stage photopolymer that incorporated tethered stage-2 chemistry, I demonstrated the ability to predict and control its 3D mechanical properties through bulk metrology and photopatterning. Critically, the validity of this technique was enabled by the unique nature of the tethered stage-2 chemistry, which prevented diffusion-induced hysteresis and provided spatio-temporal invariance in the material response. Assisted by this characterization, I utilized 3 distinct patterning modalities within the photopolymer that are amenable to the creation of permanent, rigid origami structures: 1) uniform patterning in depth to produce stiff, rigid panels, 2) strong gradients in depth to create directed self-folding hinges, and 3) permanent fixation of the final structure's shape via a uniform optical exposure. The latent nature of the crease pattern allowed all processing to be performed on the 2D sheet using mask lithography, while actuation occured at a later time through application of an external stimulus. Using these steps, I demonstrated the ability to fabricate a self-folding, permanent, rigid waterbomb base capable of supporting loads up to 1,500 times its own weight. I also observed that constrained swelling imposed by the rigid panels on the unpatterned regions could be used to assist the bending of hinges and enhance the overall folding of the programmed crease pattern. In the waterbomb base structure, constrained swelling of the central unpatterned vertex allowed for bend radii that were a factor of 3 smaller than isolated bends created on individual strips. In summary, the combination of a two-stage polymer and facile optical programming demonstrated herein enables stiff panels separated by mountain and valley creases that undergo folding and final hardening in response to simple, delayed external stimuli. These features enable complex

patterns of sharp folds in otherwise flat sheets to create mechanically and environmentally robust final parts, avoiding the common issues of precise stimulus control, pliable final state, and impermanent shape.

In the following chapters, I will explore systems that incorporate untethered stage-2 chemistry and are subject to diffusion-based mass transport. Through this diffusion, unique avenues for amplifying the material's stage-2 properties will be made accessible, however, bulk metrology can no longer accurately characterize the material response. Therefore, I will present the development and application of in-situ metrology for characterizing and unlocking the full potential of such diffusion-based two-stage photopolymers.

CHAPTER III
IN-SITU METROLOGY OF REFRACTIVE INDEX STRUCTURES THROUGH QUANTITATIVE PHASE IMAGING[1]

A. Chapter Overview

In the previous chapter, tethering the stage-2 species to the stage-1 network eliminated their diffusive mobility and provided both spatial and temporal invariance in the material response under patterned optical exposures. Thus, bulk metrology could accurately characterize and predict the in-situ material properties of a photostructured feature. However, when the stage-2 chemistry is untethered from the matrix, as in the case of two-chemistry holographic photopolymers, mass transport through diffusion now couples each photopatterned structure to the surrounding network. In this situation, the assumption of spatial and temporal invariance is no longer valid, and bulk metrology will fail to accurately characterize the material properties of internal photostructured features. In this chapter, I develop an in-situ imaging technique to characterize features written into diffusive, two-stage holographic photopolymers [69]. Unlike previous methods that ignore the complete spatial frequency spectrum of the structure (holography) or only measure the optical path length (quantitative phase imaging), this technique combines confocal reflection microscopy and quantitative phase imaging to completely resolve the spatial frequency spectrum and Δn of 2D photostructured phase elements. Using the characterization data from this technique, I can then predict the Δn of arbitrary in-situ photopatterned phase structures. This technique will then be used in chapter IV to explore new photostructuring methods to amplify the Δn response in holographic two-stage photopolymers.

[1] Adapted with permission from Opt. Express 26, 1851-1869 (2018). Copyright (2018) Optical Society of America. (Bibliography reference: [69])

B. Introduction

Direct laser writing (DLW) optical lithography is a common technique used to create micron-scale three-dimensional (3D) refractive index structures deeply buried within a photosensitive medium [6,70,71]. The primary applications of DLW have been 3D routed waveguides for interconnects to integrated optoelectronic circuits [6,72–75], 3D diffractive optics that provide greater control over the multidimensional coherence function than their 2D counterparts [4], and 3D optical data storage that extends the capacity of traditional surface recording [76,77]. Proper design for such applications demands the ability to understand this light/matter interaction, which includes characterizing the optical properties of both the focused writing beam and photosensitive material, and measuring the magnitude and shape of the resulting index response.

Inorganic photosensitive materials such as photorefractive crystals or photosensitive glass offer the ability to create non-volatile embedded refractive index structures through a post-processing thermal treatment, while offering reasonable one-photon sensitivity for DLW and holographic patterning [10,78,79]. Alternatively, the refractive index of most transparent amorphous or crystalline inorganic material can be modified at the focus of a sufficiently high intensity femtosecond pulse train [9,80]. However, the mechanism by which these structures are formed is often complex [81] and inhibits the ability to accurately predict the shape and magnitude of the index response without performing extensive metrology. The lack of such predictive models limits the ability to design single-mode waveguides, control the scattering profile of volumetric diffractive optics, or predict the data storage density of an optical disk.

In contrast to their inorganic counterparts, organic materials such as polymers provide synthetic routes to a vast range of optical and mechanical properties. Typically, absorption of

single or multiple photons by a photoinitiator molecule generates radicals or cations, which initiate monomer conversion to polymer. DLW lithography has been used to locally induce this monomer polymerization and form refractive index structures through the resulting material densification. However, formulations consisting of a single monomer species generally have minimal index response, as the initial localized polymerization is followed by a uniform bulk cure to render the material environmentally stable. To circumvent this issue, formulations typically mix high and low refractive index components whose fractional composition, and thus refractive index, is modified via mass transport when exposed to patterned illumination, but left nominally unchanged by the uniform post-processing cure [14]. The high photo-sensitivity of these two-component photopolymers, and their ease of processing, have led to applications in holography, 3D data storage [22], self-written waveguides [5,82], and laser direct-write lithography of waveguides [75,83,84]. Although the holographic community has invested significant effort both into developing a rational design for the material and understanding the index response to sinusoidal illumination [85–89], little has been done to quantitatively predict how these two-component photopolymer materials respond to arbitrary intensity patterns including the focus of a DLW system.

Thus, accurate measurements of the gradient index profile of both inorganic and organic photosensitive materials in response to single- or multi-photon absorption at a stationary or continuously moving laser focus is critical to enable a wide range of optical applications. This is an open problem fundamentally because quantitative metrology of weak (index contrast ~10^{-3}) and small (feature width ~wavelength) buried 3D phase objects is a challenging task. In particular, all 3D optical metrology methods have a finite coherent transfer function (CTF) which will fail to accurately measure the peak or profile of the index response unless the object spatial frequency

spectrum is completely within the instrument CTF. For example, Bragg diffraction from holograms written by two-beam interference and analyzed with Kogelnik's coupled wave theory [90] only measures the first harmonic of the periodic illumination, losing information about the higher orders and their contribution to the peak index. Digital holographic microscopy [91,92] and diffraction-based phase retrieval [93,94] have been applied to reconstruct buried waveguide profiles, however, in the case of perpendicular-write waveguides, the methods are constrained by poor overlap of the microscope CTF with the waveguide spatial frequency spectrum. Thus, further preparation of the sample, either via cross-sectioning, or the use of additional assumptions about the shape of the waveguide is required to measure the full index profile.

Alternatively, a method similar to that of the ascending scan technique used to measure the relationship between the writing beam focus and the 3D voxel shape of solidified two-photon polymerized structures [95] can be used to improve the overlap of the CTF and the waveguide's spatial frequency spectrum. The writing beam focus begins within the substrate, and a series of phase structures are created, shifting the focus upwards from the substrate by an amount Δz between each structure (Figure III-1). Because the substrate effectively truncates the focus spot in the z-dimension, measuring the differential optical path length (OPL) between each structure provides, thin, 2D slices that can be used to reconstruct the full 3D phase profile. Since each differential 2D slice is considered uniform in depth, all spatial frequency content collapses onto the $f_z = 0$ plane and falls within the CTF of a high NA microscope. Unfortunately for small voxels, the signal-to-noise ratio for the differential OPL between each z-shifted voxel is typically lower than the sensitivity of the phase imaging system, restricting the applicability of this scan to large, or strong phase structures. However, by adapting this technique to instead use thick, uniform 2D phase slices to study the material's light-induced index response over a range of different exposure

conditions, I gain enough information to generate a predictive model for arbitrary 3D exposure conditions.

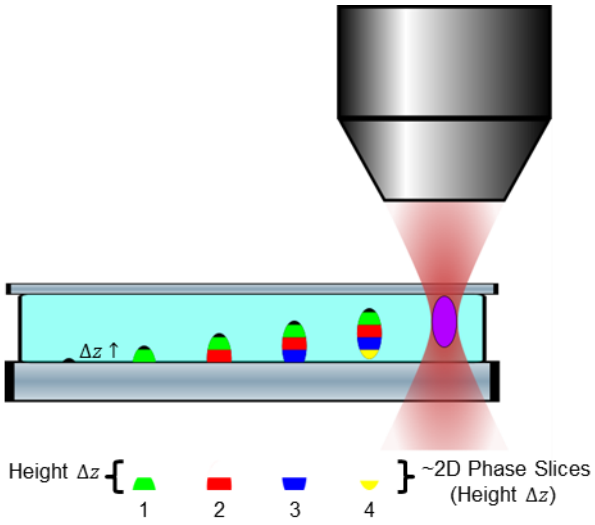

Figure III-1. The shape of 3D phase structures written into a material using either two-photon polymerization or a thresholded single-photon polymerization response can be measured using the ascending scan method. The focus of the exposure beam is shifted by an amount Δz between each exposure until the substrate no longer truncates the resulting phase structure. Phase imaging can then be used to measure the differential optical path length between adjacent structures. Because these thin phase slices are assumed to be uniform in z, the spatial frequency content of each slice falls entirely within the CTF of the imaging system. Therefore, measuring each of the differential slices in the 3D structure allows one to reconstruct the entire voxel.

As demonstrated in the following section, incomplete overlap between the object spatial frequency spectrum and the imaging system's CTF prevents accurate reconstruction of many 3D refractive index structures such as embedded waveguides. Therefore, I propose to fully characterize the index response of photosensitive materials by creating refractive index structures in a geometry that guarantees CTF overlap. I then apply this predictive model to the design of structures such as buried waveguides, whose complete spectrum does not overlap with the CTF, and is not accessible outside the material. The problem of CTF overlap is solved by imaging a transverse slice of a waveguide with a high NA transmission microscope. Although techniques such as refractive near-field scanning [96] have been used to probe the entire 2D refractive index

profile of waveguides using this geometry, they require point-by-point scanning over the entire waveguide face, which is inconveniently slow for the multi-parameter materials characterization scheme proposed here. Full field, intensity-based phase imaging schemes such as iterative phase retrieval [93], digital holographic microscopy [97], and the transport of intensity equation (TIE) [98] offer significantly faster and simpler measurements. Unfortunately, iterative phase retrieval is sensitive to support constraints and does not always guarantee convergence to a global solution, whereas digital holographic microscopy is subject to coherent noise artifacts. In contrast, TIE-based phase retrieval, developed by Teague [99], provides a direct and unique measurement of the transmitted phase, which is equal in the Born approximation to 2D integrated optical path length. However, to calculate refractive index from transmitted phase requires additional 3D information about the structure. For example, although previous work combined TIE-based phase imaging with diffraction tomography to estimate both the shape and refractive index of buried waveguides [98], the CTF of the imaging system used in this geometry was again insufficiently matched to the spatial frequency spectrum of the object, preventing a direct, quantitative measure of peak index or shape.

In this chapter, I demonstrate rapid and complete quantitative characterization of isolated index structures written by direct-write lithography using a combination of TIE-based quantitative phase imaging and confocal reflection microscopy. By aligning the CTF of the transmission microscope with the spatial frequency spectrum of thin 2D test structures, I am able to measure the relevant spatial frequency response of the material and use this to unambiguously reconstruct the complete Δn profile without the need to perform tomographic measurements. The validity of this technique is demonstrated by fully characterizing the direct-write index response of a high performance holographic photopolymer. Counter to the predictions of radical photochemistry, the

material is shown to behave linearly with intensity over a wide range of exposure intensities and times. Furthermore, the index response is found to fall on a single master curve, which provides a unique functional translation between integrated exposure dose and index response. I then show that this function can be used to predict the size and shape of written waveguides, including the nearly binary structures that can be created using the sharp saturation of the response function. This technique is experimentally simple and applicable to any photosensitive material with single- or multi-photon response, enabling the rational design and optimization of writing systems, materials, and 3D optical devices, including waveguides, volume computer generated holograms, and data storage systems.

C. Theory and Experimental Details

1. Overlap between the object spatial frequency spectrum and the imaging CTF

To illustrate the impact of mismatch between the object spectrum and the CTF, consider an ideal phase imaging system [Figure III-2(a)] operating in transmission. Independent of the specific imaging method, an instrument with a finite signal-to-noise ratio can only measure the fraction of the object spectrum within the CTF [Figure III-2(b)]. Now let this system be used to examine a buried waveguide written by moving the focus perpendicular [Figure III-2(c)] or parallel [Figure III-2(d)] to the axis of the focus. For purposes of illustration, the circularly-symmetric waveguide refractive index profile in both cases is chosen to be of similar shape as one demonstrated later in this chapter.

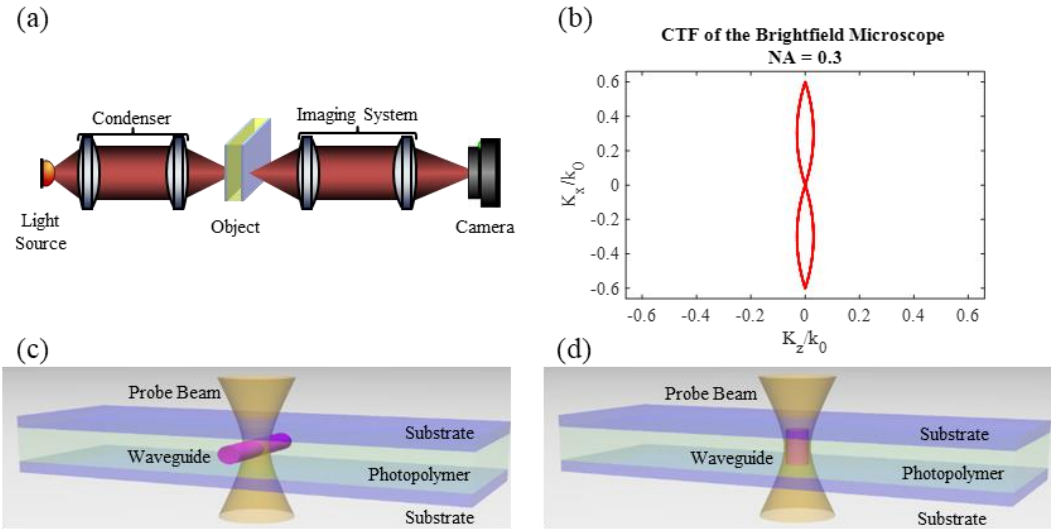

Figure III-2. (a) Transmission microscope used to image the phase object. (b) Example of an ideal CTF for the transmission microscope configuration used in all of the following experiments, operating under coherent illumination with a 0.3 NA in a material with a refractive index of 1.5. (c-d) Measurement geometry for imaging perpendicular and parallel-write waveguides respectively.

As shown in Figure III-3(c), the spatial frequency spectrum of the perpendicular-write waveguide poorly overlaps the CTF, particularly in the z-direction, independent of the microscope NA. An ideal reflection microscope has even worse overlap, particularly with structures written via laser direct-write lithography [100]. Conversely, the microscope CTF can effectively overlap the spectrum of a waveguide written by moving parallel to the axis of the focus [Figure III-3(d)] if the diffraction-limited spot size is smaller than the smallest written feature size. Crucially, the delta-function spectrum of a waveguide that is invariant in the z direction fits within the z-axis singularity of the transmission microscope CTF. Assuming an ideal reconstruction wherein the CTF is constant, the measured waveguide in the former case has little resemblance to the object, appearing to have a uniform cross section in z and a peak amplitude of only 15% of the actual structure [Figure III-3(e)]. Conversely, the latter geometry perfectly reconstructs both the profile and the peak refractive index [Figure III-3(f)]. Therefore, in order to accurately reconstruct the

object, the CTF of the imaging system must fully overlap the spatial frequency spectrum of the object.

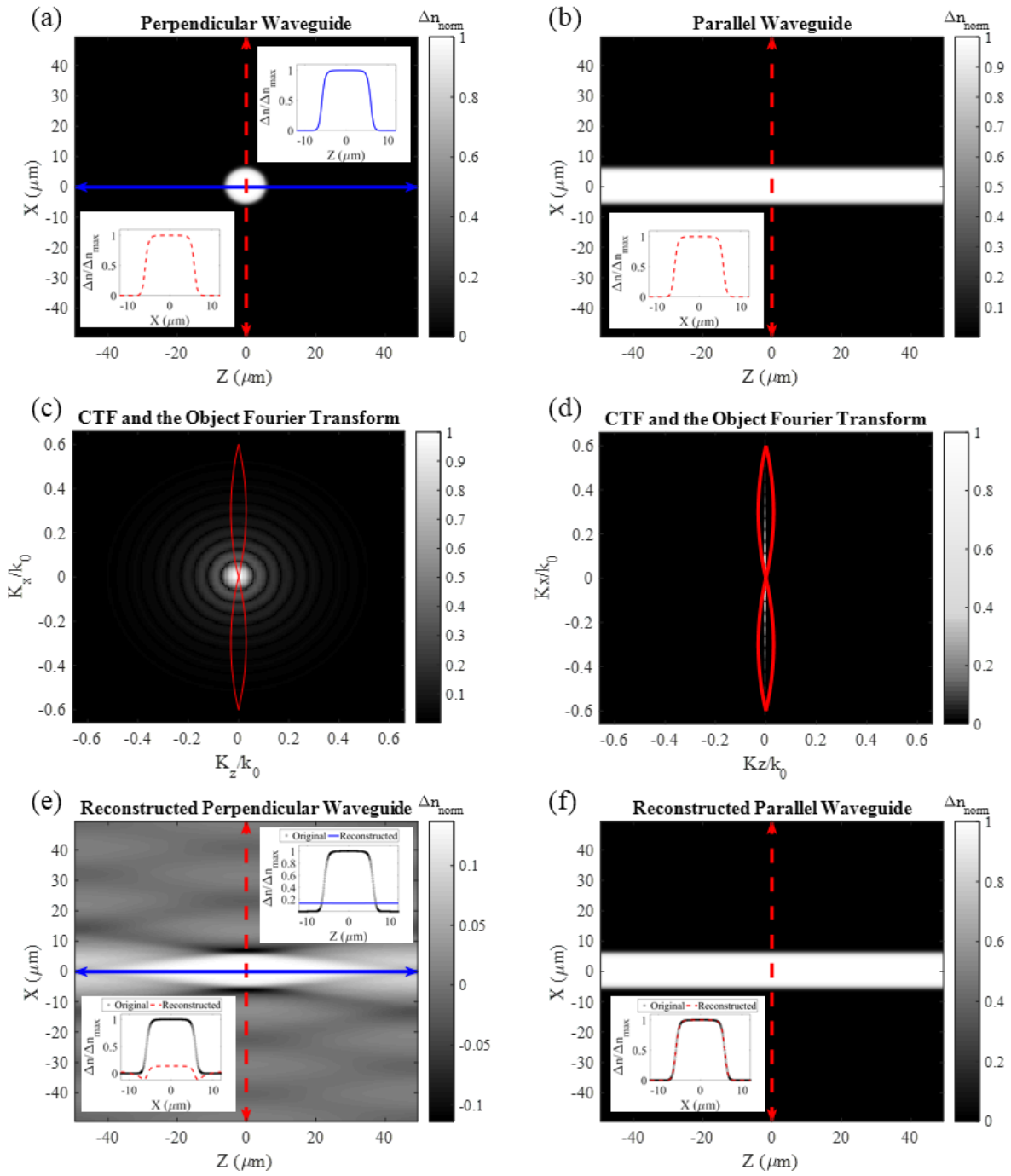

Figure III-3. (a-b) 2D image of the normalized refractive index distribution seen by the instrument from Figure III-2(a). The insets show the cross-sections along the respective lines. (c-d) Overlap of the object's Fourier transform with the CTF (line) of the ideal imaging system from Figure

III-2(b). The Fourier transform amplitude shown has been scaled by taking the square root and then normalizing the amplitude in order to show the structure more clearly. (e-f) The resulting reconstructed object using only the Fourier components that overlap with the CTF of the imaging system. The insets compare the ideal cross-sections seen by the microscope along the respective lines with the actual object cross-sections (black squares).

2. Two-component photopolymer formulation

The two-component holographic photopolymer used in this chapter is a gel consisting of a low refractive index, optically transparent, flexible matrix polymer swollen with a liquid photoreactive writing chemistry that consists of a photoinitiator and a high refractive index writing monomer [14]. Photons absorbed by the photoinitiator begin polymerization of the monomer, creating a local concentration of high refractive index polymer within the matrix. After re-equilibration of the unreacted monomer via diffusion, and the matrix via swelling, the resulting concentration variations of the low-refractive index matrix and high-refractive index polymer yield a difference in the refractive index (Δn), given by the volume-fraction weighted average of the constituent refractive indices [21]. A final uniform cure polymerizes all remaining monomer, preventing further mass transport, and resulting in minimal change to the bulk refractive index. Depending on the end-application, different chemical formulations have been developed to address the required material properties. Covestro and DuPont have both developed high dynamic range photopolymers with Δn's ranging from >0.03 to 0.06 for the Bayfol HX and OmniDex formulations respectively [101,102]. These high Δn's allow for the production of thin, volume holograms [7]. However, the high Δn typically comes at the expense of increased shrinkage (1.4% for the Bayfol HX [101]), which is unsuitable for multiplexed holographic data storage. Using their DRED formulation, Akonia Holographics has demonstrated a low-shrinkage version of a two-component photopolymer (<0.1%) for holographic data storage with a zero-to-peak Δn as high as 0.015 [103]. Although predictive models have been developed to describe the formation

of periodic holographic phase structures within such materials [104], to the best of our knowledge, little work has been done to model the material response when writing isolated phase structures such as waveguides.

The writing monomer used in the model two-component photopolymer is phosphorothioyltris(oxybenzene-4,1-diylcarbamoyloxyethane-2,1-diyl) triacrylate, and was synthesized following a procedure reported in various Covestro patent literature [105]. First, 0.0207g (0.09 mmol) of 2,6-di-tert-butyl-4-methylphenol and 57 mL of Desmodur RFE (27% solution of tris(p-isocyanatophenyl) thiophosphate in ethyl acetate, 38.9 mmol) were added to a dried 100 mL round bottom flask with a magnetic stir bar. The reaction was started by adding 13.5 g (116.3 mmol) of 2-hydroxyethyl acrylate to the flask dropwise, and was performed at 60 °C with a reflux condenser overnight. The product was collected by cooling and subsequent removal of ethyl acetate in vacuum to obtain a waxy semicrystalline solid. In order to form the photoreactive component of the photopolymer, a 1:10 molar ratio of photoinitiator TPO (2,4,6-Trimethylbenzoyl-diphenyl-phosphineoxide) to the writing monomer was used.

The crosslinked matrix of the two-component photopolymer system is a flexible polyurethane with a glass transition temperature (T_g) of -45 °C , and consists of a 1:1 molar ratio of isocyanate (Desmodur N3900) and alcohol (polycaprolactone-block-polytetrahydrofuran-block-polycaprolactone). In the following experiments, formulations with overall weight fractions of 10% and 30% of the photoreactive components were used. Test samples were fabricated by mixing the matrix and photoreactive components at 60 °C , prior to gelation of the polyurethane, degassing the resin, and then casting between a 1 mm glass microscope slide and a 150 μm glass coverslip. Sample thickness was set using spacers ranging between 13 and 25 μm. Polymerization of the urethane matrix occurred overnight in an oven at 60 °C .

3. Exposure and confocal reflection system

The optical layout shown in Figure III-4 is used to fabricate the sample phase elements for TIE-based imaging and analysis. The sample is mounted on a 5-axis stage that controls both tip/tilt and xyz motion, while a confocal reflection microscope operating at 660 nm is used to align the sample and provide a non-contact method for precisely measuring the thickness of the sandwiched photopolymer layer. The confocal beam is co-aligned with a second laser at 405 nm central wavelength that is used to expose the photopolymer. Because the chosen photoinitiator is minimally absorptive at 660 nm, the confocal imaging system will not initiate significant polymerization and can therefore make optical path length measurements at the direct site of the exposure. The known refractive index of the photopolymer at this wavelength, measured with a Metricon Model 2010 prism coupler, is used with the optical path length measurement to calculate the thickness of the sample. When performing quantitative phase imaging of a 2D profile, this thickness measurement is necessary for determining the actual Δn from the measured optical path length. A 0.66 NA objective is used in conjunction with a 10 μm pinhole to give a confocal axial resolution of ~2 μm within the material [106] and a thickness uncertainty of ±2.5%. Sufficient signal-to-noise in the confocal reflection measurement is obtained for a refractive index difference of ~0.01 between the polymer and the protective substrate.

At each location, the thickness of the sample is measured by the procedure above, then the 405 nm light beam exposes a series of 2D, isolated gradient index structures into the material using a range of intensities and exposure times. Each structure extends uniformly through the entire thickness of the polymer film. The small size of the structures and high stiffness of the glass coverslip relative to the rubbery polymer are presumed to prevent change of thickness due to polymerization shrinkage or swelling of the matrix. Before exposure, the 0.66 NA objective is

replaced with a 0.13 NA, 4× Nikon objective operating at an effective NA of 0.023 to provide a focused spot 1/exp(2) intensity diameter of ~18 μm. The total beam power is controlled using both the driving current and a variable ND filter in order to achieve a large range of intensities. Exposure time is controlled using a Uniblitz VS14 shutter with a minimum equivalent exposure time of 4.5 ms. Three points are written for each exposure condition to provide error bars.

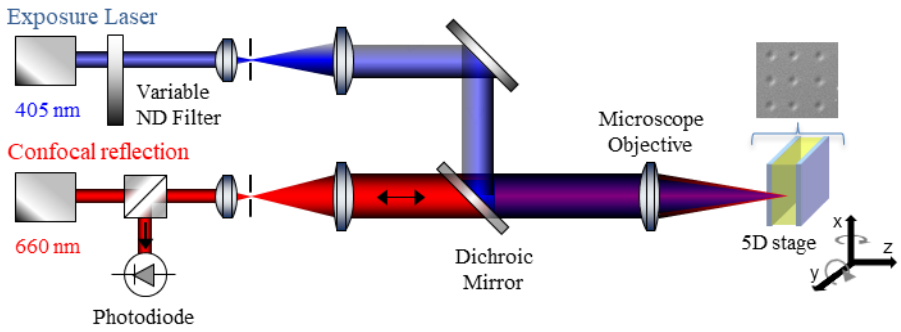

Figure III-4. The confocal reflection microscope (660 nm path) is used to position and measure the sample thickness, while the co-aligned 405 nm laser is used to expose the photopolymer and create phase structures (inset shows an example differential interference phase contrast microscopy image). The 660 nm laser is a 100 mW Coherent OBIS LX diode laser, and the 405 nm laser is a Power Technology Incorporated IQu2A105/8983 105 mW laser.

4. Phase imaging

The refractive index contrast between the written phase structures and the base matrix is measured using a non-interferometric phase imaging technique based on the solution of the transport of intensity (TIE) equation

$$-\frac{2\pi}{\lambda_0}\frac{\partial \mathrm{I}(\mathrm{r}_\perp,\mathrm{z})}{\partial \mathrm{z}}\bigg|_{z=0} = \nabla_{\mathrm{r}_\perp}\left[\mathrm{I}(\mathrm{r}_\perp,\mathrm{z}=0)\nabla_{\mathrm{r}_\perp}\Phi(\mathrm{r}_\perp,\mathrm{z}=0)\right] \tag{3.1}$$

where $\mathrm{I}(r_\perp, z=0)$ is the in-focus image intensity distribution perpendicular to the optical axis ($\hat{z}$), and λ_0 is the wavelength of the incident light (vacuum). The optical path length along the optical axis is $\Phi = k_0 \mathrm{nL}$, where $k_0 = 2\pi/\lambda_0$, n is the refractive index of the material, and L is the

thickness of the structure. In order to solve the TIE, a series of Fourier transforms $(\mathcal{F})$ are applied as shown in Eq. (3.2) and (3.3) [107,108]:

$$\Phi\left(r_{\perp}, z\right) = -\mathcal{F}^{-1}\left[\frac{\mathcal{F}\left(\nabla_{\mathrm{r}_{\perp}} \mathrm{I}^{-1}\left(r_{\perp}, z=0\right) \nabla_{\mathrm{r}_{\perp}} \Psi\left(\mathrm{r}_{\perp}, \mathrm{z}\right)\right)}{4\pi^2\left(f_x^2 + f_y^2\right)}\right] \tag{3.2}$$

where

$$\Psi\left(r_{\perp}, z\right) = \mathcal{F}^{-1}\left[\frac{\mathcal{F}\left(k_0 \frac{\partial I}{\partial z}\right)}{4\pi^2\left(f_x^2 + f_y^2\right)}\right] \tag{3.3}$$

and f_x, f_y are the spatial frequency components of the image. Aside from the wavelength of light, only knowledge of the axial intensity derivative is required. Because the axial intensity derivative can be estimated with a series of defocused images, and the TIE does not suffer from strict coherence requirements of the illumination source, this technique offers a simple method for direct phase measurements [109,110]. In the following experiments, imaging to determine the axial intensity derivative is performed with a conventional brightfield microscope equipped with a 633 nm line filter, a 20×, 0.5 NA objective, and a condenser operating at 0.3 NA to broaden the linear spatial frequency response range of the TIE [111]. The axial derivative is approximated via a second-order central difference approximation using a pair of symmetrically defocused images about the in-focus image plane. The detector noise in this approximation sets a limit on the minimum defocus distance, while the error associated with the second-order finite difference approximation imposes a competing limit on the maximum defocus distance [112,113]. Although a variety of techniques exist to reduce this noise, most commonly by acquiring larger sets of defocused images, a single pair is found to be sufficient [114–116]. The optimal defocus distance that minimizes the noise from both the axial intensity derivative approximation and that associated with the nonlinear error from the TIE approximation occurs at the distance where the peak Δn

begins to decrease. A defocus distance of ±3 μm around the object plane using a piezo actuator provides the best experimental results for the given setup (Figure III-5).

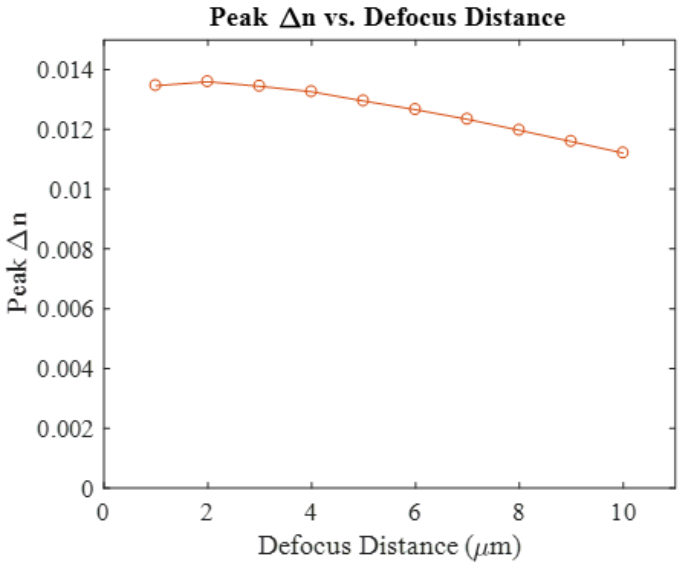

Figure III-5. The reconstructed Δn vs. defocus distance used in the TIE reconstruction algorithm. As the defocus distance increases beyond 3 μm, the TIE algorithm suffers from error due to discarded higher-order terms.

Additionally, because fast Fourier transforms are used to solve the TIE, periodic boundary conditions are assumed. While the addition of an aperture at the image plane can be used to bypass this assumption [117], the imaged phase structures in the following experiments are sufficiently isolated that the phase difference falls to 0 at all of the boundaries, thereby satisfying the required boundary condition. Finally, because the depth of field of the writing illumination is significantly larger than the thickness of the sample, and the absorption of the sample is insignificant over these thicknesses, the index of refraction of the written phase elements is uniform throughout the thickness of the sample. In other words, I measure here the response of the polymer to a stationary focus. One could also translate the focus through the thin sample of photosensitive material to simulate the continuous translation of a waveguide writing experiment. In either case, the index distribution is invariant in the axial direction and the object spatial frequency distribution is thus

confined to the plane $f_z = 0$. This guarantees no loss of information outside of the transmission microscope CTF as long as the NA of the objective used for TIE is much greater than that used for writing (Figure III-3).

With this geometry, the only 3D knowledge required to translate the phase measurement to the complete 3D refractive index profile is the precise thickness of the sample, which is provided by the integrated confocal reflection microscope. An example of the calculated refractive index structure for a Gaussian exposure is shown in Figure III-6.

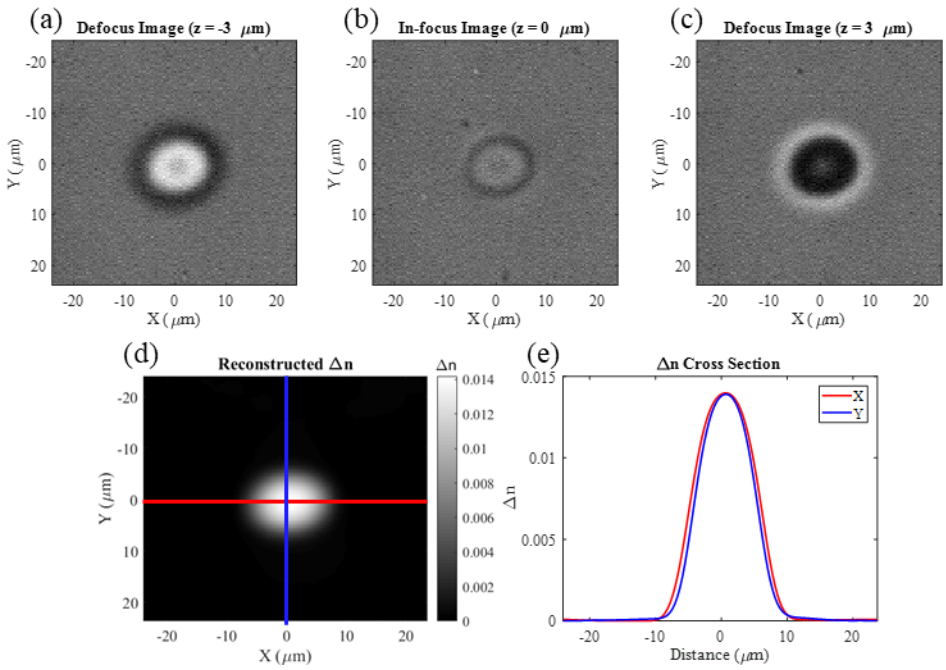

Figure III-6. (a-c) Example brightfield images required for solving the TIE, including two symmetrically defocused images (a,c) and one in-focus image (b). (d) The 2D reconstructed Δn using the images from (a-c) along with representative (e) cross-sections taken along the x- and y-axes.

Verification of the TIE algorithm was performed by characterizing the measured height profile of a fused silica microlens array (Suss MicroOptics) using both the TIE algorithm and atomic force microscopy (AFM) as seen in Figure III-7. The quoted radius of curvature (ROC) for the microlenses is 42 μm with a pitch of 30 μm. The ROC measured using the TIE was 41 μm

while the ROC obtained using AFM was 43 µm. The height of the lenses agreed within 100 nm for the two different measurement techniques.

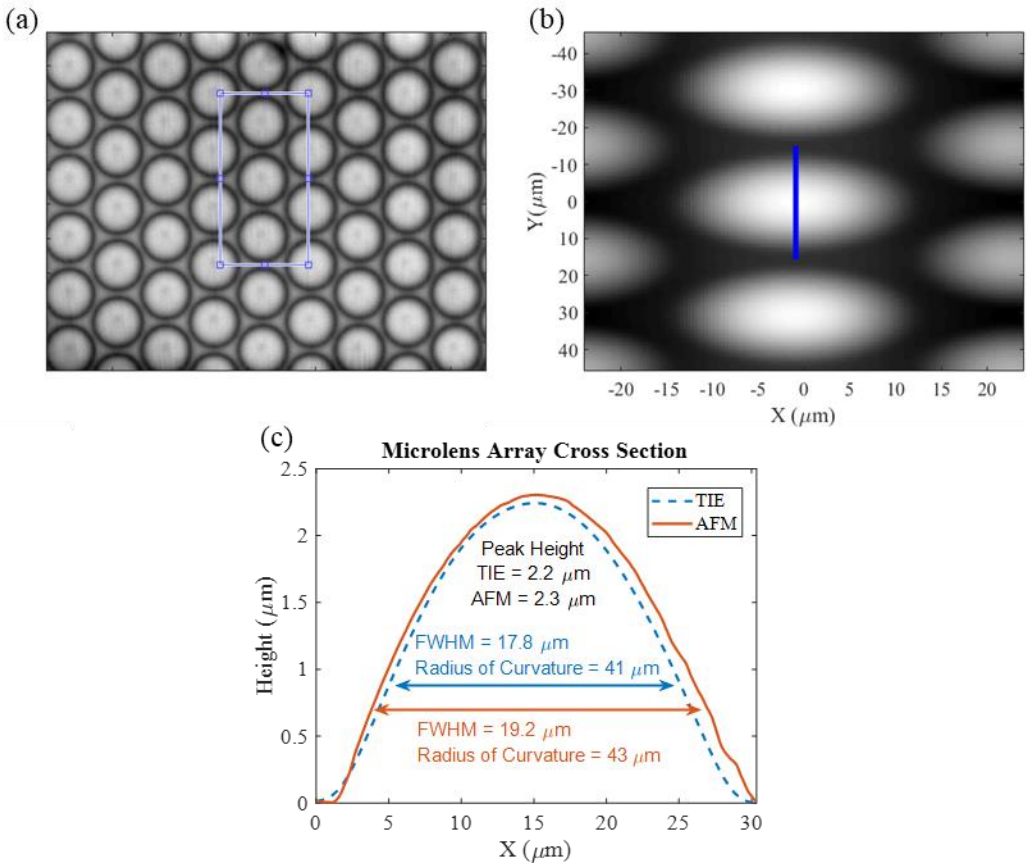

Figure III-7. (a) Brightfield microscope image showing the region of the microlens array used to test the TIE algorithm. (b) Reconstructed thickness profile of the boxed region in (a). The blue line shows the cross-section used in (c). (c) Cross section of a single microlens obtained through the TIE algorithm and atomic force microscopy. The radius of curvature agrees with the manufacturer quoted value of 42 µm.

D. Results and Discussion

1. Single-exposure material response

In order to completely quantify the Δn response of the two-component photopolymer, a series of isolated, Gaussian-shaped photoexposures are applied to the material using the 405 nm wavelength excitation source. Varying the exposure time and writing intensity provides control over the Δn modulation, which is measured using confocal reflection microscopy and the TIE as

discussed above. The concentration of writing monomer within the material is also varied between 10 and 30 wt% to measure the effect of the formulation on the Δn response to exposure. While the method measures the complete index profile, Figure III-8 shows just the index at the peak of each exposure as a function of time, intensity and formulation.

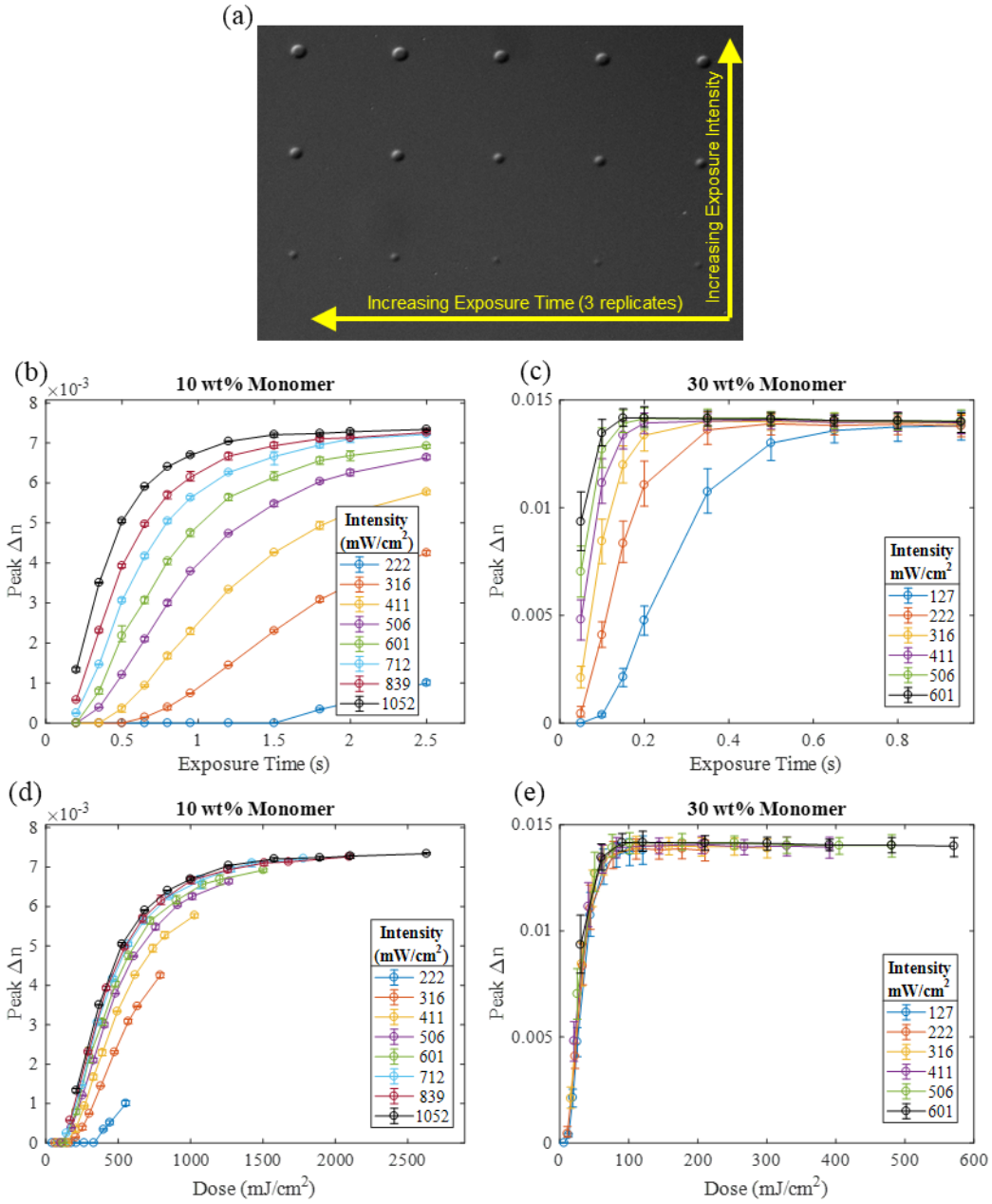

Figure III-8. (a) Differential interference contrast microscopy image of a subset of the measured phase structures. (b-e) The peak Δn response for the model two-component photopolymer over a range of different exposure intensities, exposure times, and monomer loadings as measured by

TIE-based quantitative phase imaging in conjunction with confocal reflection microscopy. (b) The Δn vs. exposure time for 10 wt% monomer loading. (c) The Δn vs. exposure time for 30 wt% monomer loading. (d) The Δn vs. exposure dose for 10 wt% writing monomer. (e) The Δn vs. exposure dose for 30 wt% writing monomer. Each symbol corresponds to 3 isolated exposures, each of which has been measured by the method described in the text. Error bars show the total spread of the three measurements.

The figure illustrates how a very large number of exposure conditions and material formulations can be rapidly evaluated, enabling a complete material characterization. For the model material, the measured data [Figure III-8(b-c)] reveal an inhibition period at low exposure times and intensities, consistent with the initial consumption of oxygen by the radical initiating species [118,119]. After this induction period, the materials respond monotonically with exposure time, exhibiting greater slope for higher intensity and monomer concentration. At large exposure times and intensities, the index response saturates. The saturation Δn of the 10 wt% monomer formulation of 7×10^{-3} is half that of the 30 wt% monomer formulation at 1.4×10^{-2}, indicating the material sensitivity and maximum obtainable Δn are limited by the initial monomer concentration. To support this hypothesis, photoinitiator consumption has been calculated to be negligible over the given exposure times and intensities (Figure III-9). The plot shows that photoinitator is not significantly consumed before saturation of the Δn. Therefore, finite monomer concentration limits the total achievable Δn for a single exposure.

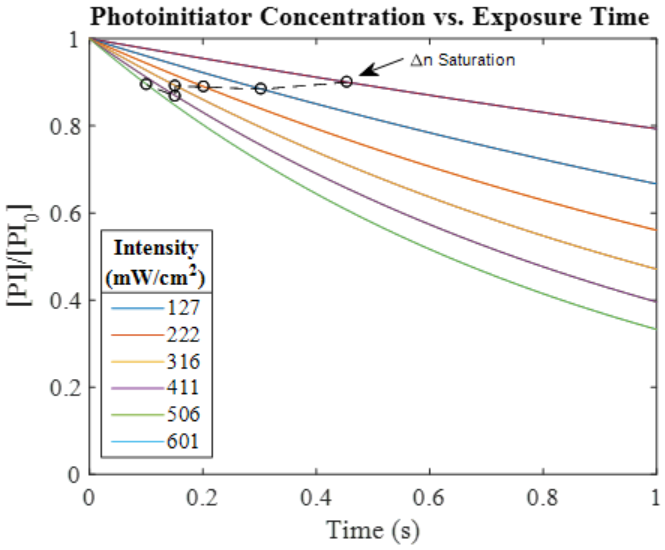

Figure III-9. Plot showing the photoinitator concentration vs. exposure time for different exposure intensities. The time required to reach saturation of Δn is plotted as circles. Saturation is reached well before a significant fraction of photoinitiator is consumed. The molar absorptivity of TPO at 405 nm is 235 L/(mol cm), and the concentration is 3.2 mmol/L.

Finally, the panels in Figure III-8(d-e) show that the raw data can be collapsed to a single master curve for both materials in which index response depends only on the product of intensity and exposure time. One possible explanation for the deviation from this fit at low intensity exposures in the 10 wt% monomer loading is the in-diffusion of new inhibiting oxygen species. However, in the general case, this linear, reciprocal behavior is contrary to the expected behavior of neat acrylate monomers and radical initiators, which should exhibit sublinear (typically square root) intensity dependence due to bimolecular termination. Although some bulk and holographic characterization of such polymers has found reciprocal behavior [85,120], common models based on pseudo steady-state analysis and bimolecular termination assume a sub-linear behavior [121]. Such sub-linear behavior dramatically limits confinement of structures written by a focused beam [122], while conversely, the completely linear behavior shown here drastically simplifies the design of complex 3D index structures.

The linear, integrating response of the material is further demonstrated in Figure III-10, where a series of phase structures was created with the focused 405 nm Gaussian beam for various exposure times. For each structure, the first exposure was immediately followed by three additional exposures of the same duration and intensity. The TIE/confocal reflection measurement was used to measure the resulting Δn profile, shown in Figure III-10(a). As shown in Figure III-10(c), the material responds only to total dose, again falling on a single master curve. The shape of the structure, characterized in Figure III-10(b,d) through the full width at half maximum (FWHM), also depends only on the total exposure dose and is invariant to the total number of exposures. These results demonstrate that the material integrates optical exposure dose with no hysteresis such that a designer can fabricate overlapping phase structures without considering the order in which they are exposed. This behavior is expected to hold as long as subsequent exposures occur before significant diffusion of the writing monomer occurs.

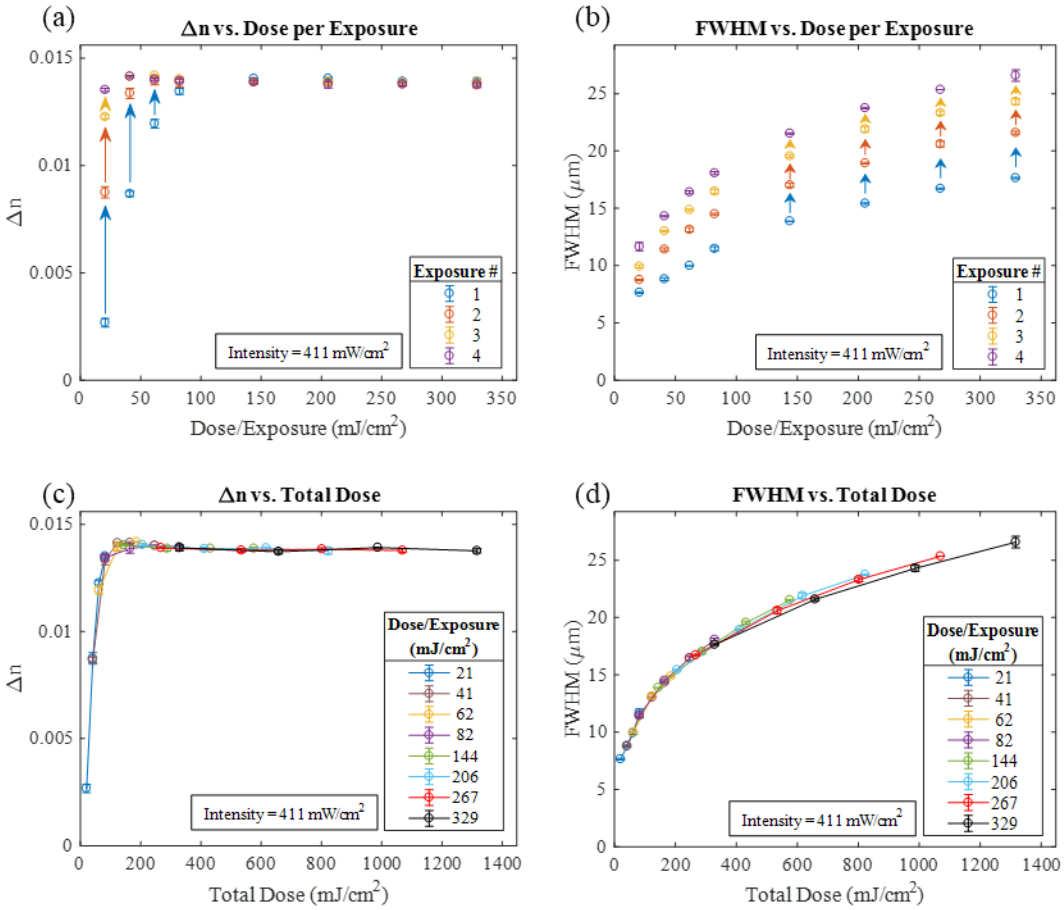

Figure III-10. (a-b) The Δn response and FWHM for a series of phase structures that are exposed up to 4 times immediately after the initial exposure. For low doses below the saturation limit, the Δn continues to increase until the final saturation Δn is reached. Continued growth of the structure terminates due to consumption of all local monomer. (c-d) The Δn response and FWHM for the same structures plotted against the total exposure dose.

2. Predicting phase structure profile with the material response master curve

The previous sections demonstrated TIE phase recovery and confocal reflection microscopy of laser direct-write lithography samples oriented such that the object spatial frequency spectrum was fully within the microscope CTF. This enables quantitative, rapid, and complete characterization of photosensitive material response to intensity, exposure time, material formulation, and multiple exposures. For the model material used here, which is linear and integrating, the peak index response Δn was shown to fall on a single master curve as a function

of total dose. While particularly convenient, multivariable response models could be developed for other materials using the methods presented.

Since the complete spatial frequency spectrum of buried waveguides cannot be accessed by any instrument that is outside the material, I suggest that the appropriate design flow for laser direct-write lithography of 3D phase structures is to first generate the material response model as shown above. Then, the model can be applied to predict the material index response to known exposure conditions that are used to write buried structures whose profile cannot be directly measured. To show that such an approach is valid, here I apply this technique to predict the size and shape of waveguide profiles written in the end-face geometry used above, such that the prediction can be compared to a quantitative measurement.

Here I use the material with 30 wt% monomer loading because of its larger saturation index and single response curve for all exposure conditions. This reference curve, is extracted from the peak index response data in Figure III-8(e), smoothed using a Gaussian filter, and then interpolated using the piecewise cubic hermite interpolating polynomial (PCHIP) method in MATLAB [Figure III-11(a)]. Given an arbitrary exposure profile and peak intensity, the curve predicts the amplitude and shape of the resulting phase element without the need for additional tomographic reconstruction of the individual structure. To demonstrate this, a series of 2D Gaussian exposures was performed in the photopolymer loaded with 30 wt% writing monomer, and the predicted transverse index profiles of the structures were compared to the measured Δn profile using TIE/confocal reflection microscopy [Figure III-11(b-d)]. Both the peak Δn and FWHM predictions agree with the measured values over doses spanning 25 to 570 mJ/cm^2. At small doses, the predicted FWHM deviates, in part due to the low signal-to-noise ratio associated with the TIE for weak phase elements.

The proposed method accurately predicts the complete profile of the waveguide, even far into the saturation regime of the material. Specifically, the relatively sharp transition between the proportional and saturated dose response of the model material enables the formation of nearly binary channel waveguides that would support tightly confined modes, as shown in Figure III-11(b). This in turn would enable the use of beam shaping methods originally suggested for femtosecond lithography of glasses with nearly binary response [123]. Design of such buried, shaped structures in response to shaped foci or multiple-passes is made possible by the characterization method described here.

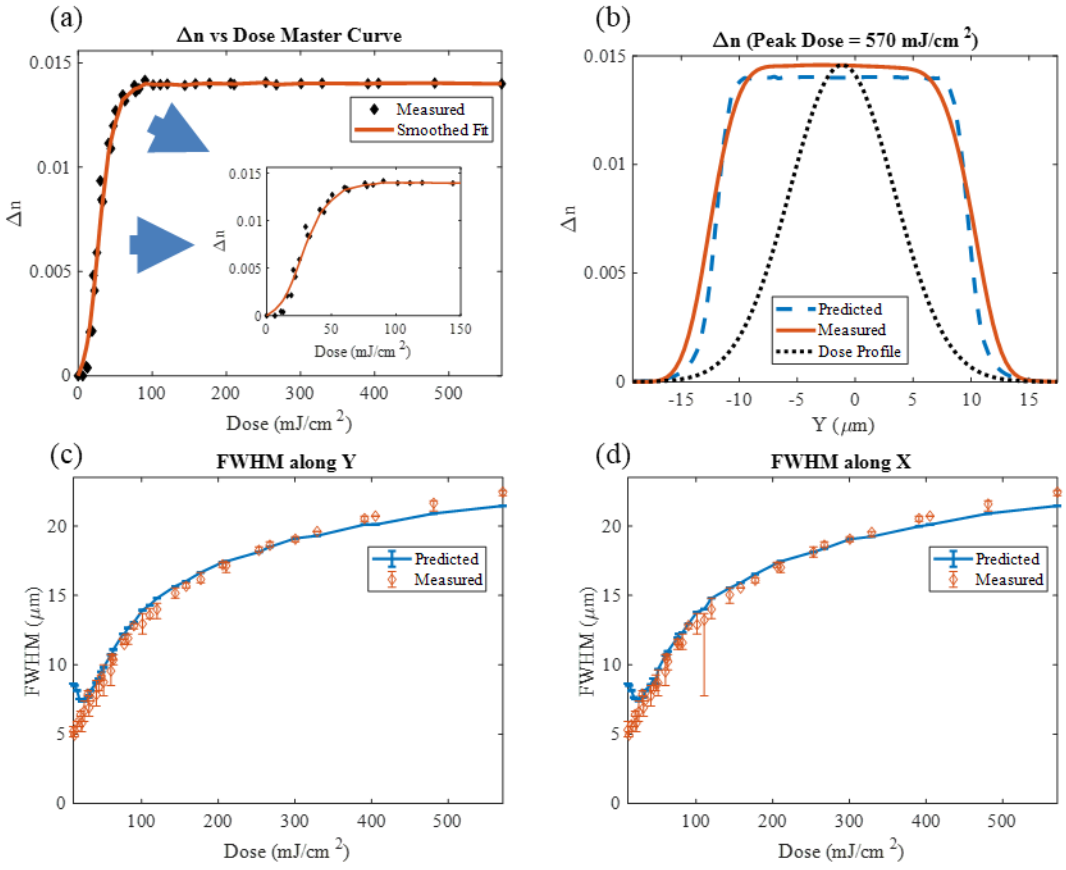

Figure III-11. (a) The phenomenological fit to Δn data acquired at different doses. (b) Cross-sections of the normalized exposure profile, the expected Δn predicted using the curve from (a), and the measured Δn using the TIE/confocal reflection system. (c) The measured vs. the predicted FWHM for a cross section along the y-axis. (d) The measured vs. the predicted FWHM for a cross-section along the x-axis.

E. Conclusion

By ensuring overlap between the CTF of the imaging system and the written phase structure, I have demonstrated the ability to completely characterize the refractive index change resulting from a DLW exposure within a diffusive two-component photopolymer. Using this information about the material response, I was then able to predict both the resulting amplitude and shape of the refractive index perturbation that developed in response to an arbitrary exposure dose profile. This technique overcomes the limitations and experimental difficulty of conventional tomography and enables the ability to design and fabricate known 3D phase structures within a photosensitive material. This technique is applicable for any transparent, photosensitive material that produces a localized change in the refractive index, regardless of diffusion effects, proving useful for both evaluating the phase response, and fabricating isolated waveguide structures in a variety of photosensitive materials.

CHAPTER IV
ENHANCING THE ΔN DYNAMIC RANGE OF TWO-STAGE PHOTOPOLYMERS THROUGH MULTIPLE EXPOSURES[1]

A. Chapter Overview

In the previous chapter, confocal reflection microscopy and quantitative phase imaging (QPI) were applied to study the in-situ response of diffusive two-stage photopolymers to single direct-write exposures. Here, I apply this same metrology to demonstrate a new photostructuring technique that extends the Δn dynamic range of current diffusive two-stage holographic photopolymers without requiring any alteration to the underlying chemical formulation [124]. I then adapt the QPI + confocal reflection metrology to enable the novel measurement of in-situ, dynamic processes such as diffusion within the photopolymer. This metrology enables me to explore and understand the fundamental limits to this new photostructuring technique.

The above photostructuring technique utilizes multiple-exposures to exploit monomer in-diffusion from unexposed regions, yielding structures in the model photopolymer with Δn's up to 4 times larger than those obtained through single exposures. In order to understand the physical constraints behind this technique, I use QPI + confocal reflection microscopy to measure monomer diffusivity during re-equilibration following one and two exposures. Through this extension of the metrology, I show that, similar to the mechanical two-stage photopolymer introduced in chapter II, multifunctional stage-2 monomers increase the local crosslink density of the stage-1 network, thereby impeding re-equilibration of monomer, and subsequently, the ultimate achievable Δn.

---

[1] Adapted with permission from Opt. Lett. 43, 1866-1869 (2018). Copyright (2018) Optical Society of America. (Bibliography reference: [124])

B. Introduction

Direct laser writing (DLW) into photosensitive media is a common technique for fabricating embedded phase structures such as waveguides [6,125] and aperiodic volume optics [4]. Because the achievable refractive index contrast (Δn) within these materials limits features such as the minimum waveguide bend radius, or the diffraction efficiency and overall size of diffractive structures, considerable effort has gone towards the development of such photosensitive materials with increased dynamic range. Two-component photopolymers are a popular material platform for DLW of phase structures due to their high achievable Δn, ease of processing, and wide range of optical and mechanical properties [14,86]. In these materials, Δn is created through a photo-induced concentration gradient between typically high-refractive index photopolymerizable monomeric species and the low-refractive index binder/matrix. However, the primary focus on the development of these materials has been directed towards applications such as holography, data storage, and displays for augmented reality, with characterization of the total dynamic range based on M/# measurements [22] and the formula limit [14]. These metrics specify the total Δn that can be achieved using sinusoidal exposure patterns while under the assumption that only the local monomer concentration can be polymerized. However, in making this assumption, any additional contribution to the Δn from diffusion of external monomer into the exposed region is lost. Although reasonable for large area exposures and materials with low monomer diffusivity, structures such as waveguides, whose diameters are on the order of 10's of microns, can leverage this in-diffusion from the unexposed bulk to achieve considerably higher Δn's through multiple patterning steps.

With the advent of two-photon polymerization and the ability to fabricate micron-scale 3D embedded optical elements through DLW, increased effort has been invested towards characterizing the total achievable Δn and shape of these isolated structures within a photosensitive material [98,126,69]. Additionally, techniques such as quantitative phase imaging have been applied towards measuring the in-

diffusion of monomer into the exposed region [127]. However, all of these studies were limited to investigating the results of single-exposures, neglecting the replenishment of the writing monomer through post-exposure diffusion. Other investigations into the effects of multiple exposures on the resulting refractive index profile either provide only qualitative evidence of increased Δn via phase contrast microscopy [128], or only consider the total accumulated dose, ignoring the effects of in-diffusion of monomer [93]. Thus, the primary methodology for increasing the total dynamic range of two-component photopolymers has been optimization of the material chemistry [17,22,85]. This is typically difficult and/or penalized by other performance metrics such as shrinkage.

In order to extend the dynamic range of two-component photopolymers for the fabrication of isolated, micron-scale phase structures, I quantitatively explore the use of subsequent time-delayed photo-exposures in conjunction with diffusion-assisted monomer replenishment after each exposure. I show that the total dynamic range can be increased by as much as 4 times the single-exposure limit in the demonstration photopolymer. Furthermore, this technique can be used to infer the maximum Δn achievable within a given two-component photopolymer, allowing for rapid screening to determine the most effective combinations of monomer and matrix components. This multi-write technique should be beneficial in extending the utility of already-available two-component photopolymers, allowing for the fabrication of a wider range of waveguide devices and isolated optical structures.

C. Experimental Details

1. Two-component photopolymer formulation

The two-component photopolymer used in the following experiments was prepared according to a previously reported procedure [69]. Briefly, the photo-active chemistry consists of a 1:10 molar ratio of the photoinitiator TPO (2,4,6-trimethylbenzoyl-diphenyl-phosphineoxide) to a synthesized triacrylate writing monomer [phosphorothioyltris(oxybenzene-4,1-diylcarbamoyloxyethane-2,1-diyl)triacrylate]. This

photoactive component was then combined in different weight fractions with the polyurethane matrix, which contained a 1:1 molar ratio of trifunctional polyisocyanate (Desmodur N3900) and difunctional polyol (polycaprolactone-block-polytetrahydrofuran-block-polycaprolactone). The material was cast between a microscope slide and coverslip, with the layer thickness set by 25 µm spacers.

2. Exposure and confocal reflection system

The experimental setup shown in Figure IV-1 was used to expose the photopolymer samples. Two lasers with wavelengths at 405 nm and 660 nm are co-aligned and focused onto the sample, which is mounted on a 5-axis motorized stage. Only the 405 nm laser has sufficient spectral overlap with the photoinitiator absorption spectrum to induce significant polymerization, allowing the 660 nm beam to be used in a confocal reflection modality. During the exposure step, a Nikon objective, operating at an NA of 0.023 provides a focused spot with a 1/exp(2) diameter of 18 µm. Because the material absorbance is 0.04 for 25 µm-thick samples with 30 wt% of the writing monomer, and the Rayleigh range of the focused spot is 10 times larger than the thickness of the sample, the exposure profile is considered uniform throughout the polymer thickness. A Uniblitz VS14 shutter controls the exposure time.

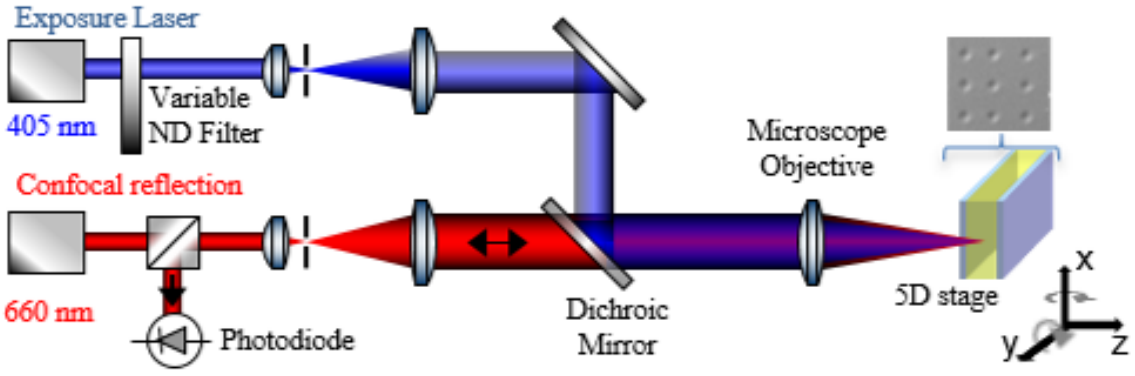

Figure IV-1. The confocal reflection microscope (660 nm path) is used to position and measure the sample thickness, while the co-aligned 405 nm laser is used to expose the photopolymer and create phase structures (inset shows an example differential interference contrast microscopy image). The 660 nm laser is a 100 mW Coherent OBIS LX diode laser, and the 405 nm laser is a Power Technology Incorporated IQu2A105/8983 105 mW laser.

3. Quantitative phase imaging

Measurement of the refractive index profile of the written phase structures is performed using quantitative phase imaging (QPI) based on the transport of intensity equation (TIE), which is further described in the previous chapter [69]. The axial intensity derivative used to solve the TIE was computed using brightfield images defocused by ±3μm about the in-focus image plane [Figure IV-2(a) inset]. In order to calculate Δn from the optical path length measured using TIE, the confocal reflection microscope is used to locally measure the thickness of the polymer layer. In this case, the Nikon objective is swapped with a 0.66 NA Leica objective. A pinhole with a diameter of 1 Airy unit is used to achieve an axial resolution of 3 μm. The confocal reflection signal is fit to measure thickness with an uncertainty of ±2.5%. The unexposed polymer refractive index required to calculate the physical thickness from the confocal reflection signal is measured using a Metricon Model 2010 prism coupler.

D. Results and Discussion

1. Multi-write photostructuring

The multi-write technique was performed as follows: grids of spots were exposed into samples of photopolymer containing 10, 20, and 30 weight percent (wt%) of the writing chemistry. Each spot in the grid extended uniformly through the thickness of the sample and was patterned with 316 mW/cm^2 light at a sufficient dose to consume the local monomer and saturate the photopolymer's Δn response. In this case, the dose per exposure was 253 mJ/cm^2 for the 10 wt% samples, and 111 mJ/cm^2 for the 20 and 30 wt% samples. After each exposure, monomer and photoinitiator were allowed to diffuse from outside the exposed region for 2 hours before re-exposure. Up to 11 consecutive exposures were performed on a given spot under the same exposure conditions. Despite the long diffusion times, heating the polymer can improve monomer mobility and increase diffusivity. Figure IV-2(a) shows the peak Δn of the resulting refractive

index structure as a function of exposure number, while a selection of the corresponding cross-sections is given by Figure IV-2(b). Each data point represents the average of three separate structures.

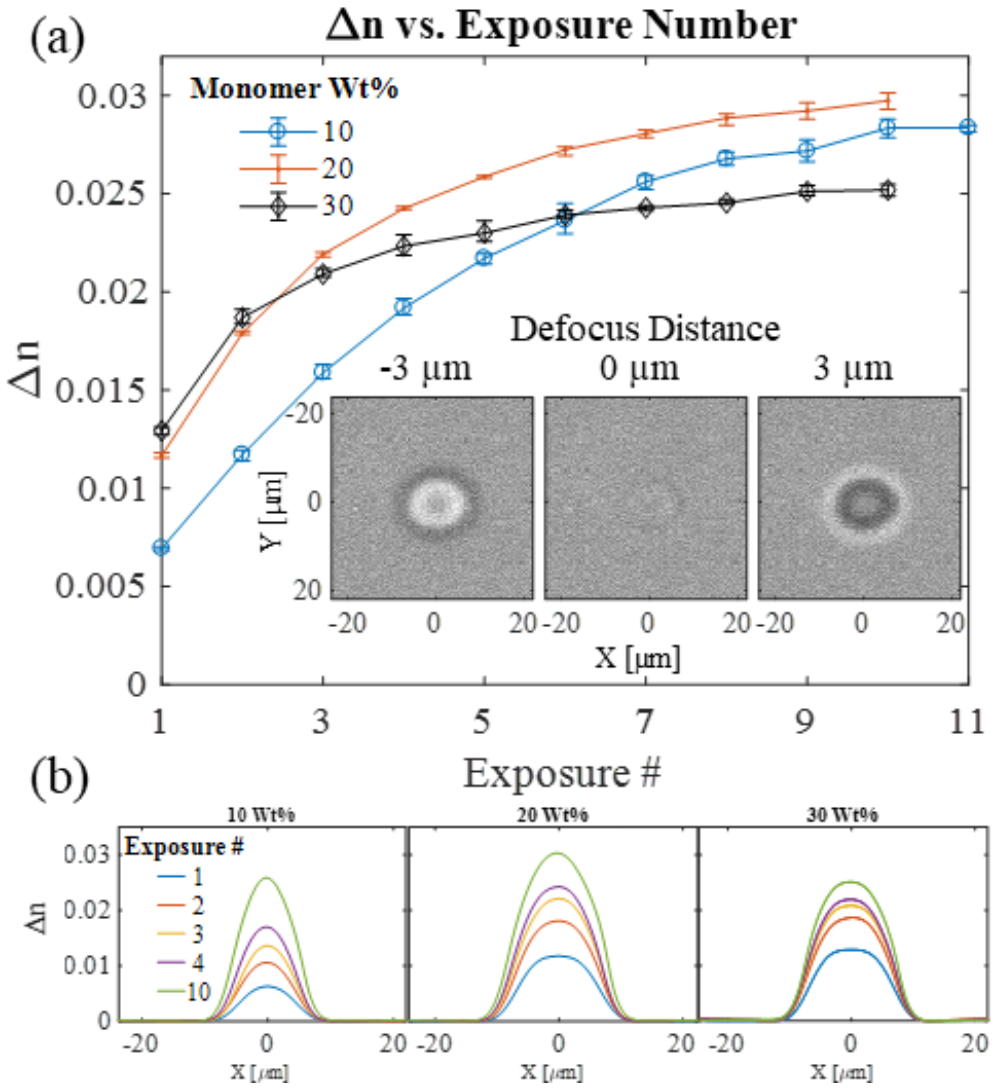

Figure IV-2. (a) The peak Δn as a function of exposure number for the photopolymer with 10, 20, and 30 wt% of the writing chemistry. The dose for each exposure was 253 mJ/cm^2 for the 10 wt% samples, and 111 mJ/cm^2 for the 20 and 30 wt% samples. Exposure intensity was 316 mW/cm^2. Each exposure occured two hours after the previous. The inset shows the defocused brightfield images of one of the exposed structures. (b) The Δn cross-sections at select exposure numbers as measured through QPI.

In the photopolymer formulations, up to a 4× amplification of the measured Δn beyond the single-exposure saturation limit was achieved, with peak Δn's reaching up to ~0.03. Although the single-exposure

saturation Δn increases monotonically with the initial monomer concentration [Figure IV-2(a)], the maximum Δn achieved through the multi-write scheme does not exhibit a clear trend with the initial monomer loading. In general, the gain with subsequent exposures falls more rapidly at the highest monomer loadings, resulting in an overall lower multiple-exposure response.

2. Measuring monomer diffusivity

I consider two hypotheses to explain this trend. Because Δn in holographic photopolymers is primarily due to the transport of species with contrasting refractive indices, the reduced limit on the maximum additional Δn between each new exposure indicates decreasing capability for mass transport. This decrease could be due to reduced mobility, or a solubility limit. To test the first hypothesis, QPI was used to measure the monomer diffusion time into the exposed region. To obtain an estimate for this diffusivity, the photopolymer is initially patterned using a single exposure dose, such that a large fraction of the local monomer is converted into polymer [see the $t = 0$ min profiles in Figure IV-3(a,b)]. Due to the resulting concentration gradient, new monomer diffuses into the exposed region [$t > 0$ min profile in Figure IV-3(a)]. During this diffusion, a delayed, identical exposure converts any replenished monomer to polymer. This new polymer adds to that from the initial $t = 0$ min exposure to generate the corresponding $t > 0$ min profiles in Figure IV-3(b). After this last exposure, monomer is allowed to re-equilibrate before performing QPI. Since concentration is directly proportional to Δn for dilute solutions under the Lorentz-Lorenz model, QPI enables direct measurement of diffusion [21]. Here, Δn obtained for the $t = 0$ min delay acts as the baseline, i.e. no in-diffused monomer between the first and final exposure. The Δn profiles obtained for $t > 0$ min exposure delays are compared to this baseline to determine the concentration of in-diffused monomer. Then, monomer diffusivity is determined by fitting the time-dependent profile to a circularly symmetric 2D Fickian diffusion model. For a photopolymer with initial conditions given by (4.1) , (4.2), and (4.3), where the initial spatial concentration of monomer within the circularly-symmetric

exposure region bounded by $r \leq a$ is given by $C(r < a) = f(r)$ at time $t = 0$, the solution to Fick's law is given by (4.4). The concentration of monomer at the boundary of the exposed region is assumed to remain constant at $C = Co$ and the initial distribution of monomer f (r) is a saturated Gaussian, which is dependent on the exposure beam waist ω_o, the measured Δn, and the saturation level Δn_{sat}. From this solution, the average monomer diffusivity D into the exposed region can be determined.

$$C = C_0, \quad r = a, \quad t \leq 0 \tag{4.1}$$

$$C = f(r), \quad 0 < r < a, \quad t = 0 \tag{4.2}$$

$$f(r) = C_0 \left(1 - \frac{1}{\dfrac{1}{\Delta n \exp\left(-2 \dfrac{r^2}{\omega_0^{\,2}} \right)} + \dfrac{1}{n_{sat}}} \frac{\Delta n + n_{sat}}{\Delta n \, n_{sat}} \right) \tag{4.3}$$

$$\begin{aligned} C = C_0 \left(1 - \frac{2}{a} \sum_{n=1}^{\infty} \frac{1}{a_n} \frac{J_0(r\alpha_n)}{J_1(a\alpha_n)} \exp\left(-D\alpha_n^{\,2} t \right) \right) + \\ \frac{2}{a^2} \sum_{n=1}^{\infty} \exp\left(-D\alpha_n^{\,2} t \right) \frac{J_0(r\alpha_n)}{J_1^{\,2}(a\alpha_n)} \int r \, f(r) \, J_0(r\alpha_n) \, dr \end{aligned} \tag{4.4}$$

where $r\alpha_n$ are the zeros of the Bessel functions of the first and second kind (J_1 and J_2). Here, D is assumed to be uniform across the exposed structure, and the technique provides an effective diffusivity after an arbitrary number of delayed writes. This allows comparisons of monomer diffusion times into the exposed region during each step of the multi-exposure process, providing insight into the change of the local polymer network due to writing monomer polymerization.

In this work, the average diffusivity after a single initial exposure and two initial exposures (separated in time by 2 hours) into a sample with 30 wt% monomer has been measured [Figure IV-3(c)].

After a single pre-exposure, the measured monomer diffusivity is 1.9 $\mu m^2/s$, and does not decrease within the uncertainty of the measurement after the second pre-exposure. Thus, a decreasing monomer solubility in the exposed structure is not responsible for the diminishing ability to achieve additional Δn between multiple exposures. Rather, Figure IV-3(c) reveals that even after equilibration of monomer, the additional Δn achieved after consecutive writes decreases relative to the first exposure. This indicates that the monomer solubility within the exposed region decreases after each successive exposure, and therefore constrains the maximum refractive index obtained from multiple exposures.

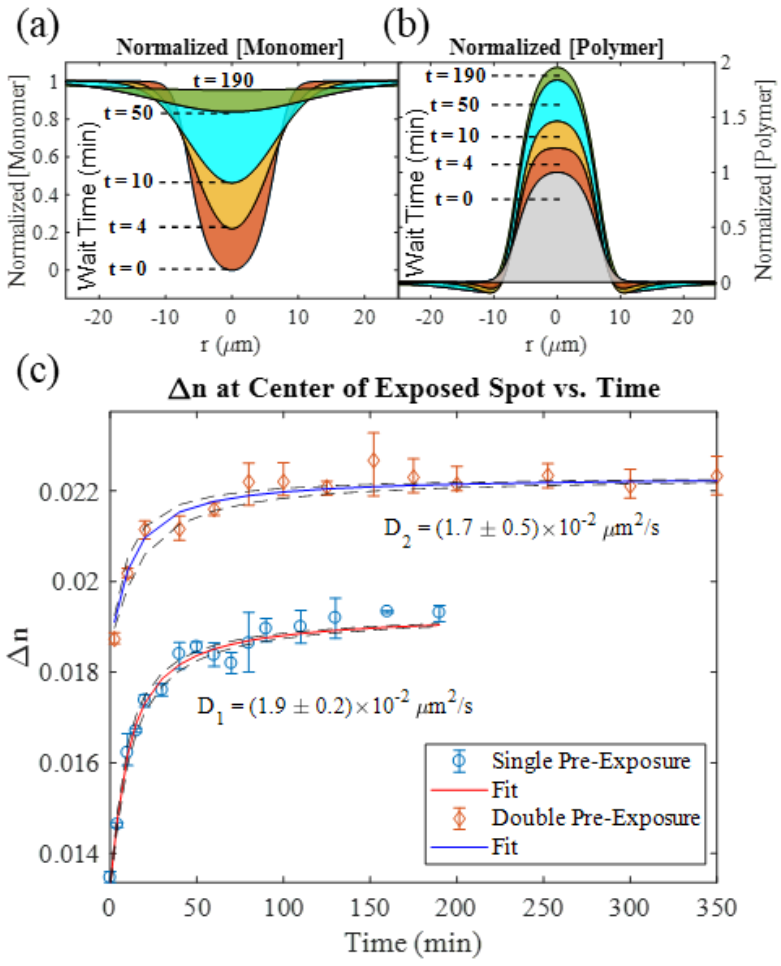

Figure IV-3. (a, b) Theoretical profiles computed using (4.4) and the measured diffusivity that serve to demonstrate the measurement of monomer diffusion time. After the bleaching exposure at time t = 0, monomer is locally depleted and converted to polymer. Replacement monomer then diffuses from the surrounding unexposed region. Performing a second delayed exposure polymerizes and immobilizes the

in-diffused monomer. After re-equilibration of the remaining monomer, this excess of high-refractive index species results in a Δn that can be measured using phase imaging. (c) The resulting fits to extract the monomer diffusivity in a sample with 30 wt% writing chemistry after a single pre-exposure and two pre-exposures. The black dashed lines represent the confidence interval for the diffusivity fit. Error bars were taken for 3 different trials.

3. Limitations to the multi-write process

To further investigate solubility of the monomer as a function of repeat exposures, I plot the data of Figure IV-2(a) as the total refractive index of each spot by adding Δn to the measured background index in Figure. IV-4(a). This background refractive index is measured by preparing unexposed samples of the photopolymer with 0, 10, 20, 30, and 40 wt% of the writing chemistry, and then performing prism coupling at 632.8 nm. Assuming that the exposed structures are sufficiently small and isolated, such that the in-diffusion of monomer during fabrication does not significantly deplete the surrounding monomer concentration, the total refractive index of the exposed spots is determined by adding the measured Δn of the structure to the corresponding refractive index of the background. This shows that increasing the concentration of writing monomer enables a greater single-exposure Δn, but simultaneously constrains the maximum multiple-exposure Δn due to a limit on the maximum absolute refractive index, and thus photopolymer concentration. I attribute this maximum achievable photopolymer concentration, and its dependence on exposure conditions, to the crosslinked interpenetrating network (IPN) formed by the multi-functional acrylate. Further support that the maximum refractive index is locally limited by monomer solubility is given in Figure. IV-4(b), where the peak Δn at each initial monomer loading is plotted against exposure dose and number. This illustrates that the maximum multiple-exposure Δn is reduced as the individual dose is decreased, and thus solubility in the IPN is not simply given by local polymer concentration [12]. This hypothesis accounts for the absence of flat-topped, saturation features in the multi-exposure cross-sections shown in Figure IV-2(b). The non-uniform intensity profile of the Gaussian

exposure beam creates a spatially varying dose, resulting in different kinetics and a non-uniform crosslink density over the multiple exposures.

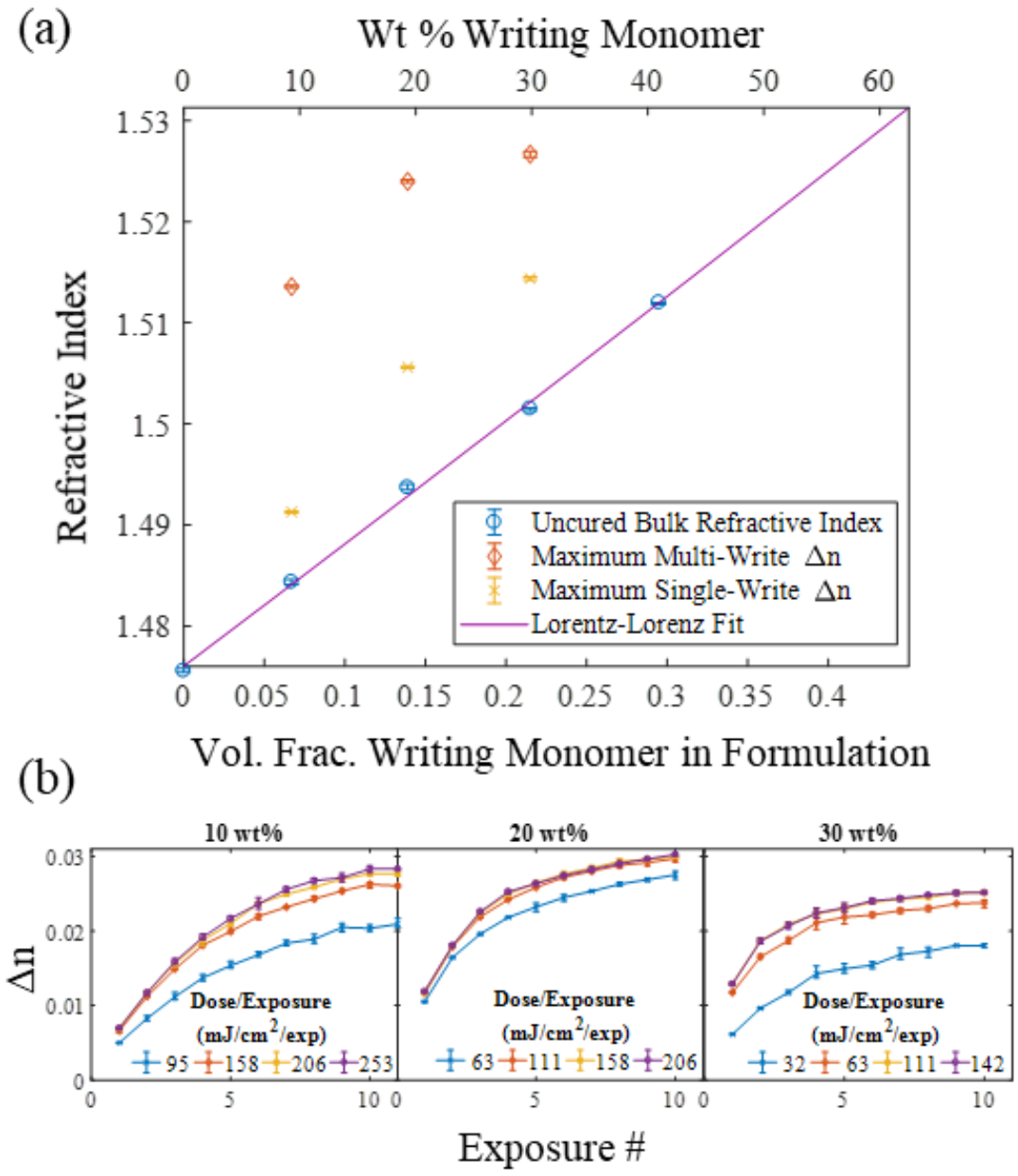

Figure. IV-4. (a) The background refractive index of the photopolymer and its fit to the Lorentz-Lorenz model, added to the measured Δn to show the absolute index of each exposure. Red diamonds show the maximum refractive index from multiple exposures, while the maximum refractive indices obtained after

a single exposure are plotted as yellow x's. (b) The Δn for materials with different initial monomer loadings plotted against exposure number and the dose per exposure. The exposure intensity was 316 mW/cm^2.

E. Conclusion

In conclusion, these results reveal new insight that the total achievable Δn for small, isolated structures depends on an interplay of the single or multiple exposure conditions, and wt% of writing chemistry in the formulation. While it is well known that the potential refractive index change per exposure increases with monomer loading, I find competing effects of increased background refractive index and finite monomer solubility. Within these constraints, I have demonstrated a new multiple-exposure photostructuring technique that provides the ability to achieve a four-fold enhanced refractive index contrast above the single-exposure saturation limit within two-component photopolymers without altering the initial material formulation. Lastly, the measurement technique enables the study of quantities such as monomer diffusivity and solubility as a function of exposure conditions. Understanding the evolution of these limits to material response will aid in the formulation of high Δn photopolymers.

CHAPTER V
HIGH EFFICIENCY FRESNEL LENS IN A TWO-STAGE PHOTOPOLYMER

A. Chapter Overview

In this chapter, I fabricate a large 16 mm-diameter, Fresnel lens diffractive optical element (DOE) in a two-stage photopolymer and demonstrate that micron-scale characterization and control of the photopolymer Δn response is necessary to realize such DOEs with diffraction efficiencies near 100%. High (2.5 μm) resolution, large area, grayscale patterning of the Fresnel lens is performed using projection-lithography and a dithered binary chrome mask. Prior material characterization informs the correct exposure dose and the proper scaling of the grayscale amplitudes in order to compensate for nonlinearity in the photopolymer Δn response. The comprehensive characterization of the material response provided by quantitative phase imaging, coupled with precise grayscale photopatterning, enables the fabrication of high-efficiency DOEs in two-component photopolymers.

B. Introduction

DOEs incorporate complex optical functionality into thin ($\sim 10 - 100$ μm) material layers by using microscopic phase features to diffract light. Such elements facilitate the manufacture of lightweight optics for use in solar energy concentrators [129], custom vision optics [130,131], integrated photonics [132], security [133], and heads-up displays [134]. Although most commercial techniques to fabricate DOEs utilize surface relief patterns to diffract light, such features are exposed and are susceptible to contamination and degradation from dust and scratches. Furthermore, the majority of photolithographic processes and materials used to create these surface reliefs are optimized for high-contrast binary features. These techniques must then approximate analog features using binary multi-level structures that require multiple deposition and etching

steps [135]. While techniques such as diamond turning or grayscale patterning of hybrid sol-gel glasses have been developed to create analog features, the resulting surface relief structures are still susceptible to scratching and contamination [136–138]. Diffusive two-stage photopolymers overcome these difficulties because their internal refractive index can be directly modulated through photopatterning, and the resulting diffractive phase structures are buried within the material [139,140]. With this feature, the overall element can be completely flat and shielded from scratches or dust by laminating protective layers to the surface. Additionally, because the Δn growth in these materials occurs through a self-developing polymerization mechanism, they are amenable to single-step development and bypass the issues and complexity associated with multi-step etching.

Previous research into the fabrication of two-stage photopolymer DOEs has already demonstrated the fabrication of arbitrary phase elements such as Fresnel lenses [139]. However, little work has explored the fabrication of Fresnel lens DOEs with high diffraction efficiency and large (>10 mm) diameters. Realizing such a DOE requires both large-area, high resolution grayscale photopatterning, and knowledge of the micron-scale material response. To overcome the first problem, I use a dithering technique to create large (25 mm diameter), pseudo-grayscale, micron-resolution patterns within a binary chrome mask. Material response data collected by QPI informs the grayscale mask design in order to account for nonlinear scaling in the photopolymer's dose response. Using projection lithography with the grayscale mask, I demonstrate the single-shot creation of 16 mm-diameter lenses with diffraction efficiencies of ~90% in the first order, and prove the necessity of complete knowledge of the material's Δn response in the design and manufacture of custom DOE's.

C. Fresnel Lens Design Theory

The following section reviews the theory behind Fresnel lenses and explores the constraints imposed by the material response and patterning optics on the overall design space. This information will guide the design and fabrication of the grayscale mask and the projection system for performing the optical exposure.

1. Fresnel lenses

Unlike conventional lenses where refraction is the dominant mechanism used to bend incident light rays, a Fresnel lens DOE is composed of an array of microscopic annular rings that bend and focus light through diffraction. The difference between the two elements is shown in Figure V-1, where a monochromatic planar wavefront is incident upon both a refractive asphere [Figure V-1(a)], and the equivalent diffractive Fresnel lens [Figure V-1(b)]. Because the curvature of the asphere varies much less rapidly than the wavelength of the incident light, refraction dominates, and the incident wavefronts are deformed at the lens surfaces according to Snell's law. Conversely, because the Fresnel lens contains features whose sizes are on the order of the wavelength of light, diffraction dominates the wavefront propagation. Because of this, the incident wavefronts are spatially divided by the lens, but re-align with neighboring wavefronts of similar integer 2π phase multiples to form new, converging wavefronts.

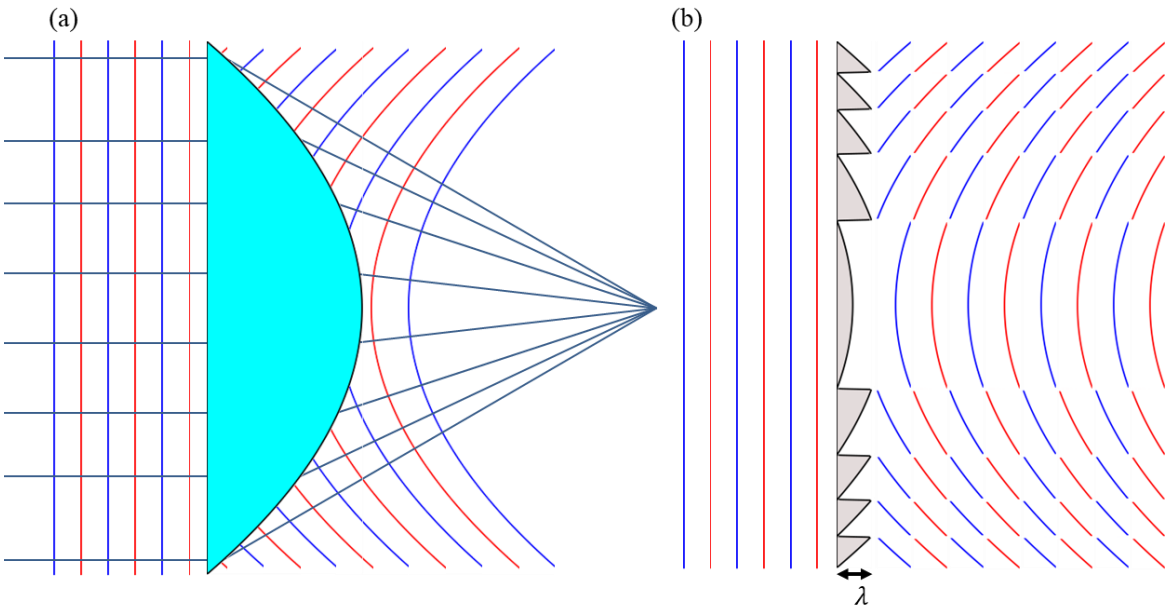

Figure V-1. (a) The refractive lens bends incident wavefronts according to Snell's law. Blue and red lines represent wavefronts whose phases are shifted by 2π radians or λ. Rays drawn normal to the wavefront demonstrate the focusing of light due to the refractive lens. (b) A diffractive (Fresnel) lens contains features that are on the order of the wavelength of the incident light. The incident wavefront undergoes spatial division by these structures, but re-aligns with neighboring wavefronts of similar integer 2π phase multiples to form new, converging wavefronts.

The phase profile of a first-order Fresnel lens is obtained from an equivalent refractive lens [Figure V-2(a)] by removing any material whose optical path length (OPL) contributes a positive integer multiple of a wavelength (λ) [Figure V-2(b)]. The remaining material, whose blazed sections contribute $\leq 1\lambda$ to the OPL of an incident wavefront, form the body of the Fresnel lens [Figure V-2(c)]. The smooth blazed profiles in conjunction with the $\leq 1\lambda$ OPL modulation allow first-order Fresnel lenses to achieve 100% diffraction efficiency into the designed focus point.

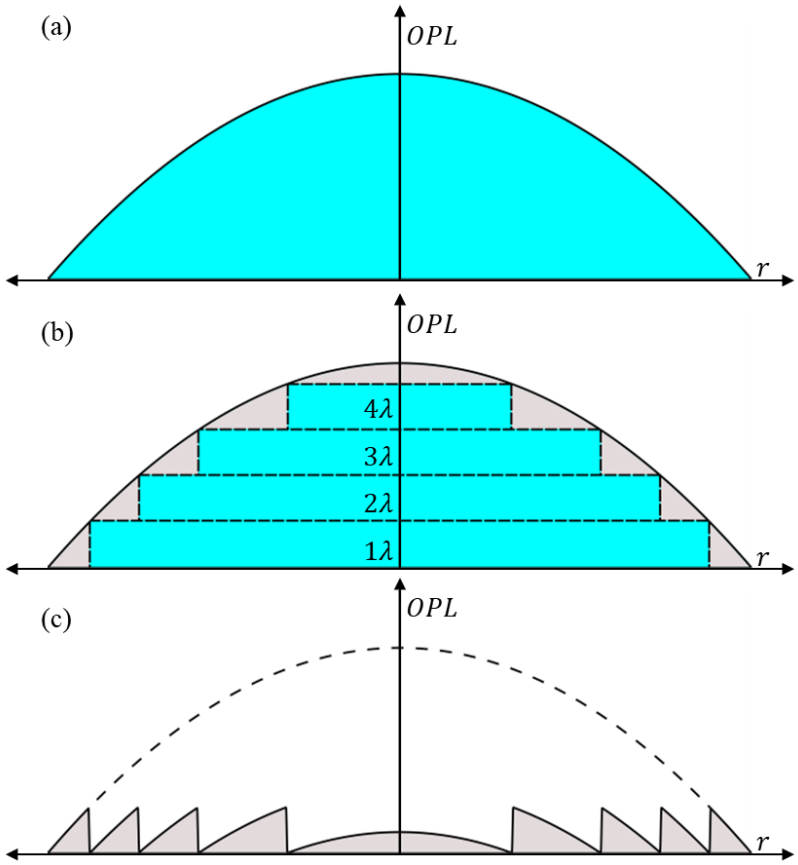

Figure V-2. (a) The desired phase profile of a 'thick' aspherical positive lens. (b) The profile of a Fresnel lens is obtained by removing the unnecessary material that contributes integer multiples of a wavelength to the OPL. (c) The resulting profile achieves similar optical functionality as the original lens, while requiring a fraction of the material.

Following the procedure discussed above, I design a first-order, positive-power Fresnel lens by considering the mathematical description of an equivalent refractive lens. The lens is designed to deform an incident, planar wavefront such that it converges to an arbitrary focus a distance f from the plane of incidence (Figure V-3). The necessary change in the optical path length (ΔOPL) is then given by [equation (5.1)].

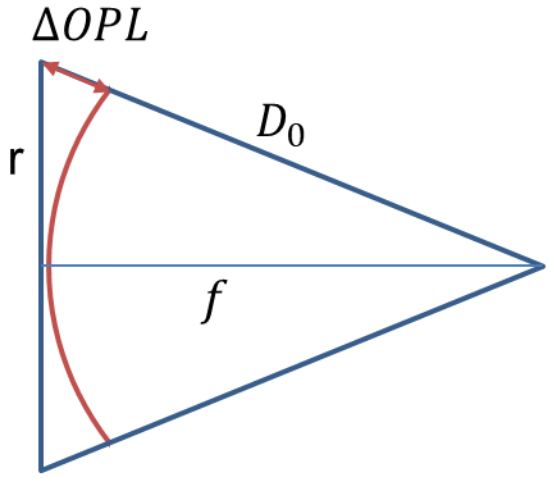

Figure V-3. In order to focus an incident planar wavefront, the DOE or refractive lens must apply a spatially varying OPL that produces the wavefront shown in red.

$$\Delta OPL(r) = D_0 - f = -\left(f - \sqrt{r^2 + f^2}\right) \tag{5.1}$$

Equation (5.1) is then shifted in order to maximize the on-axis ΔOPL and minimize the OPL at the edge of the wavefront[$OPL(r_{max})$]. This shift is expressed by equation (5.2), which is then simplified to equation (5.3).

$$OPL(r) = OPL_{max}(r_{max}) - \Delta OPL(r) = -\left(f - \sqrt{r_{max}^2 + f^2}\right) + \left(f - \sqrt{r^2 + f^2}\right) \tag{5.2}$$

$$OPL(r) = n(r)d = \left(\sqrt{\frac{1}{\Phi^2} + r_{max^2}} - \sqrt{\frac{1}{\Phi^2} + r^2}\right) \tag{5.3}$$

where Φ is the lens power ($\Phi = 1/f$), r_{max} is the maximum radius of the lens, λ is the wavelength of light, $n(r)$ is the spatially varying refractive index, and d is the thickness of the lens. As before, the blazed Fresnel zones are obtained by removing any OPL that contributes an integer multiple of 1λ to the incident wavefront. This operation is performed using the modulo operator as seen in equation (5.4).

$$OPL(r) = \left(\sqrt{\frac{1}{\Phi^2} + r_{\max^2}} - \sqrt{\frac{1}{\Phi^2} + r^2} \right) \bmod \lambda \tag{5.4}$$

The resulting equation contains the mathematical description of the blazed features that allow the first-order Fresnel lens to achieve 100% diffraction efficiency at the designed focus point. It is important to note that deviations of the OPL from this ideal profile from incorrect fabrication conditions will result in the appearance of additional diffractive orders, which manifest as positive and negative focal lengths.

In this paper, the gradient OPL of the Fresnel lens is obtained through modulating the refractive index of the two-component photopolymer instead of the thickness, thereby allowing the physical profile of the lens to remain flat.

2. Required pixel resolution

Before proceeding further, it is necessary to discuss how the practical constraints imposed on the fabrication process by physical optics and the two-stage photopolymer's material response will affect resulting the Fresnel lens. Crucially, the Fresnel profile requires a smooth OPL variation within each blaze in order to achieve 100% diffraction efficiency. However, the mask and optical system used to project the grayscale photopattern have finite resolution. If there are N grayscale levels to pattern across the width of a blazed ring, then the blaze can be approximated by discretized N-level phase structure whose diffraction efficiency η is given by [141]:

$$\eta = \left[\frac{\sin(\pi / N)}{\pi / N} \right]^2 \tag{5.5}$$

In the limit that the projection system resolves each pixel of the original grayscale mask, then there are N levels to approximate each blaze, with a reset of ~ 1 pixel. Therefore, in order to limit

the reset error to no more than 10%, there must be at least 10 pixels per ring. According to equation (5.5), the maximum attainable diffraction efficiency for structures with 10 pixels is 97%. However, from Figure V-2(c), the width of the blazed rings in the Fresnel lens vary with radial position. Therefore, it is also necessary to determine the minimum pixel resolution necessary to maintain a density of 10 pixels in the outermost ring. The width $\Lambda(r)$ of the p^{th} ring for a positive lens is given by equation (5.6):

$$\Lambda(r) = f\lambda / r_p \tag{5.6}$$

and

$$r_p^2 = 2fp\lambda\,, \tag{5.7}$$

where f is the lens focal length, λ is the wavelength of light, and r_p is the radial location of the p^{th} ring [142]. As seen by equation (5.6), the width of each blaze is therefore inversely proportional to the radial distance from the center of the lens. Increasing either the power or diameter of the lens also increases the number of blazes, and the required patterning resolution.

Given the requirement of $< 10\%$ error in the patterned blaze, the maximum diffraction efficiency was calculated to be 97%. While this is sufficient for ideal systems that assume perfect mapping of the grayscale image to Δn within the photopolymer, future work will incorporate the response function of both the projection system and the material Δn response in determining the actual patterned structure. Then diffraction efficiency can be calculated by simulating the real profile of the developed Fresnel lens.

3. Design space

The above section provided the required pixel density to contain the discretization error of the grayscale ramp to $\leq 10\%$. I now use this constraint to explore the range of Fresnel lens

widths and powers that can be obtained. I also investigate their relationship to fabrication constraints such as the patterning resolution, depth of focus of the exposure system, thickness of the photopolymer, and Δn of the photopolymer. The lenses are designed to operate at a wavelength of 532 nm, which is both near the maximum sensitivity of the photopic human eye, and readily available using diode-pumped solid-state lasers.

Here, I first analyze the optical patterning constraints, as they will then establish the required Δn and thickness of the photopolymer. Figure V-4(a) demonstrates the minimum necessary pixel diameter that must be written by the exposure system into the photopolymer in order to maintain at least 10 pixels or phase steps in the outer ring of the Fresnel lens, and is calculated using equation (5.6). Each contour represents the Fresnel lens power and radius that can be achieved using the given pixel resolution, and assuming sufficient OPL to obtain 1λ of delay. As either the lens power or radius increases, the outer blazed rings become thinner and require a greater resolution in order to maintain the 10-pixel density. Given this constraint on resolution, Figure V-4(b) then lists the depth of focus of the exposure system ($2z_{DOF}$), assuming an incident Gaussian beam, and the relationship: $2z_{DOF} = 2\pi\omega_0^2/\lambda$, where ω_0 is the pixel radius [143]. Importantly, these two parameters (ω_0 and z_{DOF}) also serve to constrain the set of allowed photopolymers. In order to support the desired resolution, the material thickness must be $\leq 2z_{DOF}$ while still achieving an OPL of at least 1λ. This leads to the plot shown in Figure V-4(c), where, given the required material thickness (established by $2z_{DOF}$) and pixel size, the necessary Δn range that the material must support to achieve 1λ of OPL is shown.

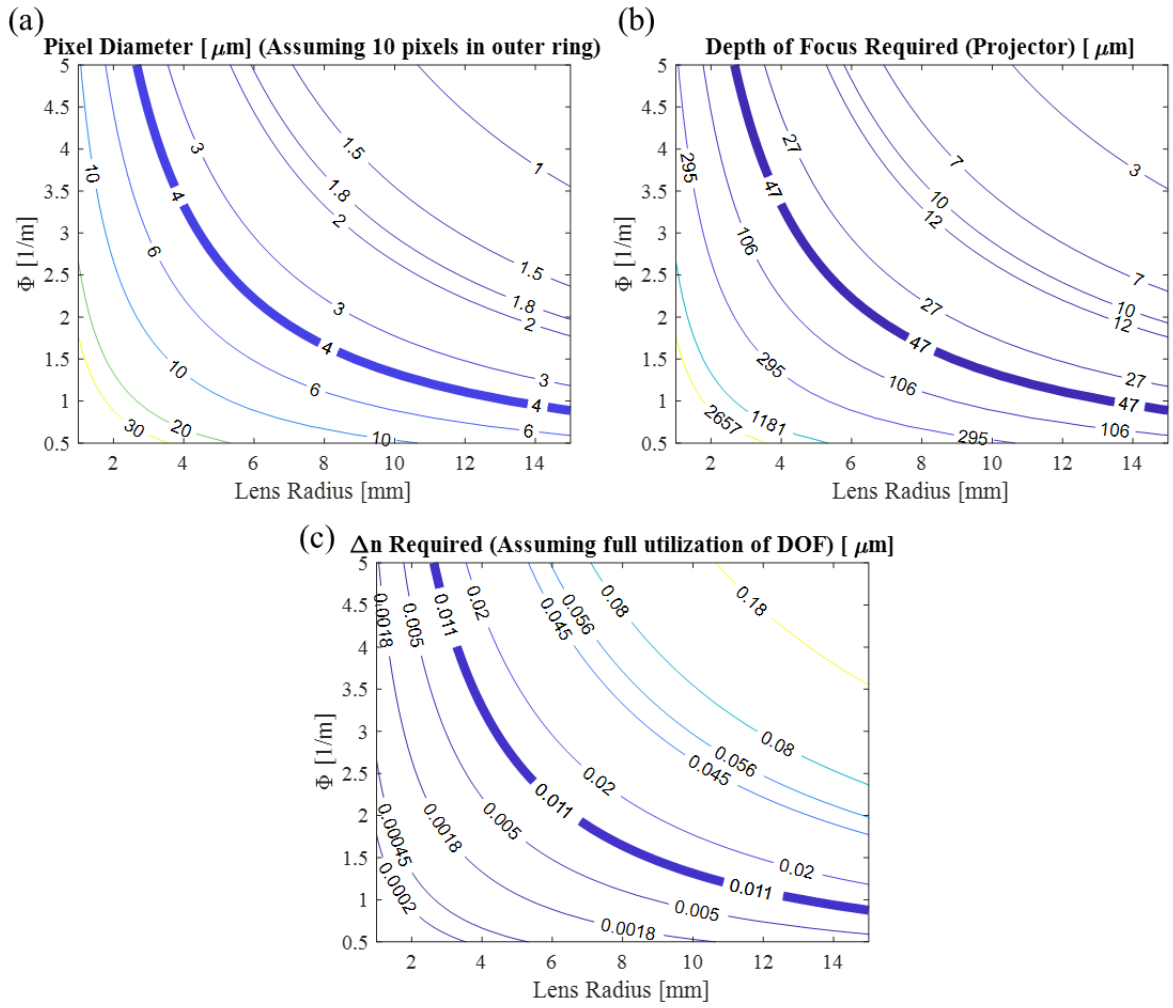

Figure V-4. Contour maps of the Fresnel lens design space that specify the required resolution, thickness or depth of focus, and Δn in order to manufacture a Fresnel lens of a given optical power and radius. (a) The maximum resolution required for both the patterning system and material response in order to have at least 10 pixels in the outermost ring. (b) The maximum thickness of the polymer, and depth of focus of the patterning system, as dictated by the pixel resolution from (a). (c) The necessary Δn, to provide one wave of delay within the thickness given by (b).

D. Experimental Details

1. Constraining the design space through prior characterization

Here, the importance of the prior characterization of the two-stage photopolymer Δn response is demonstrated, as it can now be used in conjunction with Figure V-4 to establish both the range of lenses than can be fabricated, and the requirements on the exposure system's

resolution and depth of focus. The 30 wt% photopolymer characterized in chapter III is selected because it supports the largest single-exposure Δn range of the tested materials. The measured Δn vs dose response is shown in Figure V-5.

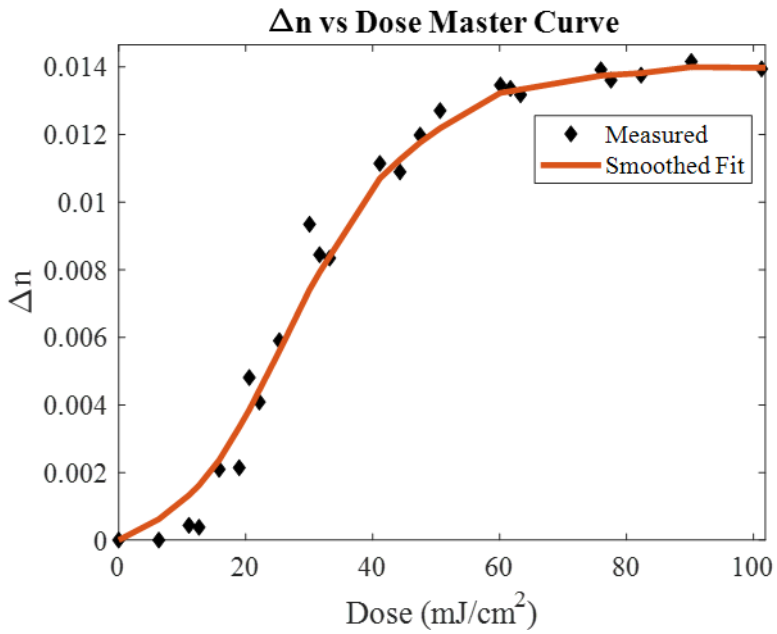

Figure V-5. Δn vs dose response curve for the 30 wt% two-stage photopolymer (presented in chapter III).

From Figure V-5, the maximum Δn that the photopolymer can support is ~0.014. With this constraint, the curves in Figure V-4 show the range of lenses that can be produced, along with the required resolution and depth of focus in the patterning system. The data provided by the Δn characterization can be further exploited to simplify the optical exposure conditions. By restricting the Δn range of the two-stage photopolymer to 0.011, the nonlinear dose response caused by Δn saturation is avoided, and the material operates within the linear range of the Δn vs dose response. With this restriction on Δn, the lenses that can now be fabricated are shown to the left of the 0.011 contour in Figure V-4(c), assuming a minimum patterning resolution of 4 μm. Lastly, the characterization data also reveals the need for an initial uniform pre-exposure in order

to react dissolved oxygen species and eliminate the initial nonlinear threshold at the low end of the dose range. In this chapter, I will demonstrate the fabrication of a 16 mm, 1 diopter lens.

2. Design of the grayscale mask

Here I describe the design of the mask for performing high-resolution, large area, grayscale photopatterning. Digital micromirror devices (DMDs) and spatial light modulators provide both the grayscale capability and the ability for dynamic mask generation. However, these devices are limited in both pixel size ($\sim$10 μm) and number, with average values of $\sim 1920 \times 1080$ pixels. Although demagnification optics can improve the patterned resolution, the limited number of pixels constrain the size of the patterned field. Techniques have been developed to overcome this limitation by stitching multiple exposures into a larger pattern [144]. However, for patterning a Fresnel lens, this requires translation stages accurate to within ~1/10th of a pixel, or $\sim$1 μm over 16 mm of travel and assumes that the nonlocal material response due to diffusion will not affect neighboring patterns. A cheaper alternative involves the use of silver-halide film transparencies, which can support grayscale patterns with resolutions up to 40k dots per inch (dpi). Unfortunately, the silver halide film has a nonlinear dose response curve and is sensitive to errors in the applied dose during the mask writing process. The risk of these errors in the final mask are undesirable when fabricating Fresnel lenses that require accurate grayscale patterning. Because chrome masks use a binary development process, they are immune to such errors, and are able to support resolutions down to $\sim$1 μm over 4 × 4" areas. To obtain grayscale features in such a binary device, I employ a dithering scheme where transparent and occluded pixels are juxtaposed in different ratios as shown in Figure V-6. By applying a small defocus to the optical projector, the individual pixel resolution can then be blurred, resulting in a smooth grayscale pattern.

The chrome mask is fabricated by Digidat Inc with pixel sizes of 2.5 μm over a 1 × 1" area. Dramatic simplification in the mask design is achieved by exploiting the two-stage photopolymer reciprocity between exposure time and intensity. This property was determined in chapter III, and is unexpected given typical radical initiation kinetics. However, without this behavior, the mask transmittance function would have to be designed for a specific exposure time and illumination intensity. Conversely, due to reciprocity, the material requires only that the transmittance be proportional to the desired Δn. Using this information, the desired Fresnel lens profile is computed using equation (5.4) and normalized by λ. The computed phase profile is then dithered using the Matlab function “dither”, and its binary profile is shown in (Figure V-6) at various magnifications.

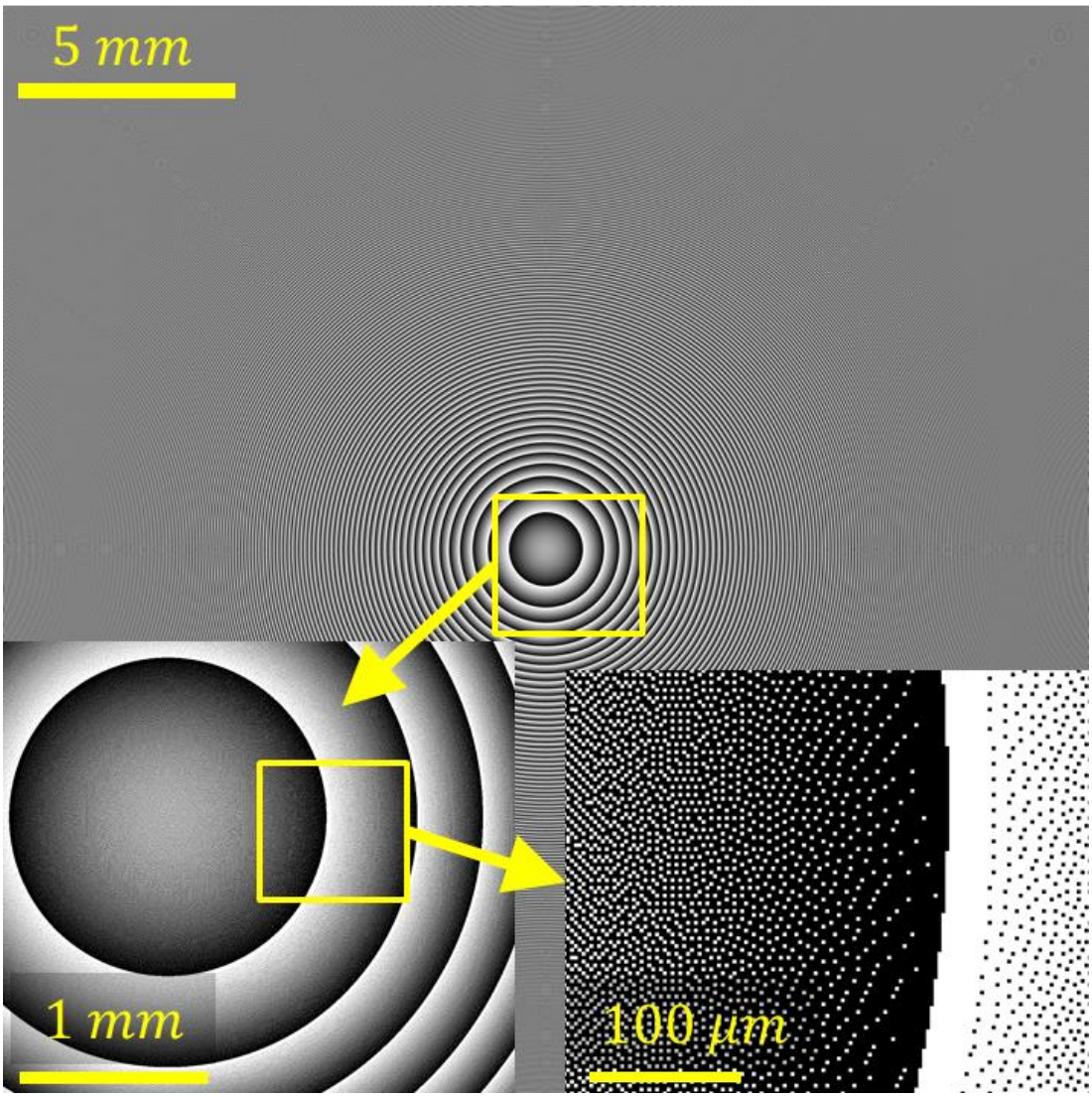

Figure V-6. The dithered bitmap used to create the pseudo-grayscale chrome mask. Pixel resolution is 2.5 μm. Each of the three regions shows an increasingly magnified view of the mask.

3. Optical exposure system

An optical projector was constructed to perform non-contact imaging of the mask onto the material and is shown in Figure V-7. The illumination optics consist of a 405 nm LED (Thorlabs M405L2) configured for Köhler illumination at the plane of the mask. To achieve this illumination condition, the collector lens reimages the LED source onto the aperture stop/entrance pupil of the condenser lens, which is located one focal length from the condenser.

Because the source LED and condenser pupil are at conjugate planes, the LED is defocused at the plane of the mask, and spatial variations in illumination intensity arising from the physical shape of the LED are greatly reduced. Using this technique, the illumination at the mask is uniform over a circle of at least 25 mm diameter. Additionally, by adjusting the diameter of the condenser aperture stop, the numerical aperture (NA) of the illumination optics can be adjusted to match the NA of the later 1x mask projection optics. Independent control over the field of illumination is realized by positioning the field stop a distance of 2f from the condenser such that it is reimaged onto the mask. Thus, independent control over both the field and the NA of the illumination optics is provided.

The 1x imaging system to project the grayscale mask into the sample uses two Nikon Nikkor 58 mm f/1.2 lenses in a 4f configuration to create the 1x relay. An iris placed one focal length between the two lenses controls the resolution and depth of focus of the projector. This is adjusted to match the NA of the projector with that of the illumination optics in order to achieve the highest contrast and realize the appropriate patterning resolution and depth of focus.

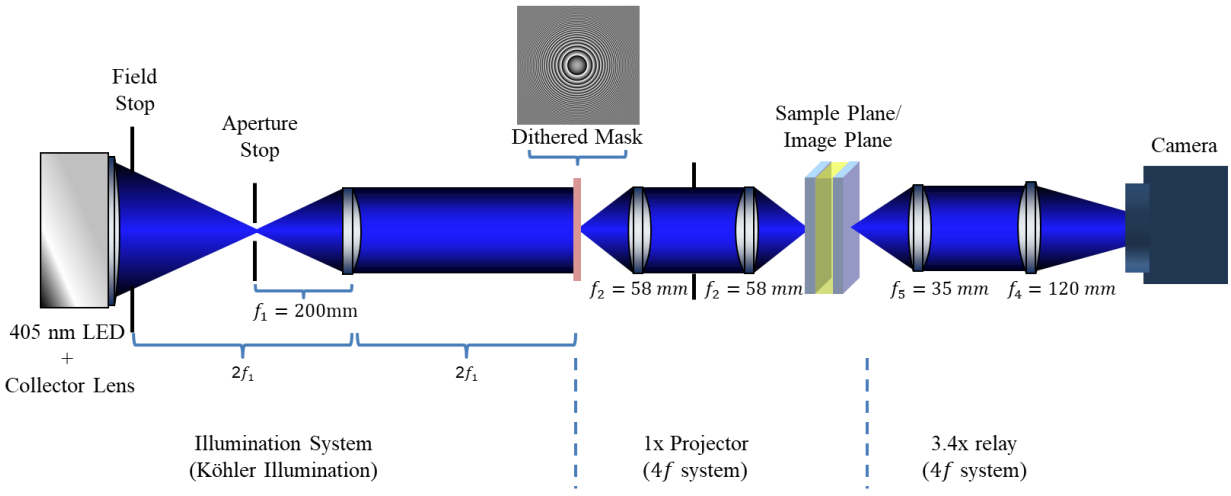

Figure V-7. A schematic of the projector used to pattern the two-stage photopolymers. The system consists of three primary components: 1) the illumination system, 2) a 1x projector, and 3) a 3.4x

imaging relay for alignment of the mask and sample. The illumination arm is configured for Köhler illumination in order to provide a uniform beam to illuminate the mask, while simultaneously offering independent control over its field and NA. The camera in the final imaging path is a Thorlabs DCC1545M CMOS camera.

The secondary 3.4x relay enables alignment of the mask and sample planes. This imaging system is first aligned to the illumination system by translating the camera and lenses along the optical axis until the field stop and detector plane are conjugate. A blank sample filled with immersion oil and spacers of the appropriate thickness is then positioned at the sample plane and brought into focus at the detector. While the sample is still mounted, the mask is brought into focus at the camera. Some small defocus can be applied to the mask at this point in order to appropriately blur the dithered pixels. With each of the planes now conjugate, the blank is removed and the real photopolymer sample is mounted. Back-reflections off the back surface of the sample are minimized by attaching an ND filter with index-matching oil (Cargille immersion oil Type A). The optical precure to consume dissolved oxygen is performed by removing the mask using a kinematic base. Exposure time is controlled through TTL modulation of the LED current using a MyDaq and the included arbitrary waveform generation software. After exposure, the sample is cleaned of oil and placed in an oven at 60°C. The heat increases monomer diffusivity and shortens the time to re-equilibrate the monomer.

4. Two-stage photopolymer formulation

The photopolymer used to make the Fresnel lenses is the same as that used in the previous two chapters. Briefly, the photo-active chemistry consists of a 1:10 molar ratio of the photoinitiator TPO (2,4,6-trimethylbenzoyl-diphenyl-phosphineoxide) to a synthesized triacrylate writing monomer [phosphorothioyltris(oxybenzene-4,1-diylcarbamoyloxyethane-2,1-diyl)triacrylate]. This photoactive component was then combined in a 3:10 weight fraction with

the polyurethane matrix, which contained a 1:1 molar ratio of trifunctional polyisocyanate (Desmodur N3900) and difunctional polyol (polycaprolactone-block-polytetrahydrofuran-block-polycaprolactone). After degassing under vacuum for 10 to 20 minutes, the material was cast between two 3x4" microscope slides, with the nominal layer thickness set by 50.8 μm spacers. Samples were cured in a 60°C oven overnight.

5. Measuring the diffraction efficiency

Diffraction efficiency of the fabricated Fresnel lenses was measured with a 532 nm source using the optical setup shown in Figure V-8. The combined spatial filter and beam expander produce a 50 mm-diameter Gaussian beam, which is truncated by irises in order to match the aperture of the Fresnel lens. A power meter with attached iris is translated along the optical axis in order to selectively capture the focused light in each of the diffracted orders while blocking any stray, undiffracted light. The total transmitted power through the Fresnel lens is measured by inserting a positive lens immediately after the Fresnel lens in order to focus all light onto the power meter. Fresnel reflections off the surfaces of the collecting lens are computed and added to the total power (~8%). The diffraction efficiency of each order is then computed by dividing the power in the given order by the total power transmitted through the Fresnel lens, after accounting for reflection off the collecting lens.

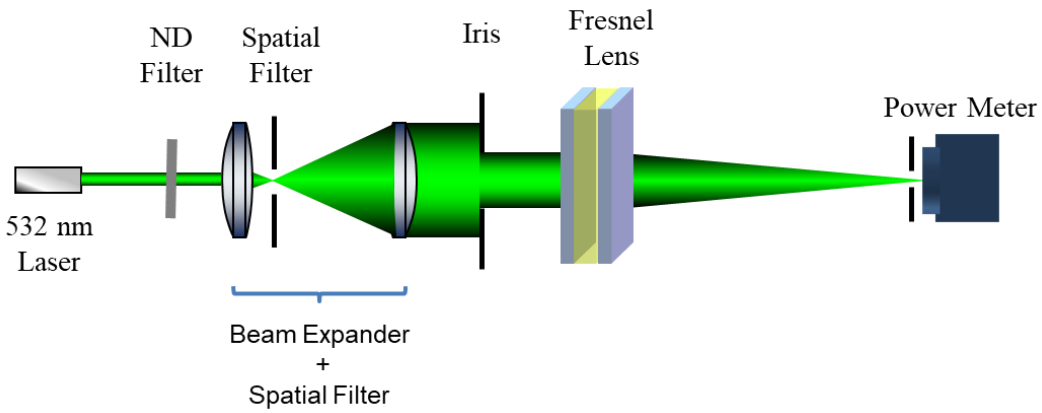

Figure V-8. The optical system used to test the efficiency of the Fresnel lenses. A 532 nm diode-pumped solid-state laser is attenuated with a neutral density filter, spatially filtered, and then magnified in order to produce a ~2" diameter collimated beam. An iris placed immediately before the Fresnel lens matches the beam width to the aperture of the Fresnel lens.

E. Results and Discussion

1. Fabrication and evaluation of a 1 diopter Fresnel lens

Here I demonstrate the fabrication of a one-diopter Fresnel lens with a minimum width of 16 mm in a photopolymer sample whose nominal thickness is 50.8 μm (as set by the plastic spacers). First, a new Δn vs dose response curve is acquired in order to account for the larger spectral bandwidth of the projection system LED compared to the diode used for the previous characterization in chapters III and IV. The same sample geometry and measurement procedure as reported in chapter III is used to measure the Δn of 15 μm spots written into the photopolymer with the mask projector. The results are plotted in Figure V-9 and are compared with the previous characterization data. Both data sets show the presence of an oxygen threshold, a region of linear Δn growth vs dose, and an upper saturation limit. Additionally, the total Δn range remains the same. The only difference is a slight shift of the Δn curve towards higher doses due to the lower spectral overlap of the 405 nm LED with the photoinitiator's absorbance spectrum.

In light of this data, an initial precure dose of 18 mJ/cm^2 is used to consume any dissolved oxygen.

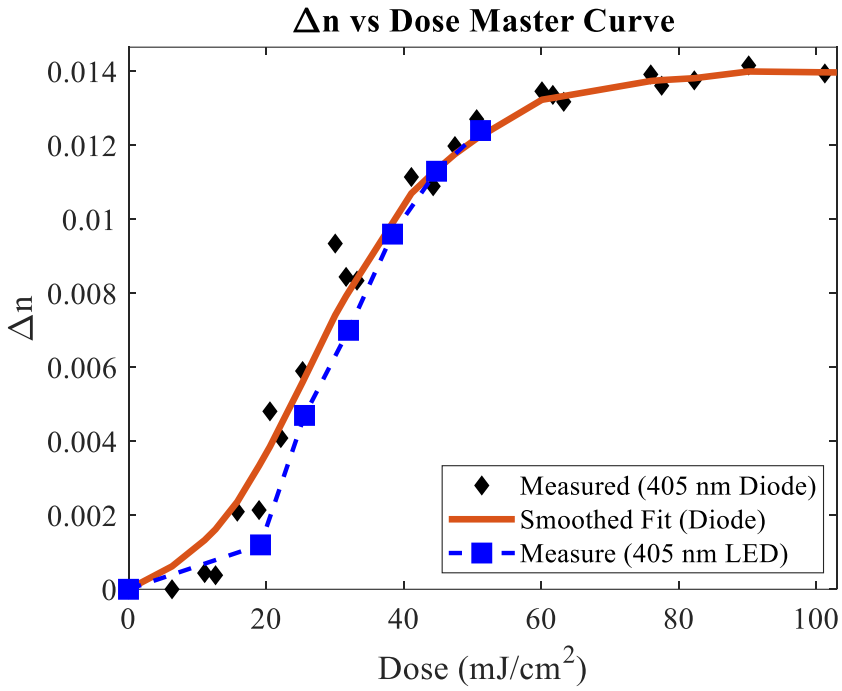

Figure V-9. Δn vs dose response curve for the two-stage photopolymer (presented in chapter III). The blue squares show the Δn vs dose using the LED source in the mask exposure system.

After the oxygen precure, the calibration data in Figure V-9 specifies that an additional exposure dose of ~20 mJ/cm^2 should be applied in the photopattern to achieve the nominal $\Delta n = 0.0104$ for a 50.8 µm-thick sample. However, due to thickness variations resulting from polymer wedging between the spacers and the microscope slides, the optimal dose of 16 mJ/cm^2 was found to produce lenses with the highest diffraction efficiency. This dose for the 1 diopter lens was applied immediately after the precure using an exposure time of 0.86s with an intensity of 18.5 mW/cm^2.

Following the exposure, the lens was removed from the projector, cleaned of immersion oil, and placed in the oven at 60℃ for 24 hours. A picture of the Fresnel lens was taken using a

Nikon D800 camera equipped with a Nikkor 105 mm f/4 lens, and is shown in Figure V-10(a). The boundaries of the annular rings are clearly visible from light scattering. The imaging ability of the Fresnel lens was also evaluated by magnifying a grid of 0.25” squares [Figure V-10(b)]. The lens was used as a magnifier by placing the grid well within the focal length ($f = 1000$ mm). The primary order is visible, while higher, or undiffracted orders resulting from an imperfect phase profile are not noticeable. The blurry regions in the image are attributed to imperfections and scatter within the material, resulting from the surface contamination on the lens during the time of exposure.

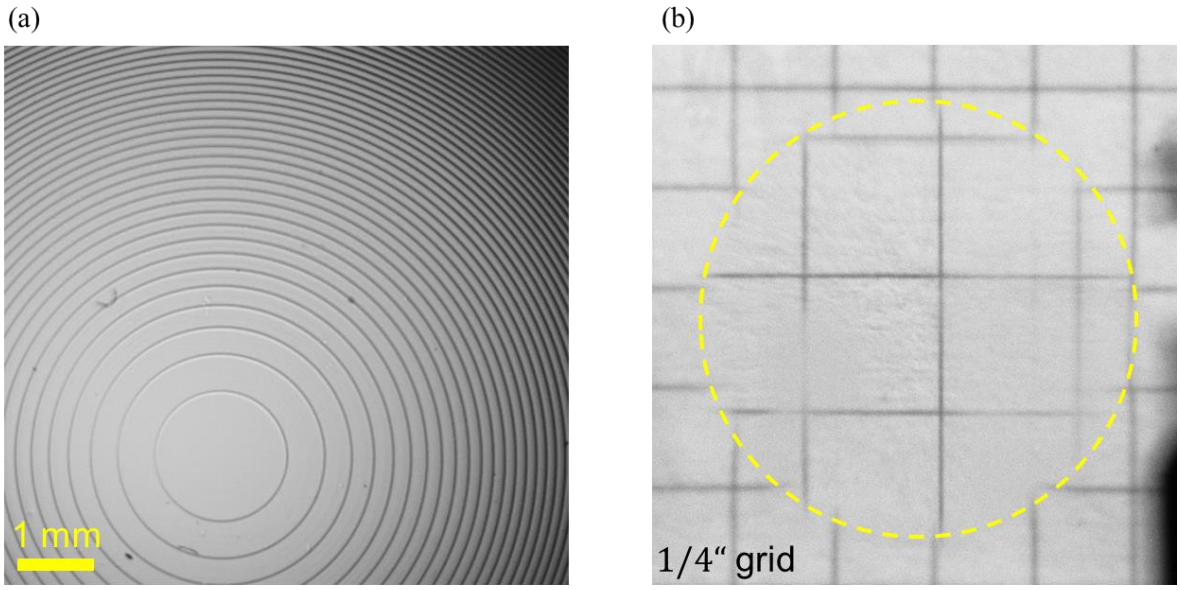

Figure V-10. (a) Camera image of the Fresnel lens. (b) Magnified image of a 1/4" square grid produced with the 1 diopter lens. The majority of light is coupled into the primary diffraction order.

To provide a quantitative evaluation of the performance, the diffraction efficiency of the lens was measured using the method described in the previous section. The efficiency of each order remained constant one day after exposure, indicating that monomer had re-equilibrated. The highest diffraction efficiency was found to be 93% in the first order, which is close to the

designed efficiency of 97%, and proves accurate photopatterning of the desired phase structure. Table V-1 shows the measured diffraction efficiencies in each of the positive orders.

Table V-1. Diffraction efficiency in each of the orders of the Fresnel lens.

Order #	1	2	3
Focal Length (mm)	1000	500	250
Measured Power (mW) (Total = 20.7 mW)	19.2 ± 0.4	1.2 ± 0.4	0.1
Diffraction Efficiency (%)	93	6	0.5

2. Sources of error preventing the optimal diffraction efficiency

To both highlight the necessity for precise materials characterization during the fabrication of Fresnel lenses, and to determine the potential sources of error in the fabrication process, I now simulate the effect of processing parameters on the diffraction efficiency in each of the diffracted orders. Each blaze is approximated as a linear ramp, which is valid for rings far from the center, where $\Lambda(r)$ is small compared to the rate of change of the OPL. Then, the general phase profile describing the lens can be given by a normalized sawtooth function as shown in Figure V-11. The efficiency, assuming normal plane wave incidence, is determined through the following equation:

$$\eta_n = F\left[e^{-i2\pi OPL(r)}\right] \tag{5.8}$$

where η_n is the n^{th} order diffraction efficiency, F represents the spatial 1D Fourier transform integral, and $\mathrm{OPL}(r)$ is the normalized optical path length of the lens. Because the spatial grid is normalized, the n efficiency orders are similarly arrayed on a normalized frequency grid, directly corresponding to $n = 1, 2, 3, ...$

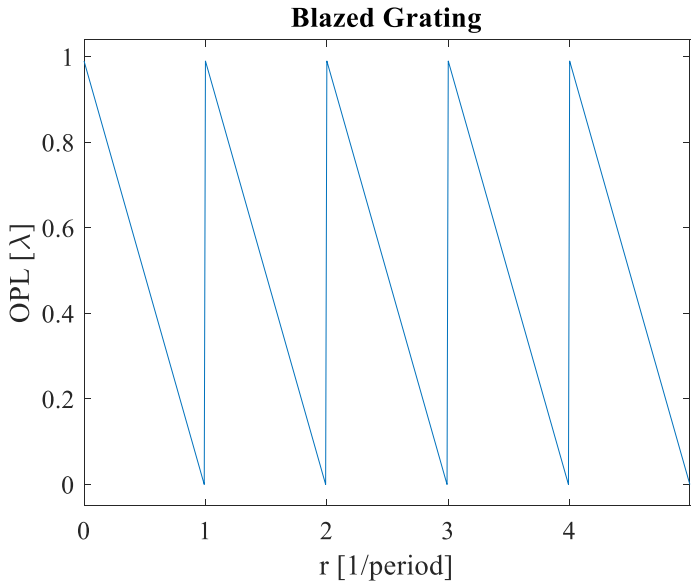

Figure V-11. Representation of the sawtooth grating used to simulate the Fresnel lens.

The simulation investigates the following sources of error in the lens fabrication (see Figure V-12): 1) Thresholding caused by residual oxygen following an incomplete flood cure (Lower Threshold). 2) Saturation of the material response following an over-exposure (Upper Threshold), 3) Variations in the peak optical path length caused by over/underexposure, or deviations in material thickness (OPL), and 4) Non-infinite phase jumps due to the finite patterning resolution (Phase Wrap Ramp) that result in a reverse ramp function between each ring. Each was varied in order to determine their effect on the diffraction efficiency of the lenses. This analysis only considers normal incidence of illumination, and does not consider non-normal angles of incidence. Any deviation in the incident wavelength is also accounted for by the variable OPL.

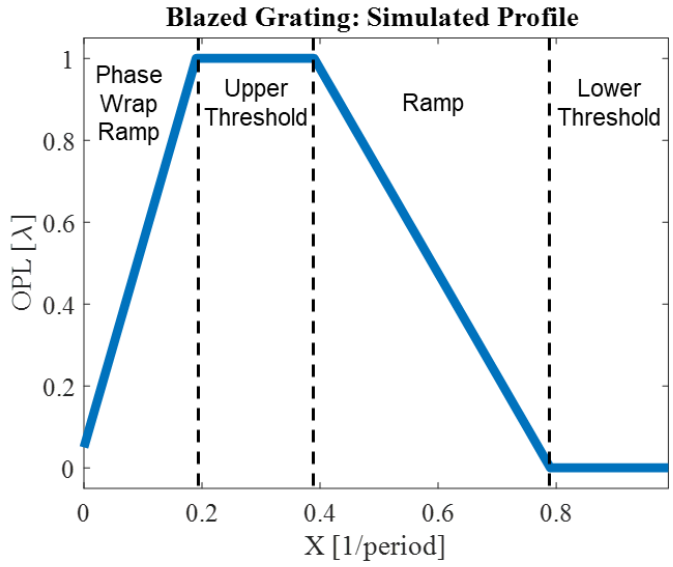

Simulation Parameter	Units
• Phase Wrap Ramp	Fraction of a period
• Upper Threshold	Fraction of a period
• OPL	Fraction of a wave
• Lower Threshold	Fraction of a period

Figure V-12. Image describing the simulated perturbations to the ideal grating profile. The phase wrap ramp represents a non-infinite phase jump between each period. The OPL is a bulk parameter accounting for the total phase delay due to material thickness and refractive index. Finally, the upper and lower thresholds represent nonlinear material response due to saturation and oxygen inhibition respectively.

The results shown in Figure V-13 were obtained by independently varying each of the above parameters while holding the others at their optimal value. For the blazed grating, optimal values are: $\mathrm{OPL} = 1$, $\mathrm{Phase\ Wrap\ Ramp} = 0$, and both Upper and Lower Threshold set to 0. The presence of any one of these faults channels power from the primary (1^{st}) order into both positive (converging) and negative (diverging) orders. This highlights the need for proper characterization of the photopolymer, as each of the above parameters can be caused by

improper exposure doses resulting from incomplete knowledge about the material's Δn vs dose curve.

The simulations in Figure V-13 also demonstrate the sensitivity of the first-order diffraction efficiency to variations in any of the four parameters. Of all four parameters, the first-order diffraction efficiency is most sensitive to the Phase Wrap Ramp [Figure V-13(b)]. If this feature occupies as little as 10% of the overall blaze period, diffraction efficiency in the first order falls by $\sim 20\%$. This relationship highlights the importance of achieving high patterning resolution and pixel densities in each of the blazed rings, especially as the desired NA of the Fresnel lens increases. As shown earlier, however, as the resolution of the optical patterning system increases, the depth of focus decreases, and limits the maximum allowable thickness of the photopolymer. Reduction of the material thickness, in turn, can only be realized by increasing the Δn range of the photopolymer.

Although the first-order diffraction efficiency is less sensitive to variations in either the OPL or threshold and saturation parameters, 20% variations in any of these parameters from their optimal value can reduce the first-order diffraction efficiency by up to 20%. This effect underscores the need to properly characterize of the material response in order to prescribe the correct exposure dose.

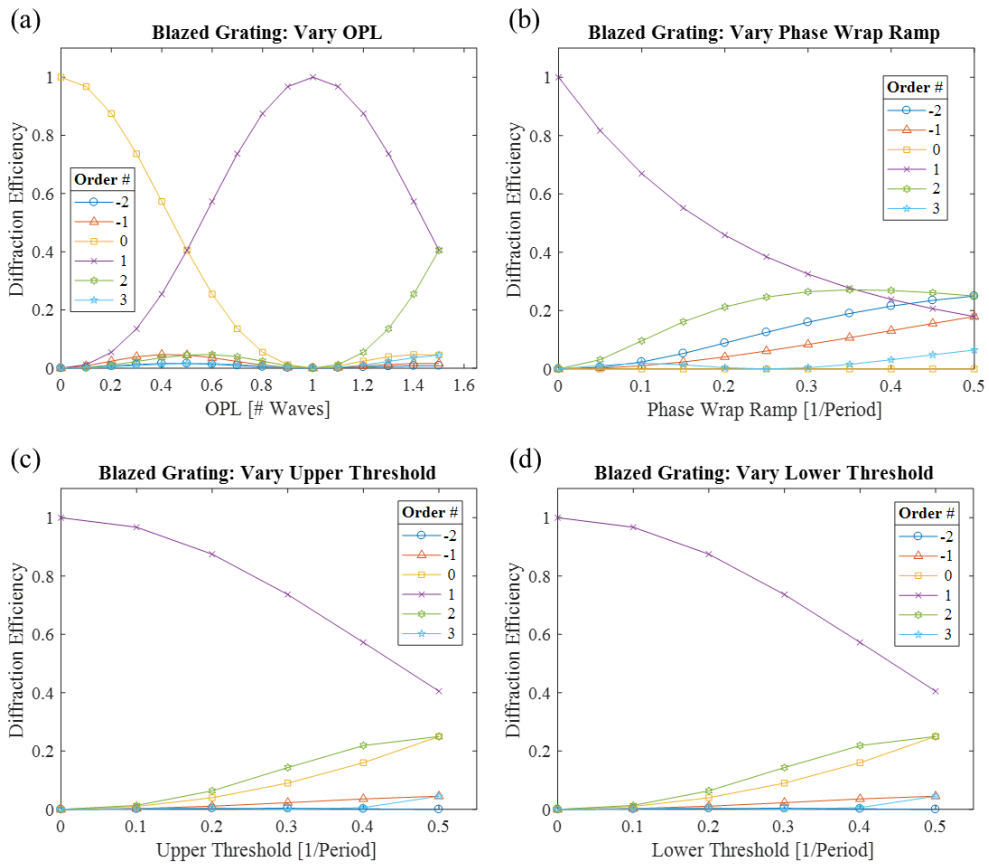

Figure V-13. Plots describing the variation in diffraction efficiency of the Fresnel lens for non-optimal conditions. (a) The change in diffraction efficiency for OPL deviations, assuming no threshold behavior and an infinite phase wrap slope. (b) The change in diffraction efficiency for variations in the sharpness of the phase wrap. (c-d) Changes in diffraction efficiency when threshold behavior is present (upper and lower respectively).

F. Conclusion

Using the knowledge from the characterization techniques I developed in the previous chapters, I have demonstrated the first high diffraction-efficiency (93%), 16 mm-diameter, one-diopter Fresnel lens inside of a two-stage photopolymer. The previous characterization via in-situ phase imaging allows me to incorporate the photopolymer's intensity response, Δn linearity, dynamic range, and oxygen threshold behavior in designing the appropriate exposure conditions for fabricating DOEs. Furthermore, I developed a facile method for patterning large, high-resolution grayscale Δn features using a binary chrome mask and a dithering process, which will

facilitate the future fabrication of arbitrary 2D diffractive optical elements in two-component photopolymers.

CHAPTER VI
FUTURE WORK

A. Chapter Overview

The preceding chapters demonstrated that accurate metrology of two-stage optical photopolymers enabled the fabrication of complex DOEs and offered insight into the fundamental limitations behind volume structuring. This knowledge provided both immediate practical use in establishing a Δn response curve to fabricate analog optical elements, and it revealed the physical limitations to achieving higher Δn in a given formulation. Future advancement in photostructuring must investigate strategies to overcome these limitations to obtain higher Δn. In order to address this challenge, the following chapter discusses potential solutions to increase the maximum dynamic range in two-stage photopolymer systems. I begin by discussing the impact of increased stage-2 monomer loading on both the maximum single- and multiple-exposure Δn in the model material. Because the solubility limit of stage-2 polymer/monomer within the stage-1 network contributes towards the maximum Δn, I then consider the effect of monomer functionality and crosslink density on the solubility limit of the stage-2 monomer. Lastly, I investigate methods for removing the unreacted background stage-2 species in order to further increase the Δn of the photostructured feature. After addressing these physical limitations to photostructuring within two-stage photopolymers, I then address the ability to fabricate conformal/flexible polymer optics using these materials.

B. Improving the Δn in Two-Stage Photopolymers

1. Increasing the stage-2 monomer loading to increase the single-exposure Δn

Chapter IV presented a plot (shown again in Figure VI-1) comparing the refractive indices of structures created using one or more exposures to the refractive index of the uncured background material at different initial stage-2 monomer loadings. The data shows that

increasing the initial volume fraction of stage-2 species within the matrix results in a higher Δn for single-exposure structures. These high concentrations enable greater mass transport of stage-2 species, resulting in larger concentration gradients and higher Δn. However, this trend does not extend to very high concentrations as evidenced by the decrease in the total Δn dynamic range for large volume fractions of stage-2 monomer. This decrease stems from the combined effect of increasing the background refractive index of the material and the apparent saturation limit imposed on the maximum photostructured refractive index. For high volume fractions of the initial stage-2 monomer, these limits will converge and ultimately constrain the maximum single-exposure Δn. In the extreme case, photostructuring into an already saturated material will fail to produce any Δn because the stage-2 species cannot diffuse. Thus, the data suggests that for single exposures there is an optimum stage-2 monomer loading that maximizes the single exposure Δn by maximizing the concentration gradient achieved through mass transport.

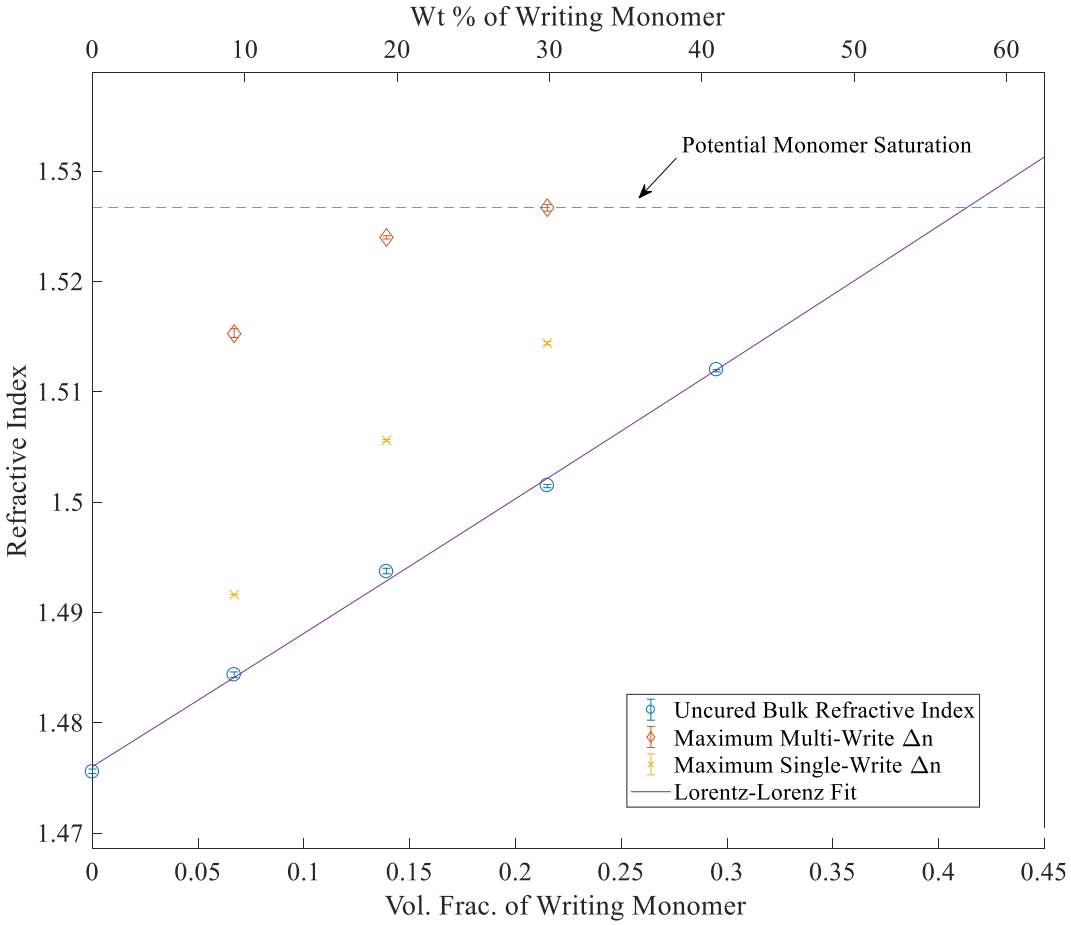

Figure VI-1. Plot from chapter IV showing the total refractive index of photostructured features produced using one or multiple exposures. The apparent monomer saturation limit (dashed line) and the increasing background refractive index (solid line) serve to constrain the maximum Δn that can be supported by the polymer for both single and multiple exposures.

Future work will verify the above conclusion by supplementing the data presented in Figure VI-1 through the measurement of the maximum single- and multiple-exposure Δn in material formulations with high initial volume fractions of stage-2 monomer. According to the above claim, as the initial volume fraction of stage-2 monomer increases, both the single- and multiple- exposure Δn will eventually decrease and fall to zero. The point at which this occurs will be the saturation limit of the stage-2 species within the stage-1 network, and will represent the maximum refractive index achievable by the two-stage photopolymer. This ability to assess

the upper limit of monomer solubility in a given two-stage photopolymer will assist in screening potential materials for performing photostructuring of optical features.

2. Removing the unreacted stage-2 monomer

As demonstrated in the previous chapters, the Δn of a photostructured feature represents the difference between the refractive indices of the feature and the unexposed background. Increases in Δn are achieved by increasing the local concentration of polymerized stage-2 species within the exposed structure. However, because Δn corresponds to a difference in the concentration of the stage-2 species, it can also be increased by removing unreacted stage-2 monomer from the background material. Removal of the unreacted stage-2 monomer will reduce the background concentration relative to the exposed feature, thereby increasing the Δn. This assumes that all monomer within the photostructured region has been immobilized such that the total refractive index of the exposed structure is unaffected by the removal of monomer. For example, if the material has a ~55 wt% monomer loading in the initial formulation and all of the local monomer is polymerized through a single exposure, this strategy can produce a Δn in the model material up to 0.05 for a single exposure.

Removal of unreacted monomer has been demonstrated in thin films by laminating a thick sheet of the neat stage-1 matrix onto the material. Mass transport through diffusion then draws the unreacted monomer into the empty stage-1 matrix. Fourier transform infrared spectroscopy reveals the effectiveness of this process (Figure VI-2). Initially, the acrylate peak at ~1610 cm^{-1} that corresponds to the stage-2 monomer is visible. After lamination and subsequent diffusion over 24 hours in a 70 ℃ oven, the peak disappears, indicating that the majority of unreacted monomer has been removed. Future work should expand this process to investigate the change in Δn of a photostructured feature after removal of the unreacted stage-2 monomer.

Concurrent to this investigation, the diffusivity of the stage-2 species into the neat stage-1 matrix can be measured through gravimetric analysis in order to determine the practicality of this technique for monomer removal. Furthermore, the dependence of this diffusivity on the ambient temperature of the material can also be explored using this technique. The ability to rapidly remove background stage-2 species will both enable increased Δn in photostructured materials and provide the ability to swap and incorporate multiple stage-2 species and material properties within a single volume.

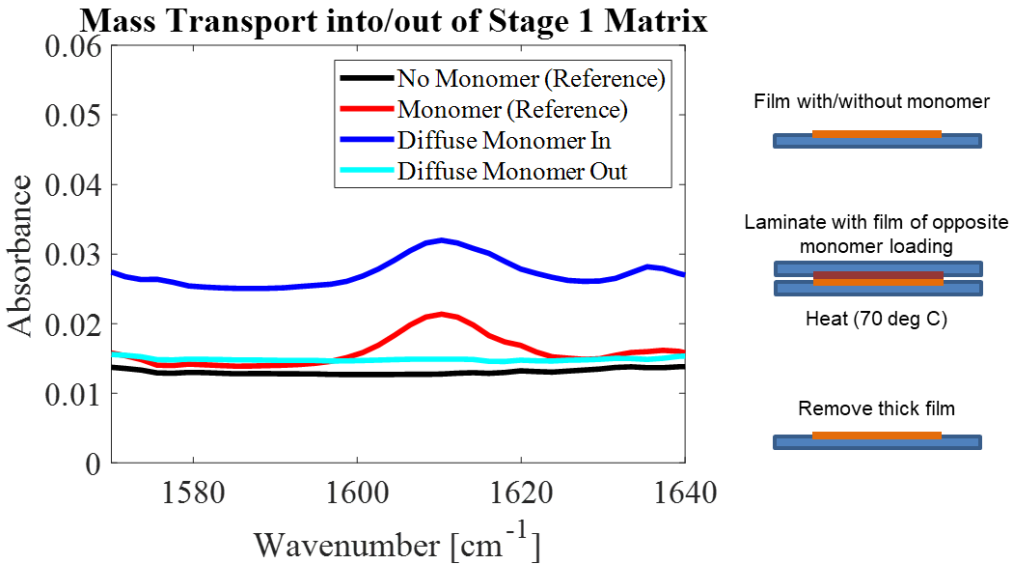

Figure VI-2. Attenuated total reflectance Fourier transform infrared spectroscopy (ATR-FTIR) used to measure the presence of unreacted stage-2 monomer within a thin layer of the two-stage polymer. The peak at ~1610 cm^{-1} indicates the presence of unreacted C=C bonds in the triacrylated urethane stage-2 monomer. After transferring the monomer into a neat stage-1 layer via mass transport, the peak is no longer visible in the original material (line labeled 'Diffuse Monomer Out'). The process can be reversed by laminating the neat stage-1 matrix with a layer that is swollen with stage-2 monomer (line labeled - Diffuse Monomer In).

3. Reducing the stage-2 network crosslink density

As seen in chapter IV the upper solubility limit of the stage-2 monomer is primarily attributed to an increased crosslink density caused by the photostructuring process. This crosslinking results from the polymerization of the multifunctional stage-2 monomer.

Preliminary measurements of crosslink density using dynamic mechanical analysis on uniformly structured samples support this claim. Figure VI-3 shows the increase in the crosslink density of the polymer after uniform polymerization of all the stage-2 species. The data shows that even after only a single exposure, photoinduced crosslinking of the stage-2 species can increase the crosslink density up to 10 times beyond that of the neat stage-1 matrix. Furthermore, the inset in Figure VI-3 highlights the decrease in additional Δn gained between the first exposure into a neat stage-1 matrix, and a second exposure into the developed structure with the increased crosslink density. As the crosslink density increases, the additional Δn gained by a new photoexposure decreases relative to the first. Thus, reducing the average functionality of the stage-2 monomer will reduce the crosslink density during photostructuring and consequently increase the solubility limit of the polymer. All else being equal, this change in the monomer functionality should allow greater Δn for each exposure during the multiple-exposure process.

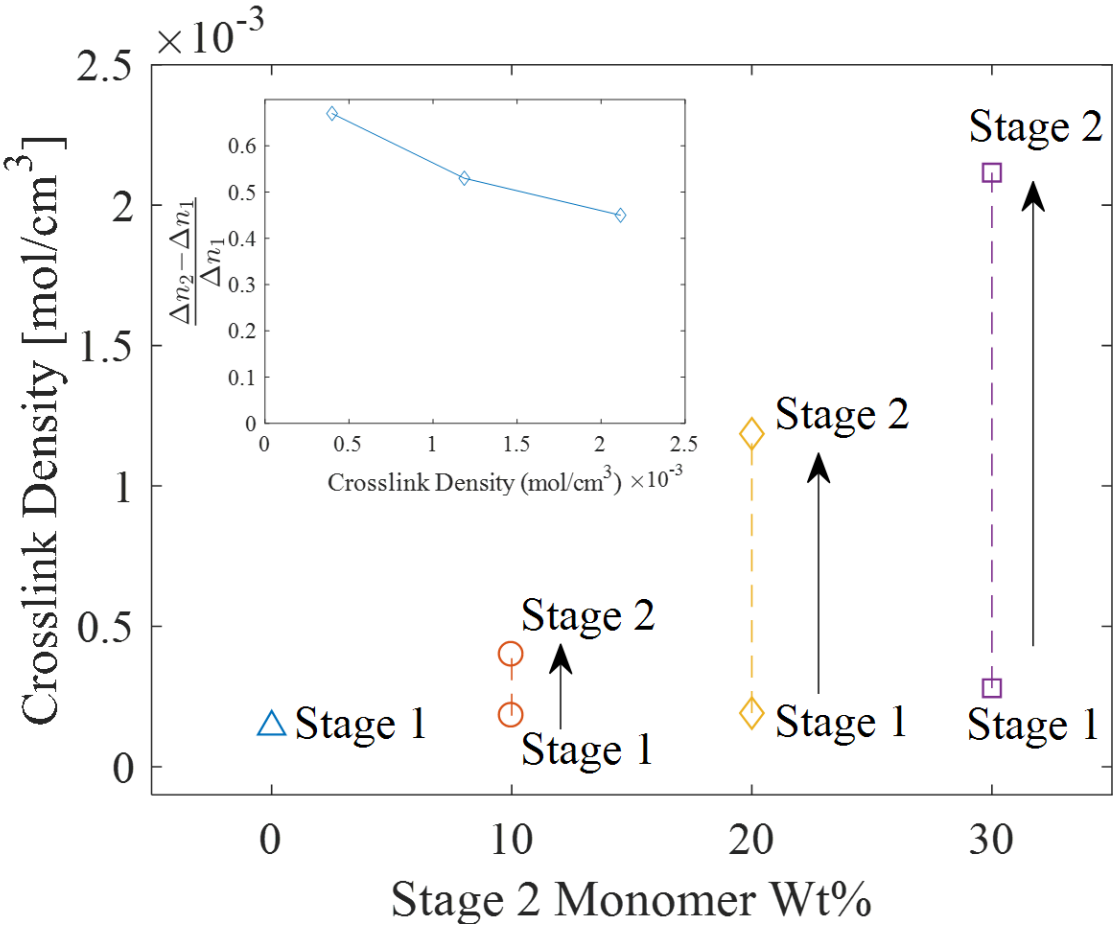

Figure VI-3. The effect of stage-2 monomer polymerization on the crosslink density of the photopolymer. As the initial weight percent of monomer increases, more polymer is formed during a single photostructuring step, and the crosslink density increases. The inset shows the dependence of polymer crosslink density on Δn. The vertical axis shows the relative gain in Δn after an initial photostructuring step in the stage-1 matrix (Δn_1) and photostructuring into a polymer with the given crosslink density (Δn_2).

Future work will investigate the dependence of monomer functionality and stage-2 crosslink density on the solubility limit of the photostructured polymer. Ideally, the only variation between the structures of the stage-2 components will be their functionality. Because the refractive index of the different stage-2 species may differ slightly, Δn should not be used to compare the effect of crosslinking on the upper solubility limit. Instead, comparisons should be made between the total concentration of stage-2 species in the exposed region. Such measurements can be determined through a similar process as shown in Figure VI-1.

It should be noted that reducing the stage-2 monomer functionality to a single group will prevent the formation of additional covalent crosslinks. While this can increase the solubility limit of the stage-2 species within the matrix compared to a multifunctional monomer, out-diffusion of the resulting linear polymer chains can negatively impact the final concentration of stage-2 species within the photostructured region. Thus, the ideal functionality of the stage-2 monomer will depend on both the final crosslink density and immobilization of the formed polymer chains.

C. Flexible Diffractive and Optical Phase Elements

While the presented work in chapters III-V only considered the photostructuring of optical features within a flat material, the ability to fabricate rubbery polymers with a T_g below room temperature will enable the creation of highly efficient, flexible and conformal optical devices. Because the material can be deformed after photostructuring, simplification of the exposure process can be achieved by patterning a flat 2D sheet and incorporating the final deformed shape into the exposure pattern. In order to leverage this capability, future work should explore the design and simulation of conformal optics to determine the best application of this technique.

D. Conclusion

Photostructured optical and mechanical elements offer vast potential for the fabrication of DOEs, shape programmable materials, and cell scaffolds. This work extended the understanding of photostructured polymers by presenting metrology techniques to accurately characterize optical and mechanical features created through either local or nonlocal reactions. I showed, in the case of local reactions, that bulk metrology of uniform material can describe the mechanical properties of photostructured features. This was demonstrated by using bulk characterization to investigate a

new class of shape programmable material, through which I fabricated a novel self-folding origami structure. In the case of nonlocal photostructuring reactions, I developed a quantitative metrology technique that combined QPI and confocal reflection microscopy to measure smoothly-varying, 2D structures. This method overcame the issue of incomplete overlap between the spatial frequency content of the photostructured object and the CTF of the measurement system, thereby enabling quantitative measurement of the in-situ material response. The predictive power afforded by this metrology and characterization allowed me to accurately design and fabricate a novel, high-diffraction efficiency, large diameter Fresnel lens. Additionally, this metrology enabled me to develop and explore a new photostructuring technique that used multiple exposures in optical two-stage photopolymers to increase the achievable Δn without requiring a change in the chemical formulation. In order to study the limitations of this technique, the previous metrology was further adapted to characterize dynamic processes such as diffusion of stage-2 monomer into the photostructured feature. The ability to both measure Δn and diffusivity revealed that increased crosslink density due to the multi-functional stage-2 monomer imposed the upper bound on Δn.

The demonstrated techniques to perform quantitative metrology will enable future study of photostructured features within photopolymers, and enable a new class of novel optical, mechanical, and biochemical devices.

BIBLIOGRAPHY

1. D. J. Glugla, M. D. Alim, K. D. Byars, D. P. Nair, C. N. Bowman, K. K. Maute, and R. R. McLeod, "Rigid Origami via Optical Programming and Deferred Self-Folding of a Two-Stage Photopolymer," ACS Appl. Mater. Interfaces **8**, 29658–29667 (2016).

2. Y. Zhang and L. Ionov, "Actuating porous polyimide films.," ACS Appl. Mater. Interfaces **6**, 10072–7 (2014).

3. M. Jamal, A. M. Zarafshar, and D. H. Gracias, "Differentially photo-crosslinked polymers enable self-assembling microfluidics.," Nat. Commun. **2**, 527 (2011).

4. T. D. Gerke and R. Piestun, "Aperiodic volume optics," Nat. Photonics **4**, 188 (2010).

5. R. Malallah, H. Li, D. Kelly, J. Healy, and J. Sheridan, "A Review of Hologram Storage and Self-Written Waveguides Formation in Photopolymer Media," Polymers (Basel). **9**, 337 (2017).

6. A. C. Sullivan, M. W. Grabowski, and R. R. McLeod, "Three-dimensional direct-write lithography into photopolymer," Appl. Opt. **46**, 295 (2007).

7. F.-K. Bruder, H. Bang, T. Fäcke, R. Hagen, D. Hönel, E. Orselli, C. Rewitz, T. Rölle, D. Vukicevic, and G. Walze, "Precision holographic optical elements in Bayfol HX photopolymer," in *Practical Holography XXX: Materials and Applications*, H. I. Bjelkhagen and V. M. Bove, eds. (International Society for Optics and Photonics, 2016), Vol. 9771, p. 977103.

8. H. Akbari, I. Naydenova, and S. Martin, "Using acrylamide-based photopolymers for fabrication of holographic optical elements in solar energy applications," Appl. Opt. **53**, 1343 (2014).

9. K. Miura, J. Qiu, H. Inouye, T. Mitsuyu, and K. Hirao, "Photowritten optical waveguides in various glasses with ultrashort pulse laser," Appl. Phys. Lett. **71**, 3329 (1997).

10. L. Vittadello, A. Zaltron, N. Argiolas, M. Bazzan, N. Rossetto, and R. Signorini, "Photorefractive direct laser writing," J. Phys. D. Appl. Phys. **49**, 125103 (2016).

11. C. A. DeForest, B. D. Polizzotti, and K. S. Anseth, "Sequential click reactions for synthesizing and patterning three-dimensional cell microenvironments," Nat. Mater. **8**, 659–664 (2009).

12. C. I. Fiedler, E. A. Aisenbrey, J. A. Wahlquist, C. M. Heveran, V. L. Ferguson, S. J. Bryant, and R. R. McLeod, "Enhanced mechanical properties of photo-clickable thiol–ene PEG hydrogels through repeated photopolymerization of in-swollen macromer," Soft Matter **12**, 9095–9104 (2016).

13. A. R. Studart, "Biological and Bioinspired Composites with Spatially Tunable Heterogeneous Architectures," Adv. Funct. Mater. **23**, 4423–4436 (2013).

14. B. A. Kowalski and R. R. McLeod, "Design concepts for diffusive holographic photopolymers," J. Polym. Sci. Part B Polym. Phys. **54**, 1021–1035 (2016).

15. H. H. Duc Nguyen, U. Hollenbach, U. Ostrzinski, K. Pfeiffer, S. Hengsbach, and J. Mohr, "Freeform three-dimensional embedded polymer waveguides enabled by external-diffusion assisted two-photon lithography," Appl. Opt. **55**, 1906 (2016).

16. A. C. Urness, K. Anderson, C. Ye, W. L. Wilson, and R. R. McLeod, "Arbitrary GRIN component fabrication in optically driven diffusive photopolymers," Opt. Express **23**, 264 (2015).

17. F.-K. Bruder, T. Fäcke, and T. Rölle, "The Chemistry and Physics of Bayfol® HX Film Holographic Photopolymer," Polymers (Basel). **9**, 472 (2017).

18. J. D. Musgraves, K. Richardson, and H. Jain, "Laser-induced structural modification, its mechanisms, and applications in glassy optical materials," Opt. Mater. Express **1**, 921 (2011).

19. D. P. Nair, N. B. Cramer, J. C. Gaipa, M. K. McBride, E. M. Matherly, R. R. McLeod, R. Shandas, and C. N. Bowman, "Two-Stage Reactive Polymer Network Forming Systems," Adv. Funct. Mater. **22**, 1502–1510 (2012).

20. D. P. Nair, N. B. Cramer, M. K. McBride, J. C. Gaipa, R. Shandas, and C. N. Bowman, "Enhanced Two-Stage Reactive Polymer Network Forming Systems.," Polymer. **53**, 2429–2434 (2012).

21. W. Heller, "Remarks on Refractive Index Mixture Rules," J. Phys. Chem. **69**, 1123–1129 (1965).

22. K. Curtis, L. Dhar, A. J. Hill, W. L. Wilson, and M. R. Ayres, *Holographic Data Storage: From Theory to Practical Systems*, 1st ed. (John Wiley & Sons Ltd, n.d.).

23. K. Menard, *Dynamic Mechanical Analysis* (CRC Press, 1999).

24. H. Czichos, T. Saito, and L. Smith, eds., *Springer Handbook of Materials Measurement Methods* (Springer Berlin Heidelberg, 2006).

25. M. Griepentrog, G. Krämer, and B. Cappella, "Comparison of nanoindentation and AFM methods for the determination of mechanical properties of polymers," Polym. Test. **32**, 455–460 (2013).

26. Y. Liu, J. Genzer, and M. D. Dickey, "“2D or Not 2D”: Shape-Programming Polymer Sheets," Prog. Polym. Sci. **52**, 79–106 (2015).

27. R. Geryak and V. V Tsukruk, "Reconfigurable and actuating structures from soft materials.," Soft Matter **10**, 1246–63 (2014).

28. A. R. Studart and R. M. Erb, "Bioinspired materials that self-shape through programmed microstructures.," Soft Matter **10**, 1284–94 (2014).

29. E. A. Peraza-Hernandez, D. J. Hartl, R. J. Malak Jr, and D. C. Lagoudas, "Origami-inspired active structures: a synthesis and review," Smart Mater. Struct. **23**, 94001 (2014).

30. X. Guo, H. Li, B. Y. Ahn, E. B. Duoss, K. J. Hsia, J. A. Lewis, and R. G. Nuzzo, "Two- and three-dimensional folding of thin film single-crystalline silicon for photovoltaic power applications.," Proc. Natl. Acad. Sci. U. S. A. **106**, 20149–54 (2009).

31. C. C. B. Bufon, J. D. C. González, D. J. Thurmer, D. Grimm, M. Bauer, and O. G. Schmidt, "Self-assembled ultra-compact energy storage elements based on hybrid nanomembranes.," Nano Lett. **10**, 2506–10 (2010).

32. G. Huang, Y. Mei, D. J. Thurmer, E. Coric, and O. G. Schmidt, "Rolled-up transparent microtubes as two-dimensionally confined culture scaffolds of individual yeast cells.," Lab Chip **9**, 263–8 (2009).

33. S. Zakharchenko, N. Puretskiy, G. Stoychev, M. Stamm, and L. Ionov, "Temperature controlled encapsulation and release using partially biodegradable thermo-magneto-sensitive self-rolling tubes," Soft Matter **6**, 2633–2636 (2010).

34. S. Zakharchenko, E. Sperling, and L. Ionov, "Fully biodegradable self-rolled polymer tubes: a candidate for tissue engineering scaffolds.," Biomacromolecules **12**, 2211–5 (2011).

35. M. Jamal, N. Bassik, J.-H. Cho, C. L. Randall, and D. H. Gracias, "Directed growth of fibroblasts into three dimensional micropatterned geometries via self-assembling scaffolds.," Biomaterials **31**, 1683–90 (2010).

36. N. Bassik, G. M. Stern, M. Jamal, and D. H. Gracias, "Patterning Thin Film Mechanical Properties to Drive Assembly of Complex 3D Structures," Adv. Mater. **20**, 4760–4764 (2008).

37. G. Stoychev, N. Puretskiy, and L. Ionov, "Self-folding all-polymer thermoresponsive microcapsules," Soft Matter **7**, 3277–3279 (2011).

38. E. Gultepe, J. S. Randhawa, S. Kadam, S. Yamanaka, F. M. Selaru, E. J. Shin, A. N. Kalloo, and D. H. Gracias, "Biopsy with thermally-responsive untethered microtools.," Adv. Mater. **25**, 514–9 (2013).

39. E. J. Smith, S. Schulze, S. Kiravittaya, Y. Mei, S. Sanchez, and O. G. Schmidt, "Lab-in-a-

tube: detection of individual mouse cells for analysis in flexible split-wall microtube resonator sensors.," Nano Lett. **11**, 4037–42 (2011).

40. S. Zakharchenko, N. Puretskiy, G. Stoychev, C. Waurisch, S. G. Hickey, A. Eychmüller, J.-U. Sommer, and L. Ionov, "Stimuli-responsive hierarchically self-assembled 3D porous polymer-based structures with aligned pores," J. Mater. Chem. B **1**, 1786–1793 (2013).

41. Y. Mei, D. J. Thurmer, C. Deneke, S. Kiravittaya, Y.-F. Chen, A. Dadgar, F. Bertram, B. Bastek, A. Krost, J. Christen, T. Reindl, M. Stoffel, E. Coric, and O. G. Schmidt, "Fabrication, self-assembly, and properties of ultrathin AlN/GaN porous crystalline nanomembranes: tubes, spirals, and curved sheets.," ACS Nano **3**, 1663–8 (2009).

42. J. L. Silverberg, A. A. Evans, L. McLeod, R. C. Hayward, T. Hull, C. D. Santangelo, and I. Cohen, "Using origami design principles to fold reprogrammable mechanical metamaterials," Science. **345**, 647–650 (2014).

43. D. Morales, E. Palleau, M. D. Dickey, and O. D. Velev, "Electro-actuated hydrogel walkers with dual responsive legs.," Soft Matter **10**, 1337–48 (2014).

44. S. Schwaiger, M. Bröll, A. Krohn, A. Stemmann, C. Heyn, Y. Stark, D. Stickler, D. Heitmann, and S. Mendach, "Rolled-Up Three-Dimensional Metamaterials with a Tunable Plasma Frequency in the Visible Regime," Phys. Rev. Lett. **102**, 163903 (2009).

45. E. J. Smith, Z. Liu, Y. F. Mei, and O. G. Schmidt, "System investigation of a rolled-up metamaterial optical hyperlens structure," Appl. Phys. Lett. **95**, 83104 (2009).

46. E. A. Peraza-Hernandez, D. J. Hartl, R. J. Malak Jr, and D. C. Lagoudas, "Origami-inspired active structures: a synthesis and review," Smart Mater. Struct. **23**, 94001 (2014).

47. F. Liu and M. W. Urban, "Recent advances and challenges in designing stimuli-responsive polymers," Prog. Polym. Sci. **35**, 3–23 (2010).

48. N. Bassik, B. T. Abebe, K. E. Laflin, and D. H. Gracias, "Photolithographically patterned smart hydrogel based bilayer actuators," Polymer. **51**, 6093–6098 (2010).

49. J.-H. Na, A. A. Evans, J. Bae, M. C. Chiappelli, C. D. Santangelo, R. J. Lang, T. C. Hull, and R. C. Hayward, "Programming Reversibly Self-Folding Origami with Micropatterned Photo-Crosslinkable Polymer Trilayers.," Adv. Mater. **27**, 79–85 (2014).

50. X. Mu, N. Sowan, J. A. Tumbic, C. N. Bowman, P. T. Mather, and H. J. Qi, "Photo-induced bending in a light-activated polymer laminated composite.," Soft Matter **11**, 2673–82 (2015).

51. M. T. Tolley, S. M. Felton, S. Miyashita, D. Aukes, D. Rus, and R. J. Wood, "Self-folding origami: shape memory composites activated by uniform heating," Smart Mater. Struct. **23**, 94006 (2014).

52. K. Suzuki, H. Yamada, H. Miura, and H. Takanobu, "Self-assembly of three dimensional micro mechanisms using thermal shrinkage of polyimide," Microsyst. Technol. **13**, 1047–1053 (2006).

53. C. Yoon, R. Xiao, J. Park, J. Cha, T. D. Nguyen, and D. H. Gracias, "Functional stimuli responsive hydrogel devices by self-folding," Smart Mater. Struct. **23**, 94008 (2014).

54. M. Jamal, A. M. Zarafshar, and D. H. Gracias, "Differentially photo-crosslinked polymers enable self-assembling microfluidics.," Nat. Commun. **2**, 527 (2011).

55. K. Fuchi, T. H. Ware, P. R. Buskohl, G. W. Reich, R. A. Vaia, T. J. White, and J. J. Joo, "Topology optimization for the design of folding liquid crystal elastomer actuators.," Soft Matter **11**, 7288–95 (2015).

56. N. Tabiryan, S. Serak, X.-M. Dai, and T. Bunning, "Polymer film with optically controlled form and actuation," Opt. Express **13**, 7442 (2005).

57. M. Podgórski, D. P. Nair, S. Chatani, G. Berg, and C. N. Bowman, "Programmable mechanically assisted geometric deformations of glassy two-stage reactive polymeric materials.," ACS Appl. Mater. Interfaces **6**, 6111–9 (2014).

58. J. Ryu, M. D'Amato, X. Cui, K. N. Long, H. Jerry Qi, and M. L. Dunn, "Photo-origami—Bending and folding polymers with light," Appl. Phys. Lett. **100**, 161908 (2012).

59. S. Felton, M. Tolley, E. Demaine, D. Rus, and R. Wood, "A method for building self-folding machines," Science. **345**, 644–646 (2014).

60. M. Behl, M. Y. Razzaq, and A. Lendlein, "Multifunctional shape-memory polymers.," Adv. Mater. **22**, 3388–410 (2010).

61. J. M. Cuevas, R. Rubio, L. Germán, J. M. Laza, J. L. Vilas, M. Rodriguez, and L. M. León, "Triple-shape memory effect of covalently crosslinked polyalkenamer based semicrystalline polymer blends," Soft Matter **8**, 4928 (2012).

62. Y. Liu, J. K. Boyles, J. Genzer, and M. D. Dickey, "Self-folding of polymer sheets using local light absorption," Soft Matter **8**, 1764–1769 (2012).

63. N. Turner, B. Goodwine, and M. Sen, "A review of origami applications in mechanical engineering," Proc. Inst. Mech. Eng., Part C **230**, 2345–2362 (2015).

64. G. Landini, "ThreePointCircularROI," (n.d.).

65. L. W. Hill, "Calculation of crosslink density in short chain networks," Prog. Org. Coatings **31**, 235–243 (1997).

66. S. Ye, N. B. Cramer, and C. N. Bowman, "Relationship between Glass Transition Temperature and Polymerization Temperature for Cross-Linked Photopolymers," Macromolecules **44**, 490–494 (2011).

67. S. P. Timoshenko and J. N. Goodier, *Theory of Elasticity*, 3rd ed. (McGraw-Hill Publishing Company, 1970).

68. B. H. Hanna, J. M. Lund, R. J. Lang, S. P. Magleby, and L. L. Howell, "Waterbomb base: a symmetric single-vertex bistable origami mechanism," Smart Mater. Struct. **23**, 94009 (2014).

69. D. J. Glugla, M. B. Chosy, M. D. Alim, A. C. Sullivan, and R. R. McLeod, "Transport-of-intensity-based phase imaging to quantify the refractive index response of 3D direct-write lithography," Opt. Express **26**, 1851 (2018).

70. K. M. Davis, K. Miura, N. Sugimoto, and K. Hirao, "Writing waveguides in glass with a femtosecond laser," Opt. Lett. **21**, 1729 (1996).

71. S. Nolte, M. Will, J. Burghoff, and A. Tuennermann, "Femtosecond waveguide writing: a new avenue to three-dimensional integrated optics," Appl. Phys. A Mater. Sci. Process. **77**, 109–111 (2003).

72. B. L. Booth, "Low loss channel waveguides in polymers," J. Light. Technol. **7**, 1445–1453 (1989).

73. S. Bichler, S. Feldbacher, R. Woods, V. Satzinger, V. Schmidt, G. Jakopic, G. Langer, and W. Kern, "Functional flexible organic-inorganic hybrid polymer for two photon patterning of optical waveguides," Opt. Mater. **34**, 772–780 (2012).

74. R. Woods, S. Feldbacher, D. Zidar, G. Langer, V. Satzinger, V. Schmidt, N. Pucher, R. Liska, and W. Kern, "3D optical waveguides produced by two photon photopolymerisation of a flexible silanol terminated polysiloxane containing acrylate functional groups," Opt. Mater. Express **4**, 486 (2014).

75. C. Ye, K. T. Kamysiak, A. C. Sullivan, and R. R. McLeod, "Mode profile imaging and loss measurement for uniform and tapered single-mode 3D waveguides in diffusive photopolymer," Opt. Express **20**, 6575 (2012).

76. R. R. McLeod, A. J. Daiber, M. E. McDonald, T. L. Robertson, T. Slagle, S. L. Sochava, and L. Hesselink, "Microholographic multilayer optical disk data storage," Appl. Opt. **44**, 3197 (2005).

77. H. J. Eichler, P. Kuemmel, S. Orlic, and A. Wappelt, "High-density disk storage by multiplexed microholograms," IEEE J. Sel. Top. Quantum Electron. **4**, 840–848 (1998).

78. T. Volk and M. Wöhlecke, "Problem of a Non-Erasable Photorefractive Hologram," in

Lithium Niobate: Defects, Photorefraction and Ferroelectric Switching (Springer, Berlin, Heidelberg, 2008), pp. 103–137.

79. O. M. Efimov, L. B. Glebov, and V. I. Smirnov, "Diffractive optical elements in photosensitive inorganic glasses," in A. J. Marker III and M. J. Davis, eds. (International Society for Optics and Photonics, 2001), Vol. 4452, pp. 39–47.

80. E. N. Glezer, M. Milosavljevic, L. Huang, R. J. Finlay, T.-H. Her, J. P. Callan, and E. Mazur, "Three-dimensional optical storage inside transparent materials," Opt. Lett. **21**, 2023 (1996).

81. R. R. Gattass and E. Mazur, "Femtosecond laser micromachining in transparent materials," Nat. Photonics **2**, 219–225 (2008).

82. A. Zanutta, E. Orselli, T. Fäcke, and A. Bianco, "Photopolymeric films with highly tunable refractive index modulation for high precision diffractive optics," Opt. Mater. Express **6**, 252 (2016).

83. R. Woods, S. Feldbacher, D. Zidar, G. Langer, V. Satzinger, V. Schmidt, N. Pucher, R. Liska, and W. Kern, "3D optical waveguides produced by two photon photopolymerisation of a flexible silanol terminated polysiloxane containing acrylate functional groups," Opt. Mater. Express **4**, 486 (2014).

84. S. Klein, A. Barsella, H. Leblond, H. Bulou, A. Fort, C. Andraud, G. Lemercier, J. C. Mulatier, and K. Dorkenoo, "One-step waveguide and optical circuit writing in photopolymerizable materials processed by two-photon absorption," Appl. Phys. Lett. **86**, 211118 (2005).

85. B. A. Kowalski, A. C. Urness, M.-E. Baylor, M. C. Cole, W. L. Wilson, and R. R. McLeod, "Quantitative modeling of the reaction/diffusion kinetics of two-chemistry diffusive photopolymers," Opt. Mater. Express **4**, 1668 (2014).

86. J. Guo, M. R. Gleeson, and J. T. Sheridan, "A Review of the Optimisation of Photopolymer Materials for Holographic Data Storage," Phys. Res. Int. **2012**, 1–16 (2012).

87. H. Arimoto, W. Watanabe, K. Masaki, and T. Fukuda, "Measurement of refractive index change induced by dark reaction of photopolymer with digital holographic quantitative phase microscopy," Opt. Commun. **285**, 4911–4917 (2012).

88. H. Li, Y. Qi, and J. T. Sheridan, "Three-dimensional extended nonlocal photopolymerization driven diffusion model Part I Absorption," J. Opt. Soc. Am. B **31**, 2638 (2014).

89. H. Li, Y. Qi, and J. T. Sheridan, "Three-dimensional extended nonlocal photopolymerization driven diffusion model Part II Photopolymerization and model

development," J. Opt. Soc. Am. B **31**, 2648 (2014).

90. H. Kogelnik, "Coupled Wave Theory for Thick Hologram Gratings," Bell Syst. Tech. J. **48**, 2909–2947 (1969).

91. R. Osellame, N. Chiodo, V. Maselli, A. Yin, M. Zavelani-Rossi, G. Cerullo, P. Laporta, L. Aiello, S. De Nicola, P. Ferraro, A. Finizio, and G. Pierattini, "Optical properties of waveguides written by a 26 MHz stretched cavity Ti:sapphire femtosecond oscillator," Opt. Express **13**, 612 (2005).

92. V. Apostolopoulos, L. Laversenne, T. Colomb, C. Depeursinge, R. P. Salathé, M. Pollnau, R. Osellame, G. Cerullo, and P. Laporta, "Femtosecond-irradiation-induced refractive-index changes and channel waveguiding in bulk Ti3+:Sapphire," Appl. Phys. Lett. **85**, 1122–1124 (2004).

93. M. S. Dinleyici and C. Sümer, "Characterization and estimation of refractive index profile of laser-written photopolymer optical waveguides," Opt. Commun. **284**, 5067–5071 (2011).

94. A. C. Sullivan and R. R. McLeod, "Tomographic reconstruction of weak, replicated index structures embedded in a volume," Opt. Express **15**, 14202 (2007).

95. H.-B. Sun, T. Tanaka, and S. Kawata, "Three-dimensional focal spots related to two-photon excitation," Appl. Phys. Lett. **80**, 3673 (2002).

96. M. Young, "Optical fiber index profiles by the refracted-ray method (refracted near-field scanning)," Appl. Opt. **20**, 3415 (1981).

97. M. Mir, B. Bhaduri, R. Wang, R. Zhu, and G. Popescu, "Quantitative Phase Imaging," in *Progress in Optics* (Elsevier B.V., 2012), Vol. 57, pp. 133–217.

98. A. Jesacher, P. S. Salter, and M. J. Booth, "Refractive index profiling of direct laser written waveguides: tomographic phase imaging," Opt. Mater. Express **3**, 1223 (2013).

99. M. Reed Teague, "Deterministic phase retrieval: a Green's function solution," J. Opt. Soc. Am. **73**, 1434 (1983).

100. T. Wilson, Y. Kawata, and S. Kawata, "Readout of three-dimensional optical memories," Opt. Lett. **21**, 1003 (1996).

101. Covestro, "Bayfol HX200 Datasheet," https://www.films.covestro.com/en/Products/Bayfol/ProductList/201603170508/Bayfol-HX200.

102. W. J. Gambogi, Jr., A. M. Weber, and T. J. Trout, "Advances and applications of DuPont holographic photopolymers," in *Holographic Imaging and Materials*, T. H. Jeong, ed.

(International Society for Optics and Photonics, 1994), Vol. 2043, p. 2.

103. M. R. Ayres, K. Anderson, F. Askham, B. Sissom, and A. C. Urness, "Holographic data storage at 2+ Tbit/in2," in *Practical Holography XXIX: Materials and Applications*, H. I. Bjelkhagen and V. M. Bove, eds. (2015), p. 93860G.

104. H. Berneth, F. K. Bruder, T. Fäcke, R. Hagen, D. Hönel, D. Jurbergs, T. Rölle, and M.-S. Weiser, "Holographic recording aspects of high-resolution Bayfol HX photopolymer," in *Practical Holography XXV: Materials and Applications*, H. I. Bjelkhagen, ed. (International Society for Optics and Photonics, 2011), p. 79570H.

105. T. Roelle, F.-K. Bruder, T. Faecke, M.-S. Weiser, D. Hoenel, and N. Stoeckel, "Photopolymer Compositions for Optical Elements and Visual Displays," U.S. patent 12/569,184 (2009).

106. R. H. Webb, "Confocal optical microscopy," Reports Prog. Phys. **59**, 427–471 (1996).

107. L. J. Allen and M. P. Oxley, "Phase retrieval from series of images obtained by defocus variation," Opt. Commun. **199**, 65–75 (2001).

108. T. . Gureyev and K. . Nugent, "Rapid quantitative phase imaging using the transport of intensity equation," Opt. Commun. **133**, 339–346 (1997).

109. T. E. Gureyev, A. Roberts, and K. A. Nugent, "Partially coherent fields, the transport-of-intensity equation, and phase uniqueness," J. Opt. Soc. Am. A **12**, 1942 (1995).

110. N. Streibl, "Phase imaging by the transport equation of intensity," Opt. Commun. **49**, 6–10 (1984).

111. C. J. R. Sheppard, "Defocused transfer function for a partially coherent microscope and application to phase retrieval," J. Opt. Soc. Am. A **21**, 828 (2004).

112. D. Paganin, A. Barty, P. J. McMahon, and K. A. Nugent, "Quantitative phase-amplitude microscopy. III. The effects of noise.," J. Microsc. **214**, 51–61 (2004).

113. J. Martinez-Carranza, K. Falaggis, and T. Kozacki, "Multi-filter transport of intensity equation solver with equalized noise sensitivity," Opt. Express **23**, 23092 (2015).

114. L. Waller, L. Tian, and G. Barbastathis, "Transport of Intensity phase-amplitude imaging with higher order intensity derivatives.," Opt. Express **18**, 12552–61 (2010).

115. J. Martinez-Carranza, K. Falaggis, and T. Kozacki, "Optimum plane selection for transport-of-intensity-equation-based solvers.," Appl. Opt. **53**, 7050–8 (2014).

116. Z. Jingshan, R. A. Claus, J. Dauwels, L. Tian, and L. Waller, "Transport of Intensity phase imaging by intensity spectrum fitting of exponentially spaced defocus planes.," Opt.

Express **22**, 10661–74 (2014).

117. J. Martinez-Carranza, K. Falaggis, and T. Kozacki, "Solution to the Boundary problem for Fourier and Multigrid transport equation of intensity based solvers," Photonics Lett. Pol. **7**, 2–4 (2015).

118. A. K. O'Brien and C. N. Bowman, "Impact of Oxygen on Photopolymerization Kinetics and Polymer Structure," Macromolecules **39**, 2501–2506 (2006).

119. C. Decker and A. D. Jenkins, "Kinetic approach of oxygen inhibition in ultraviolet- and laser-induced polymerizations," Macromolecules **18**, 1241–1244 (1985).

120. L. Feng and B. I. Suh, "Exposure Reciprocity Law in Photopolymerization of Multi-Functional Acrylates and Methacrylates," Macromol. Chem. Phys. **208**, 295–306 (2007).

121. J. H. Kwon, H. C. Hwang, and K. C. Woo, "Analysis of temporal behavior of beams diffracted by volume gratings formed in photopolymers," J. Opt. Soc. Am. B **16**, 1651 (1999).

122. T. F. Scott, C. J. Kloxin, D. L. Forman, R. R. McLeod, C. N. Bowman, C. Eggeling, S. W. Hell, T. Kogej, M. D. Levin, S. R. Marder, D. McCord-Maughon, J. W. Perry, H. Rockel, M. Rumi, C. Subramaniam, W. W. Webb, X. L. Wu, and C. Xu, "Principles of voxel refinement in optical direct write lithography," J. Mater. Chem. **21**, 14150 (2011).

123. M. Ams, G. D. Marshall, D. J. Spence, and M. J. Withford, "Slit beam shaping method for femtosecond laser direct-write fabrication of symmetric waveguides in bulk glasses," Opt. Express **13**, 5676 (2005).

124. D. J. Glugla, M. B. Chosy, M. D. Alim, K. K. Childress, A. C. Sullivan, and R. R. McLeod, "Multiple patterning of holographic photopolymers for increased refractive index contrast," Opt. Lett. **43**, 1866 (2018).

125. G. D. Marshall, M. Ams, and M. J. Withford, "Direct laser written waveguide-Bragg gratings in bulk fused silica," Opt. Lett. **31**, 2690 (2006).

126. A. Žukauskas, I. Matulaitienė, D. Paipulas, G. Niaura, M. Malinauskas, and R. Gadonas, "Tuning the refractive index in 3D direct laser writing lithography: towards GRIN microoptics," Laser Photon. Rev. **9**, 706–712 (2015).

127. T. Babeva, I. Naydenova, S. Martin, and V. Toal, "Method for characterization of diffusion properties of photopolymerisable systems," Opt. Express **16**, 8487 (2008).

128. J. Kumpfmueller, K. Stadlmann, Z. Li, V. Satzinger, J. Stampfl, and R. Liska, "Two-photon-induced thiol-ene polymerization as a fabrication tool for flexible optical waveguides," Des. Monomers Polym. (2013).

129. G. Vallerotto, M. Victoria, S. Askins, R. Herrero, C. Domínguez, I. Antón, and G. Sala, "Design and modeling of a cost-effective achromatic Fresnel lens for concentrating photovoltaics," Opt. Express **24**, A1245 (2016).

130. P. J. Valle and M. P. Cagigal, "Analytic design of multiple-axis, multifocal diffractive lenses," Opt. Lett. **37**, 1121 (2012).

131. S. Ravikumar, A. Bradley, and L. N. Thibos, "Chromatic aberration and polychromatic image quality with diffractive multifocal intraocular lenses," J. Cataract Refract. Surg. **40**, 1192–1204 (2014).

132. T. Suhara, K. Kobayashi, H. Nishihara, and J. Koyama, "Graded-index Fresnel lenses for integrated optics," Appl. Opt. **21**, 1966 (1982).

133. V. Gandhi, J. Orava, H. Tuovinen, T. Saastamoinen, J. Laukkanen, S. Honkanen, and M. Hauta-Kasari, "Diffractive optical elements for optical identification," Appl. Opt. **54**, 1606 (2015).

134. G. Li, D. Lee, Y. Jeong, J. Cho, and B. Lee, "Holographic display for see-through augmented reality using mirror-lens holographic optical element," Opt. Lett. **41**, 2486 (2016).

135. G. J. Swanson and W. B. Veldkamp, "High-efficiency, multilevel, diffractive optical elements," U.S. patent US07801034 (December 2, 1991).

136. H. Jiang, X. Yuan, Z. Yun, Y.-C. Chan, and Y.-L. Lam, "Fabrication of microlens in photosensitive hybrid sol–gel films using a gray scale mask," Mater. Sci. Eng. C **16**, 99–102 (2001).

137. W. Yu and X. Yuan, "Localized self-volume growth in hybrid sol-gel glass induced by ultraviolet radiation with a gray-scale mask," Appl. Opt. **43**, 575 (2004).

138. J. Zhou, L. Li, N. Naples, T. Sun, and A. Y. Yi, "Fabrication of continuous diffractive optical elements using a fast tool servo diamond turning process," J. Micromechanics Microengineering **23**, 75010 (2013).

139. A. C. Urness, K. Anderson, C. Ye, W. L. Wilson, and R. R. McLeod, "Arbitrary GRIN component fabrication in optically driven diffusive photopolymers," Opt. Express **23**, 264 (2015).

140. C. Ye and R. R. McLeod, "GRIN lens and lens array fabrication with diffusion-driven photopolymer," Opt. Lett. **33**, 2575 (2008).

141. G. J. Swanson, *Binary Optics Technology: The Theory and Design of Multi-Level Diffractive Optical Elements* (1989).

142. D. C. O'Shea, T. J. Suleski, A. D. Kathman, and D. W. Prather, *Diffractive Optics: Design, Fabrication, and Test* (SPIE, 2003).

143. B. E. A. Saleh and M. C. Teich, *Fundamentals of Photonics*, 2nd ed. (John Wiley & Sons, Inc., 2007).

144. F.-K. Bruder, T. Fäcke, R. Hagen, D. Hönel, T. P. Kleinschmidt, E. Orselli, C. Rewitz, T. Rölle, and G. Walze, "Diffractive optics in large sizes: computer-generated holograms (CGH) based on Bayfol HX photopolymer," in L.-C. Chien, S.-D. Lee, and M. H. Wu, eds. (International Society for Optics and Photonics, 2015), Vol. 9385, p. 93850C.

145. M. D. Goodner and C. N. Bowman, "Modeling Primary Radical Termination and Its Effects on Autoacceleration in Photopolymerization Kinetics," Macromolecules **32**, 6552–6559 (1999).

APPENDIX I
SUPPORTING INFORMATION FOR CHAPTER II

A. Predicting the Mechanical Properties in a UV-Exposed Absorptive Strip

1. Initial assumptions

Conversion between applied optical exposure dose and the corresponding material properties is achieved by assuming the rate of polymerization, R_p, follows a square root dependence on the exposure intensity as seen by the following equation,

$$R_p = k_p \left(\frac{\phi \varepsilon I_0 [I]}{E k_t} \right)^{1/2} [M] \tag{7.1}$$

where k_p is the polymerization rate constant, ϕ is the initiator efficiency, $[M]$ is the instantaneous concentration of double bonds, ϵ is the molar absorptivity of the initiator, $[I]$ is the initiator concentration, and I_0 is the incident light intensity [145]. This equation results from a pseudo steady state approximation and the assumption of bimolecular termination being the dominant radical termination mechanism. FTIR data obtained from multiple samples of stage-1 material that were exposed to varying light intensities supports this claim, as seen in Figure VIII-1. The rate of polymerization vs. conversion is plotted, normalized by either the exposure intensity (I) or square root of the intensity $(\sqrt{I})$. If bimolecular termination dominates, the rate of polymerization at different intensities will be equal when normalized by $\sqrt{I}$. This is the observed case as seen in Figure VIII-1.

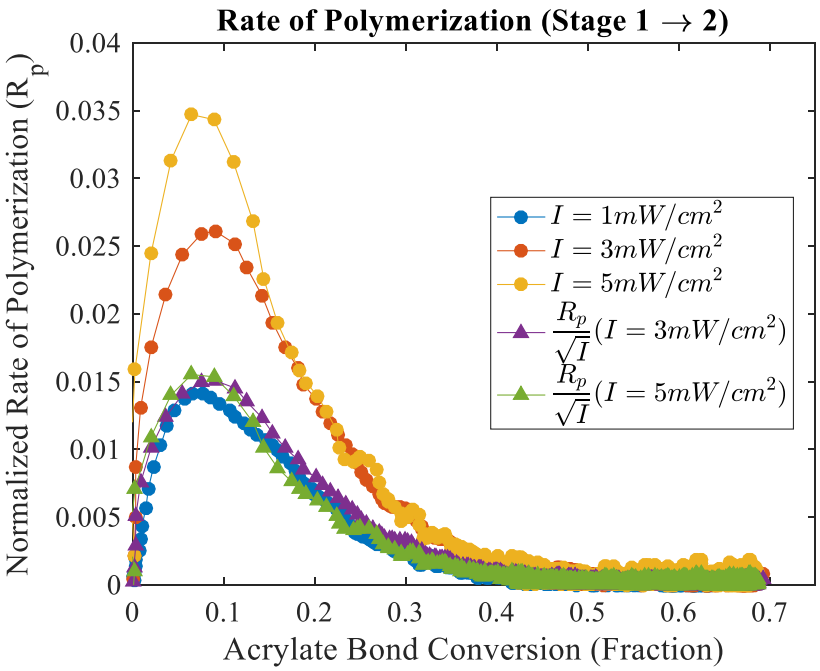

Figure VIII-1. The rate of polymerization normalized by either the incident exposure intensity (I) or the square root of the intensity $(\sqrt{I})$ and plotted vs. the relative stage-1 to stage-2 acrylate conversion.

2. Determining the mechanical properties as a function of depth

The predicted profiles of mechanical properties are generated using the data in Figure II-2. For a given incident exposure intensity and a known material absorbance, the Beer-Lambert law is used to determine the applied intensity as a function of depth, z, within the strip. Given the exposure time, t, and intensity as a function of distance into the strip, $I(z)$, an "effective dose", D_{eff}, is computed using $D_{eff}(z) = \sqrt{I(z)}t$. Then, by scaling the data from Figure II-2 by $D_{eff}(z)$ rather than dose $(I(z)t)$, the appropriate mechanical property may be determined through interpolation at a given depth within the strip.

Curves of relevant mechanical properties for different incident exposure doses are shown in

Figure VIII-2. As the applied exposure dose increases, more of the strip is converted to stage 2. Although the tensile modulus, and therefore the bending stiffness, increase with applied dose, the bending moment and neutral axis exhibit more complex behavior as they depend on both the tensile modulus and swelling strain.

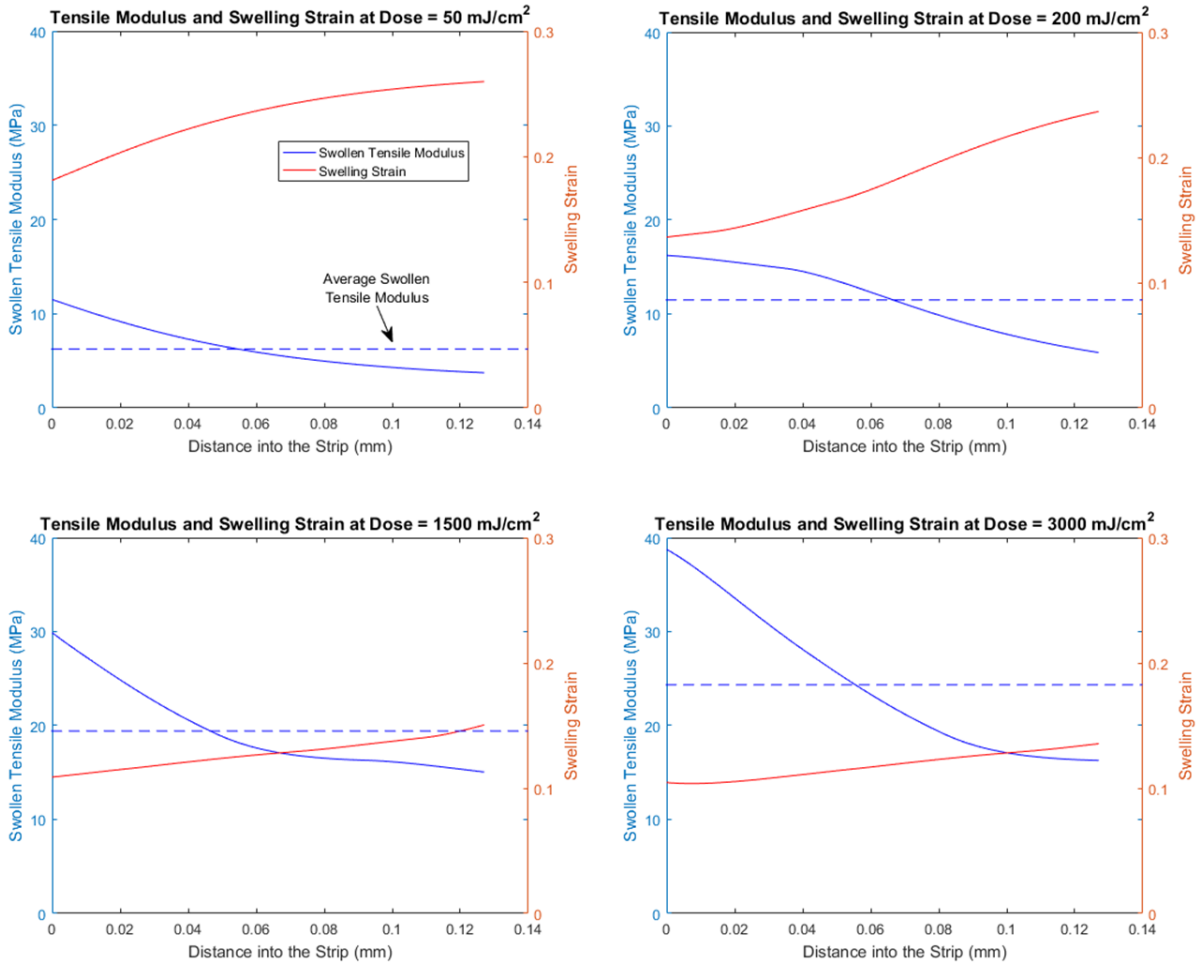

Figure VIII-2. Profiles of the tensile modulus and swelling strain as a function of depth into the strip for different doses. The front surface exposure intensity is 5 mW/cm^2. As the exposure dose increases, more of the strip converts to stage 2, resulting in an increase in the tensile modulus and decrease in swelling strain.

B. Simulating the Bend Radius of Curvature Using a Nonlinear Finite Element Model

Figure VIII-3 compares the bend radius of curvature vs. exposure dose that are predicted by the analytical Euler-Bernoulli composite beam model and a nonlinear finite element model

(FEM) with a Neo-Hookean constitutive material model. While the nonlinear FEM is in slightly better agreement with the experimental data, both models agree regarding the qualitative description of the bend radius' change with exposure dose.

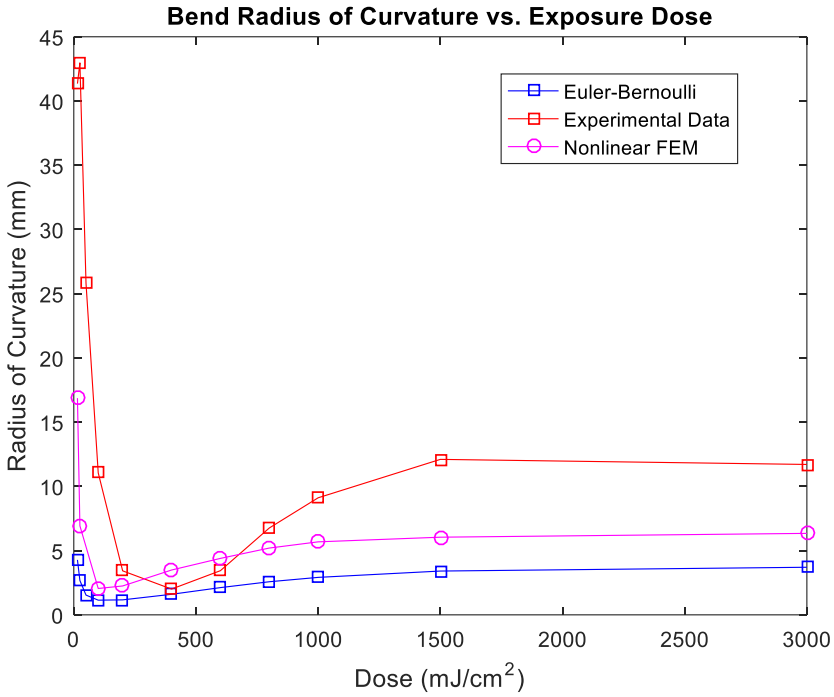

Figure VIII-3. Predicted bend radius of curvature vs. exposure dose using both the analytical Euler-Bernoulli composite beam model and a nonlinear finite element model (FEM). Both models agree on the qualitative behavior of the bend radius as the exposure dose increases, however, the nonlinear FEM is in slightly better quantitative agreement with the experimental results.

C. Predicting the Bend Radius of the Waterbomb Base Hinges

Upon swelling in solvent, the waterbomb base has two primary mechanisms that lead to folding: swelling-induced deformations within the hinges, and swelling-induced, constrained buckling of the unpatterned central vertex. The deformations induced by the buckling of the central vertex are coupled into the hinges through the stiff panels, allowing the two effects to cooperatively fold the sheet. Measurements taken on isolated strips only show bend radii down to 1.4 mm, whereas the measured bend radii in the waterbomb base are ~0.5 mm, indicating that constrained buckling of the central vertex has a significant effect on the resultant bend radius.

The deformations induced by this buckling are analyzed from a geometrical viewpoint as shown in Figure VIII-4. For a constrained disc-shaped vertex with perimeter p $\approx 2\pi \times 0.7$ mm, and swelling strain of $\epsilon = 26\%$, the estimated bend radius of the constrained deformations is ~0.5 mm which is in agreement with the measured bend radii of the waterbomb base.

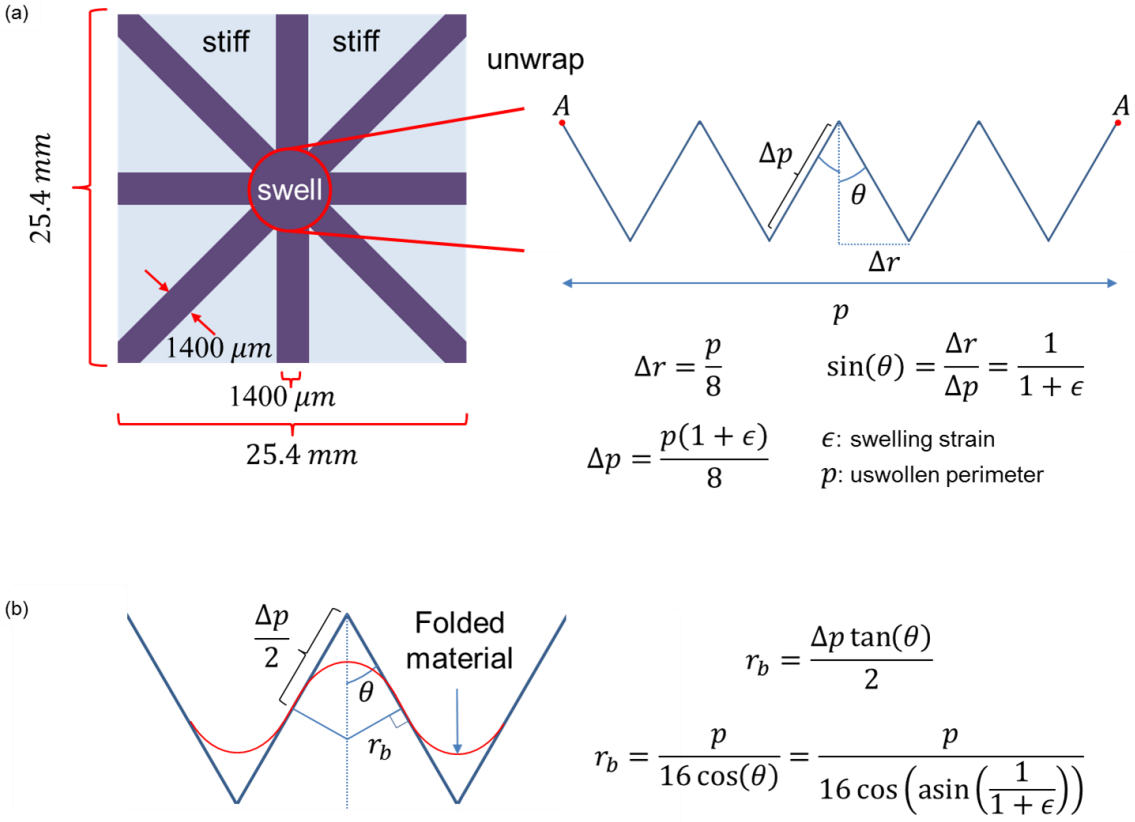

Figure VIII-4. The geometrical analysis used to predict the fold bend radius due to constrained buckling of the central disc-shaped vertex. (a) The unpatterned vertex at the center of the waterbomb base (red circle) swells and is constrained by the stiff panels (blue). These constraints cause the vertex to buckle at each of the hinges, producing a sequence of mountain and valley folds. (b) The bend radius of the folds is predicted by assuming symmetric, and alternating deformations around each of the hinges. For a given swelling strain, $\epsilon = 0.26$, and initial perimeter, $p = 2\pi \times 0.7$ mm, the bend radius at each fold is predicted to be $r_b = 0.5$ mm.